UNIVERSITÀ DELLA CALABRIA

UNIVERSITA' DELLA CALABRIA

Dipartimento di INGEGNERIA CIVILE

Dottorato di Ricerca in

INGEGNERIA CIVILE E INDUSTRIALE

CICLO

XXXVII

TITOLO TESI

"Field experiments on wind-wave forces acting on rough horizontal cylinders"

Settore Scientifico Disciplinare CEAR 01/B

Coordinatore: Ch.mo Prof. Domenico Mundo

Firma [redacted] Firma oscurata in base alle linee guida del Garante della privacy

Supervisore/Tutor: Ch.mo Prof. Francesco Aristodemo

Firma [redacted] Firma oscurata in base alle linee guida del Garante della privacy

Dottorando: Dott. Federico Casella

Firma [redacted] Firma oscurata in base alle linee guida del Garante della privacy

Università della Calabria

Dipartimento di Ingegneria Civile

T H E S I S

"Field experiments on wind-wave forces acting on rough horizontal cylinders"

XXXVII-CYCLE:

Civil and Industrial Engineering Ph.D Course

CANDIDATE:

Eng. Federico Casella

SUPERVISOR:

Prof. Eng. Francesco Aristodemo

COORDINATOR:

Prof. Eng. Domenico Mundo

Rende
2024

Abstract

The present thesis deals with field experiments conducted to study the influence of barnacles on the evaluation of the wind-waves forces at a horizontal submerged cylinder. Field tests were performed in the reserved portion of sea at the Marine Energy Laboratory (MEL) of the University of Reggio Calabria. The laboratory set-up was composed by three iron frames, carefully anchored on the sea bed at a water depth of 1.9 m, supporting a smooth cylinder treated to avoid the formation of marine fouling and a rough one. The latter was simulated by an external roughness printed artificially and characterized by the presence of barnacles. A battery of eight pressure transducers was placed in the middle of each cylinder to evaluate the wave forces, while two ultrasonic probes were used to detect the free surface and to deduce the wave direction and the undisturbed kinematic field at the cylinder centre. For practical purposes, the hydrodynamic force coefficients in the Morison and transverse equations were deduced from the experimental kinematics and forces at the cylinder. The effect of the involved roughness around the cylinder in comparison with the smooth one was analyzed in terms of force history, force peaks, force spectra and probability of exceedance of the force peaks. Deep learning techniques were applied to help in extracting the influences of barnacles on wind-waves loads on the studied horizontal cylinder. The main results highlight

an overall increase of the wave forces on the rough cylinder if compared to the smooth one as well as of the hydrodynamic force coefficients. Furthermore, it has been observed an overall feasibility of Morison and transverse schemes in assessing the hydrodynamic loads, particularly for the case of smooth cylinder.

Acknowledgments

During the three years of my PhD, many people played a crucial role in ensuring that this work could come to life and develop in the best possible way. Some provided invaluable support from a scientific perspective, guiding me with their knowledge and expertise in the academic field, helping me overcome the various challenges of research. Others offered significant support on a more personal level, providing understanding, motivation, and advice during the most challenging moments. Lastly, there were those who were able to seamlessly combine both the scientific and personal aspects, showing me how intellectual growth can go hand in hand with emotional and relational development. From all of these individuals, I hope to have gained valuable and lasting lessons that I will carry with me, fully aware of the impact they've had not only on the success of this project but also on my growth as a person.

A special thank you goes to those who made this journey possible and meaningful. First and foremost, I wish to express my deepest gratitude to Prof. Francesco Aristodemo, my supervisor, for his invaluable guidance, patience, and constant availability. His scientific expertise and insightful feedback were fundamental throughout the research process, helping me to navigate challenges and refine my work with greater clarity and precision. His support was essential for the completion of

this project.

I would also like to thank Prof. Fabio Filianoti from the University of Reggio Calabria for giving me the opportunity to carry out the experimental activity at the Marine Energy laboratory (MEL). I would also like to thank him for the invaluable scientific advice during the research that allowed this work to be completed, for the help during all the crucial phases of the experiments and for the contagious passion he passed on to me for experimental field activities.

I would like to express my sincere gratitude to my colleagues from the MEL laboratory of the University of Reggio Calabria and from the GMI laboratory of the University of Calabria for their invaluable support throughout my research. Their collaboration, constructive feedback, and willingness to share their expertise have played a key role in refining my scientific work. Whether through productive discussions, offering advice, or simply being available to exchange ideas, their contributions have been instrumental in helping me navigate the challenges I faced.

I would like to extend my heartfelt thanks to Prof. Franck Schoefs for graciously hosting me during my research stay at the Nantes Université. His support and generosity in welcoming me into his research group provided an invaluable opportunity to expand my academic horizons and engage in meaningful collaboration.

Finally, I would like to express my deepest gratitude to my family and friends. Their unwavering support, patience, and encouragement have been a constant source of strength throughout this journey. Whether through offering words of comfort during challenging times or celebrating small victories along the way, their presence has been invaluable. I am truly lucky to have them by my side, and I could not have reached this point without their love and understanding.

Contents

List of Figures

List of Tables

CHAPTER 1

Introduction

1.1 Marine biofouling on cylindrical structures

From ancient times to the modern era, humans have always tried to construct at sea to exploit its resources, and to make people's lives easier. People began to colonize the sea to build, for example, ports to facilitate communications and coastal structures to reduce erosion and inundation phenomena. With the industrial era, the attention was focused, for example, to try to acquire energy from non-renewable (e.g., oil and gas) and renewable sources (e.g, winds, currents, wind-waves and tides). With the development of coastal and offshore engineering, engineers have tried to understand the complexity of marine environment in terms of interactions between waves and structures. In fact, putting a men-made structure at the sea, the flow field changes and this can cause a multitude of problems such as instability and vibrations.

In this context, the present thesis is focused into studying the interaction between wind-generated waves and a particular type of marine structure such as horizontal cylinders. These bodies are abundant into the sea. Example can be found in

the sub-structures of offshore platforms that usually are employed in oil and gas industry 1.1, in wind farms 1.2, in radar surveillance and oceanographic research. Other type of cylindrical structures that can be found at the sea are the submarine pipelines placed near, at the bottom or below it to transport fluids such as oil, gas and waste water or electrical cables 1.3.

As a result, in coastal and offshore engineering, a correct evaluation of the hydrodynamic loads in a wide range of environmental conditions to design cylindrical structures is fundamental. When planning that it must be taken into account that every structure into the marine environment is subject to the settlement and growth of the so called bio-fouling. It causes an increase in the diameter and the projected area causing a rise of the hydrodynamic loads due to modifications of the near flow field, especially if the growth is abundant on a relative small structure (e.g., [1, 2]). This means that it is large enough to disrupt the smallest eddies near the surface, and thus the surface cannot be considered smooth. As a surface became roughened, a change in the hydrodynamic forces is highlighted. Marine growth accumulation also increases the mass and structural weight and can induce a reduction in vortex shedding frequency [1, 3, 4]. Attention must also be paid to the management costs. In fact, the maintenance and cleaning costs of the marine structures increase dramatically due to the presence of roughness [5]. The growth of marine fouling starts with the deposition on the structure of a bio-fouling film, composed by bacteria and diatoms. Macro-fouling is later formed by algal spores and various larvae of sessile invertebrates that settle on the surface of the substrate and then develop into adult individuals [6]. Generally, the growth pattern is closely related to the physical and chemical characteristics of the water. The main ones include: seawater temperature, amount of dissolved oxygen, pH, conductivity, turbidity and salinity [7]. Marine fouling grows rapidly in the initial stages, and then

Figure 1.1: Offshore oil and gas platform.

settles down over the time. Figure 1.4 illustrates two examples of the zonal and vertical distribution of potential growth on offshore structures in the southern North Sea. Generally, biofouling can be influenced by various environmental factors such as light availability, water flow speed, and depth. For instance, kelps are restricted to near-surface areas where light is crucial for photosynthesis. Barnacles are usually found in between the intertidal zone and the first 2 m below the surface level. The inherent randomness and uncertainties of biofouling make modeling this environmental load considerably more complex. The biggest challenge is accurately predicting the structural impacts and determining the fluid force coefficients. The involved parameters to investigate the marine fouling, as shown in Fig. 1.5a, are usually the height of the roughness k, the standard thickness t which is the mean value of the size of the roughness over the surface, the diameter of the cylinder D and the equivalent one D_e (considering the size of the fouling). Marine growth can be either hard, or soft and flexible, or a mixture of both (Fig. 1.5b).

Figure 1.2: Offshore wind farm.

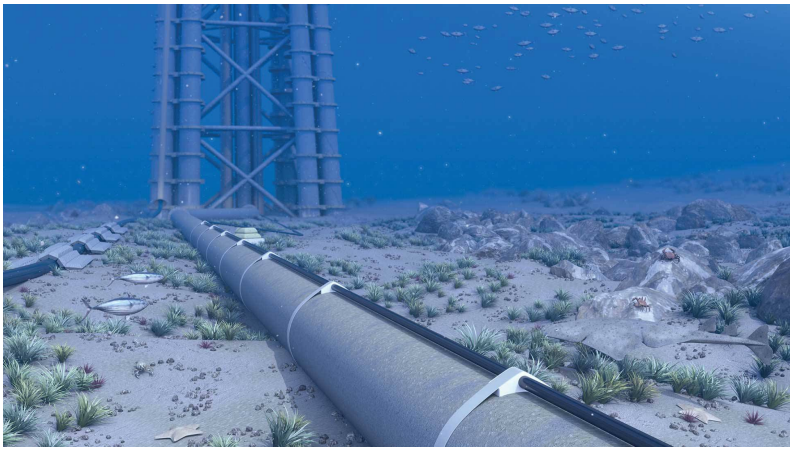

Figure 1.3: Submarine pipeline.

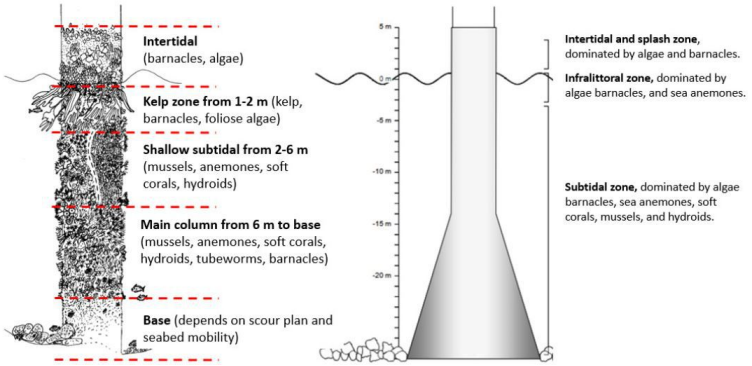

Figure 1.4: Schematic view of zonal communities and their vertical distribution on offshore structures in the southern North Sea (adopted from [8]).

To optimize the design and re-qualification of marine cylindrical structures, a huge attention need to be paid on biocolonizations. As said before, the settlement and growth of marine roughness is random and full correlated to many factors, and can cause a lot of problems about the structural integrity of these structures. The knowledge and understanding the growth pattern of marine fouling on structures can be useful to provide and calibrate mathematical models for the evaluation of wave forces on these structures. This is to ensure a more effective design that takes into account the operating conditions of the structure and to improve the stability analysis. Another important aspect takes into account the maintenance methods and protocols of this type of marine structure.

1.2 Aim of the thesis

Due to all the uncertainties of the marine environment, the impact of the fouling in the evaluation of hydrodynamic forces on horizontal cylindrical structures needs to be deeply inves-

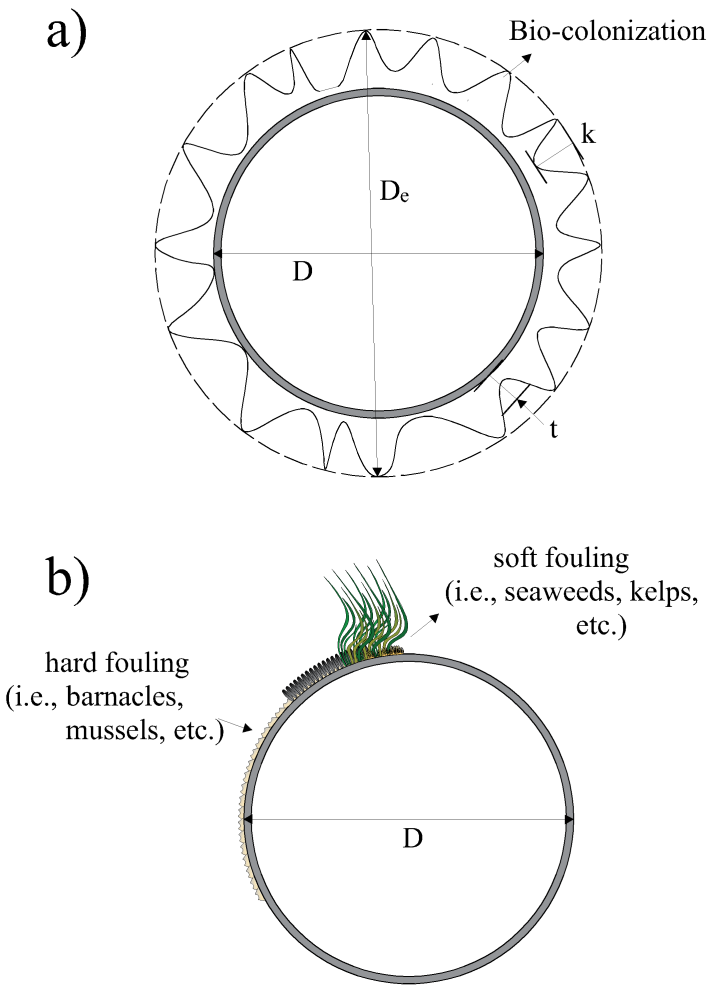

Figure 1.5: a) Parameters of surface roughness; b) Types of hard and soft fouling.

tigated. That is necessary to provide guidelines to make the design procedure of these structures easier, and also to draw up maintenance protocols. For the above reasons, this work discusses on field tests conducted at the Marine Energy Laboratory of the University of Reggio Calabria to investigate the features of wind-wave forces acting on a submerged horizontal cylinder with printed barnacles along its external surface. The experimental set-up was composed by an iron frame structure supporting two horizontal cylinders, one rough and one treated to keep it smooth during the time. On the basis of the time series of the wave forces and the kinematics at the cylinder, the hydrodynamic coefficients (drag, inertia and lift) in practical semi-empirical equations will be calibrated using a time domain method ([9]). The starting point of this study was the experiences made by [9] and [10], in which the authors investigated the accuracy of Morison and transverse equations to determine the wave forces acting on vertical and horizontal smooth cylinders conducting field experiments. Using a database of wind waves, they compared two stationary random force processes. In particular, one measured and one calculated using the Morison [11] and the transverse [12] semi-empirical models. They deduced the hydrodynamic force coefficients in a range of Keulegan-Carpenter numbers K_C up to 20 and Reynolds numbers Re ranging about between $2 * 10^4$ and $2 * 10^5$. However, the presence of smooth cylinders proves to be quite distant from the operating conditions at sea where the fouling assumes a relevant importance on the structural integrity of the involved structures. This was the principal reason to extend their works taking into account a more realistic condition with the presence of barnacles. The use of deep learning techniques was also helpful in investigating the features of wind-wave forces acting on horizontal cylinders covered by hard fouling.

1.3 Structure of the contents

The contents of the thesis are presented as follows. In Chapter 2, a review of the roughness around circular structures under waves is illustrated. Specifically, this chapter highlights the literature experiences related to laboratory tests and field tests conducted to evaluate the incidence of surface roughness into the evaluation of hydrodynamic loads. Details of the applications of deep learning techniques in coastal engineering and in assessing the interaction between waves and structures are also shown.

In Chapter 3, the design and the realization of the experimental set-up is illustrated. In particular, details of the particular site of the experiments are described in Section 3.1, while the design and construction of the set-up is highlighted in Section 3.2. Finally, the used instruments and their calibration is reported in Section 3.3.

In Chapter 4, the adopted methodologies are illustrated. Specifically, this section describes the theory of sea states proposed by Boccotti [13] and the methods to obtain the directional wave spectrum from the time series of surface elevations [14] as well as the kinematic characteristics of the waves [9]. The approach to obtain the horizontal and vertical forces at the cylinder from the pressure measurements is explained, as well as the Morison and transverse semi-empirical models for short-crested waves.

In Chapter 5, deep learning techniques are applied to the experimental results. This to train a neural network in predicting the features of the wind-wave forces on rough cylinders (e.g., percentiles of the forces).

Chapter 6 shows the results of the experimental campaign and the application of deep learning techniques. The features of the horizontal and vertical forces on the smooth and rough cylinder due to the action of wind-generated waves are highlighted, as well as the calibration of the hydrodynamic coeffi-

cients in the Morison and transverse semi-analytical schemes, the force spectra and the probability of exceedance of the force peaks.

Finally, in Chapter 7 the conclusions and future development close this thesis.

CHAPTER 2

State of art

2.1 Hydrodynamic forces on cylinders

2.1.1 Fluid dynamics around circular cylinders

Cylindrical structures are widely employed both in coastal and offshore engineering. They are commonly used for submarine pipelines (e.g., [15]) or as supports of offshore platforms and wind turbines (e.g., [16]). Let us consider the scheme reported in Fig. 2.1, where a cylinder subject to waves is proposed. As a notation we will consider the axis y as the wave direction orthogonal to the cylinder and the axis z through the depth. The design of horizontal cylinders starts from the evaluation of the hydrodynamic coefficients for the design waves. The fluid dynamics aspects of a circular cylinder subject to wave motion are of fundamental importance for defining the flow field around it. An accurate description of the involved physical phenomena is essential for correctly evaluating the hydrodynamic forces acting on the pipeline. When an oscillating or stationary flow field encounters a cylindrical obstacle, its trajectory is altered. For low velocities, the fluid streams impacting the obstacle experience an angular deviation, allowing them to flow around it. When the flow is characterized by

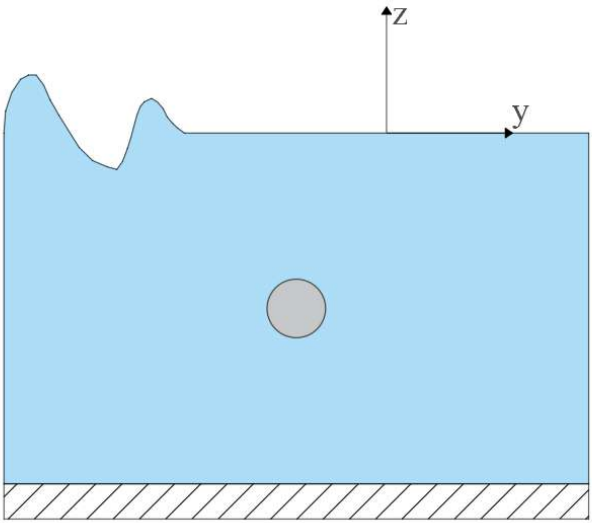

Figure 2.1: Reference axes.

significant velocities, the fluid streams at the contour of the pipe may separate, leading to the formation of vortex regions around the pipeline, with varying intensity. For the reasons listed above, researchers have firstly investigated the dynamics of waves interacting with circular cylinders to understand the physical behavior of the formation of vortices in order to assess the hydrodynamic forces acting on any type of cylindrical structure in the sea.

A wide description of the fluid dynamics around circular cylinders can be found in [17]. Starting from the flow field induced by a stationary flow, the dimensionless parameter Re, known as Reynolds number, is introduced as

$$Re = \frac{v_y D}{\nu}, \tag{2.1}$$

where v_y is the velocity of the current at the transverse axis of

the cylinder, D is the external diameter of the cylinder, and ν is the fluid viscosity.

The vortex shedding mechanism, which is activated at approximately $Re > 40$ (Fig. 2.2), involves the formation of a vortex on the upper surface of the cylindrical body, rotating in the same direction (clockwise) as the vorticity contribution. This vortex develops in a wider wake region compared to the vortex that forms on the lower surface, which rotates in the opposite direction (counterclockwise). The smaller shedding amplitude of the vortex generated on the lower part of the cylinder surface causes it to move upward towards the upper part of the cylinder, where it disrupts the fully developed upper vortex, detaching it from the upper surface and allowing it to propagate away. Following this, a third vortex forms on the upper surface of the cylinder, following the path of the first vortex. The fully developed vortex from the lower surface is then disrupted by this new vortex as it moves downward along the cylinder.

For cylinders under regular waves, another dimensionless parameter is introduced to describe the dynamics of the flow around the structure. This is the Keulegan-Carpenter number, KC, that is calculated as

$$KC = \frac{v_{y_m} T}{D}, \tag{2.2}$$

where v_{y_m} is maximum value of the undisturbed horizontal velocity at the transverse axis of the cylinder, and T is the wave period.

The temporal variation of the horizontal velocity of an undisturbed flow field, defined by a sinusoidal oscillatory motion, is given by the expression:

$$v_y(t) = v_{y_m} cos(\omega t), \tag{2.3}$$

where ω (angular frequency) $=2\pi/\mathrm{T}$.

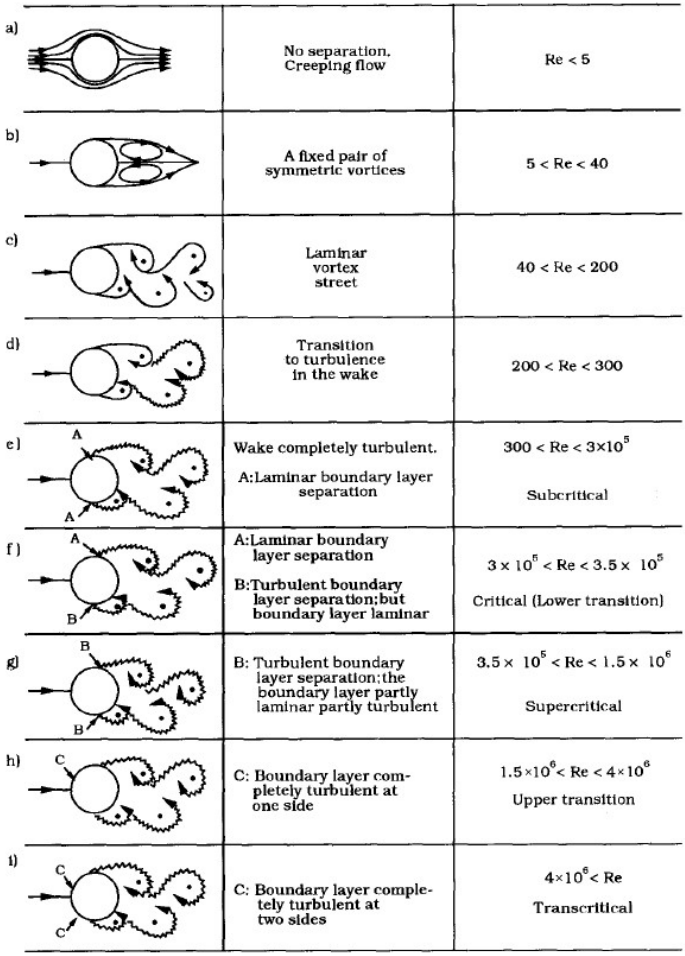

Figure 2.2: Flow around a circular cylinder in steady flow as a functions of Re [17]

.

A classification of the impact of a sinusoidal fluid motion on a horizontal cylinder was made by [17], for $Re = 10^3$, as a function of KC (Fig. 2.3). For values of $KC < 1.1$, there is no separation of the fluid mass around the cylinder, and the flow regime can be considered laminar. Initial separation from the cylinder's surface occurs in the narrow range of $1.1 < KC < 1.6$, known as the Honji instability regime ([18]). The two-dimensional flow, varying along the direction of motion and vertically, expands to form laterally vortex strips in a mushroom shape. As the Keulegan-Carpenter number increases ($1.6 < KC < 4$), the impact of the fluid mass on the cylinder leads to the continuous development of two symmetric vortices along the primary direction of flow, which detach from the cylinder's upper and lower surfaces. The symmetry of the vortices is disrupted for $KC > 4$. This phenomenon results in the generation of hydrodynamic forces directed along the direction orthogonal to the flow, directly linked to the asymmetric development of the vortices. The vortex shedding regime occurs, according to [17], for values of $KC > 4$. Other authors have defined the onset of this regime at $KC > 6$ ([19]; [13]). Depending on the variation of the Keulegan-Carpenter number, different vortex shedding regimes exist. Each regime is characterized by a different configuration in the development of the vortices (Fig. 2.3).

The flow regime around a cylinder subject to a 2D irregular oscillatory flow is defined by a Keulegan-Carpenter number, KC, and a Reynolds number, Re, which depend on the statistical and spectral characteristics of the irregular waves. According to [20] and [21], Re and KC are respectively equal to

$$Re = \frac{v_{y_{m0}} D}{\nu}, \tag{2.4}$$

$$KC = \frac{v_{y_{m0}} T_p}{D}, \tag{2.5}$$

a) 	No separation. Creeping (laminar) flow.	KC < 1.1
b) 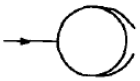	Separation with Honji vortices. See Figs. 3.3 and 3.4	1.1 < KC < 1.6
c) 	A pair of symmetric vortices	1.6 < KC < 2.1
d) 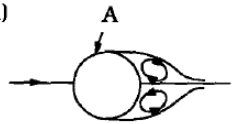	A pair of symmetric vortices. Turbulence over the cylinder surface (A).	2.1 < KC < 4
e) 	A pair of asymmetric vortices	4 < KC < 7
f) 	Vortex shedding	7 < KC Shedding regimes

Figure 2.3: Vortex regimes around a circular cylinder under regular waves [17].

where $v_{y_{m0}}$ is the significant velocity, calculated as a representative value of the maximum amplitude of the undisturbed flow velocity, $v_y(t)$, induced by a random oscillatory motion along the transverse axis of the cylinder, and T_p is the peak period.

The value of $v_{y_{m0}}$ can be evaluated as

$$v_{y_{m0}} = 2\sigma_{v_y} \tag{2.6}$$

where σ_{v_y} represents the root-mean square of $v_y(t)$.

2.2 Wave forces on smooth horizontal cylinders

Once understood the flow dynamics around a horizontal circular cylinder, several authors have started to investigate the features of the wave forces on it. Experiments have been generally conducted in wave flume or laboratory tanks, while few literature experiences have been carried out directly in the field. Knowing the free stream kinematic field at the cylinder and measuring (with load cells or pressure sensors) experimentally the forces induced by the wave motion, the goal is generally to use these values in semi-empirical models (e.g., [11], [12]) to evaluate the hydrodynamic force coefficients. The horizontal hydrodynamic force F_H ([11]) is defined as the linear superposition of two different components. One component, defined as drag force F_D, is generated by the tangential stresses which arise on the external surface of the cylinder and by the particular distribution of dynamic pressures resulting in the deviation of the fluid threads around the cylinder. Another component, defined as inertia force F_{HI}, is present when the velocity of the fluid mass at the cylinder varies temporally and is therefore related to the action exerted by an accelerated motion on a cylindrical body. The most commonly used models, that will be re-arranged for this thesis in Chapter 4, are the Morison

scheme [11] and the transverse one [12]. Thanks to the first one, the horizontal force is given as

$$F_H(t) = F_D(t)+F_{HI}(t) = \frac{1}{2}\rho C_D D|v_y(t)|v_y(t)+\frac{\pi}{4}D^2\rho C_{MH}a_y(t), \tag{2.7}$$

where ρ is the fluid density, C_D is the drag coefficient, C_{MH} is the horizontal inertia coefficient, and a_y is the horizontal acceleration at the transversal axis of the cylinder.

The vertical force F_V is due to the sum of a lift component F_L, given by the asymmetric behavior of the vortices generated around the cylinder, and a vertical inertia component F_{MV}, due to the effects of the vertical acceleration field at the cylinder. Cheong et al. [12] introduced the transverse model to deduce these two force components as

$$F_V(t) = F_L(t) + F_{VI}(t) = \frac{1}{2}\rho C_L D v_y^2(t) + \frac{\pi}{4}D^2\rho C_{MV}a_z(t) \tag{2.8}$$

where C_L is the lift coefficient, C_{MV} is the vertical inertia coefficient, and a_z is the vertical acceleration at the transversal axis of the cylinder.

For several decades, the focus of many researchers has been addressed on the experimental determination of the hydrodynamic coefficients in the mentioned semi-empirical models through laboratory activities on specific scale models or directly at sea. These dimensionless quantities have been determined for small isolated cylinders ($e/D \to \infty$), near the seabed ($e/D \to 0$), or resting on it ($e/D = 0$) in cases of sinusoidal waves, sinusoidal waves with currents, irregular waves, and irregular waves with currents. The value of e is the distance between the lower part of the cylinder and the seabed. The experimental studies have allowed the determination of the hydrodynamic coefficients through a series of graphs as a function of global quantities which characterize the motion, such as the Keulegan-Carpenter number (KC), the Reynolds

number (Re), and the conditions in which the cylinder is located, such as the relative distance from the seabed (e/D).

In this Section, we will focus the attention to the studies on smooth horizontal cylinders, while in the next one we will discuss about the influences of surface roughness in the evaluation of the forces induced by wave motion. One of the first, and most relevant experience, is the one conducted by Sarpkaya [22, 23]. The analyses conducted by Sarpkaya were performed through a series of laboratory experiments using an oscillating fluid tunnel, which simulated the behavior of a sinusoidal wave motion acting on a cylinder. The main results can be also found in the book "Mechanics of wave forces on offshore structures" by Sarpakaya and Isaacson [19], and can be illustrated by the graphs in Fig.2.4. The hydrodynamic coefficients from Fig.2.4 can be applied to externally smooth cylinders, whether isolated or near the seabed, and subject to sinusoidal motion. As shown, these can be determined as a function of the Reynolds number, with $0.15x10^5 < Re < 15x10^5$ and different values of e/D, represented by a family of curves for two fixed values of KC equal to 40 and 100. The variations in the curves demonstrate that, for the same Re, the hydrodynamic coefficients increase as the cylinder approaches the seabed ($e/D \to 0$). Sumer et al. [24], investigated a horizontal cylinder placed in a wave flume with a flat bottom. The cylinder was subject to a periodic flow. The results obtained by the authors confirmed that, for a fixed value of $Re = 10^5$ and for $10 < KC < 80$, an increase of the hydrodynamic coefficients is noticeable going from the isolated condition to the seabed. Bearman et al. [25], conducted a series of experiments in order to understand the effects of regular and irregular waves on a smooth horizontal and vertical cylinder. The experiments were conducted in a wave flume, designed to reproduce both periodic and random wave conditions. The adopted model was a rigid cylinder, representative of typical offshore structural el-

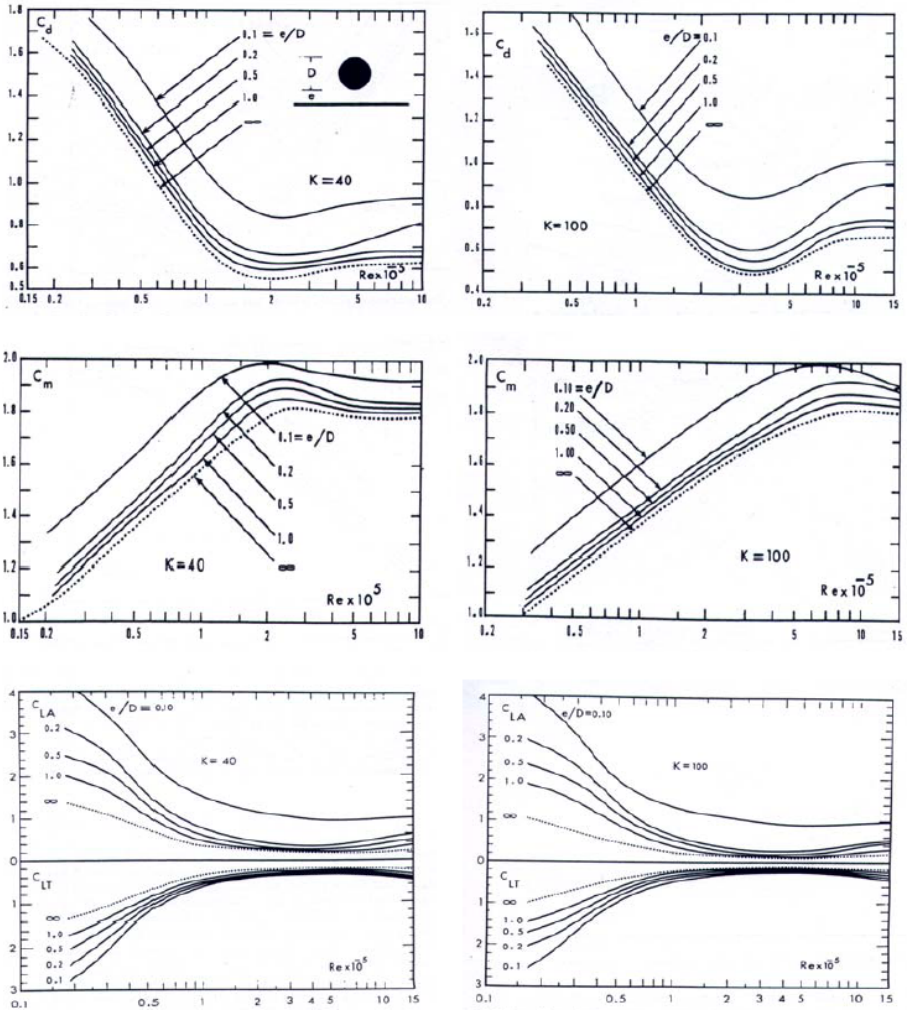

Figure 2.4: Hydrodynamic coefficients as function of Re and KC for a horizontal cylinder subject to sinusoidal motion (Sarpkaya and Isaacson, 1982) [19].

ements, and load cells were used to deduce the time series of the forces induced by the waves on the cylinders. The study observed significant variations in the loading on the cylinder depending on whether the flow was periodic or random. In fact, under periodic waves, the loads exhibited a more predictable pattern. Conversely, random waves resulted in less predictable loading, with forces fluctuating more irregularly, reflecting the stochastic nature of the waves. This highlights the challenges in applying standard hydrodynamic models like Morison's equation to such conditions. More realistic conditions can be achieved, testing models of cylinders directly into the sea. However, such tests are difficult, expensive and strongly related to the wave conditions of the test site. Few of these experiences can be found in the literature. Koterayama et al. [26] derived the drag and inertia coefficients for a vertical smooth cylinder fixed to an ocean research platform at 2 km off the coast, where the water depth was about 15 m. The diameter D and the length L of the test cylinder are 0.5 and 9 m, respectively, and the mean length of the submerged portion is 5.5 m, varying slightly with the tide. It was noticed that both the drag and inertia coefficients exhibited significant variability under random wave conditions. This variability was greater than what is typically observed under regular waves (Fig. 2.5). For the authors, the reason can be due to the fact that the hydrodynamic force acting on a body under an unsteady flow depends not only on the present flow field but also on the past, i.e. the so-called history effect.

As said in Chapter 1.2, this thesis takes inspiration on the study made by Boccotti et al. [9], in which the authors investigated the accuracy of Morison and transverse equations to determine the wave forces acting on vertical and horizontal smooth cylinders conducting field experiments. At the beginning, the authors tested a smooth isolated horizontal cylinder with different diameters. The cylinders were placed at 1 m

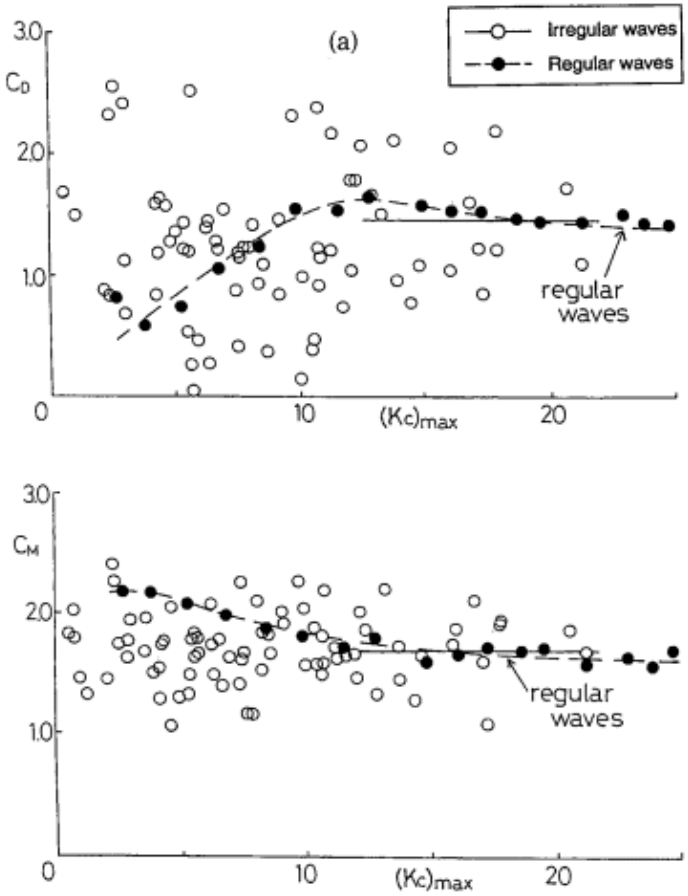

Figure 2.5: Drag and inertia coefficients from field tests (Kotereyama et al., 1995) [26].

from the free surface on a depth of 2 m. Pressure transducers were used to determine the time series of the wave forces and ultrasonic probes were mounted to deduce the wave characteristics. Concerning the results, in Figs. 2.6 and 2.7 the hydrodynamic coefficients are reported vs. KC. It is noticeable a growing trend of the drag and the lift inertia coefficients for low KC, followed by lowering for large KC. Conversely, the overall decreasing trend vs. KC was observed for the horizontal and vertical inertia coefficients. The authors also stated that Morison and transverse models are effective in representing the features of wave forces acting on cylinders in random waves.

It appears clear that, every structure, in an aggressive field such as the marine one, is subject to an increase of the dimensions related to the action of the biofouling. As we will see in next sections, researchers tried to investigate also the features of the wave forces, as well as the hydrodynamic coefficients, for rough cylinders.

2.3 Effects of marine biofouling on structures

As said in Chapter 1.1, marine biofouling can be generally divided into hard (mussels, barnacles, etc.) soft (algae, soft corals, etc.) and long flapping (kelp and seaweeds). Different types of fouling have different effects on turbulence [2]. The marine growth increases the external roughness of a cylinder and then its diameter. As shown by Achenbach and Heinecke [27] and Jusoh and Wolfram [1], that causes an increase in the flow instability. Digre and Zwerneman [28] stressed that the induced roughness height k on the diameter of the cylinder due to the formation of hard fouling (e.g., barnacles and mussels) is greater than 10^{-3} m and can exceed 10^{-2} m. So, a modification of the external surface of the structures results in a flow

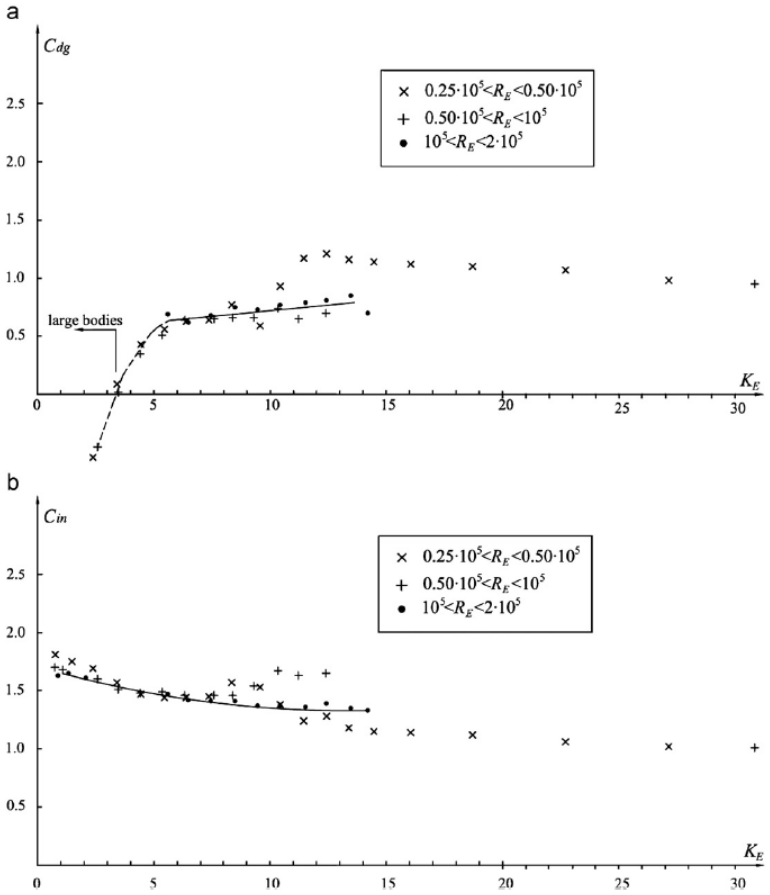

Figure 2.6: Drag and horizontal inertia coefficients from field tests (Boccotti et al., 2012) (horizontal cylinders) [9].

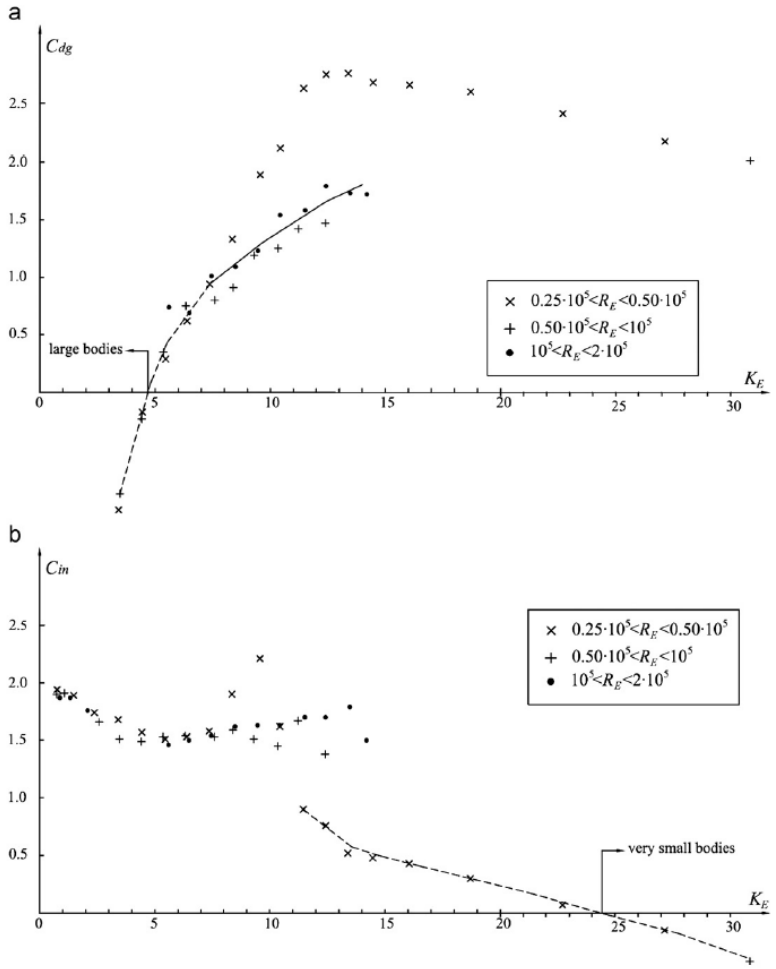

Figure 2.7: Lift and vertical inertia coefficients from field tests (Boccotti et al., 2012) (horizontal cylinders) [9].

perturbation which leads to a modification of the time series of the hydrodynamic forces. For this reason, the values of the hydrodynamic coefficients generally increase [2].

Another undesirable effect of the marine fouling is that the more a surface is roughened, the more is difficult to conduct health monitoring of the structure and maintenance activities. Biofouling can also accelerate the corrosion process of the material. Natural fouling process is also influenced by the seasonality and the environmental characteristics of the site. This process is challenging because it is a peculiarity of each site, necessitating of in-situ measurements of the growth over the time correlated to the monitoring of in-situ parameters (e.g., salinity, turbidity, pH, conductivity, water temperature, etc.) [16].

For engineering purposes, the most challenging issue is to compute the values of hydrodynamic force coefficients in the presence of marine fouling to use them in semi-empirical force models (e.g., [11], [12]). Parameters involved into the characterization of the marine fouling are its geometry and size (e.g.,[29–36]) percentage of coverage (e.g., [31–33]) and the pattern of the colonization (e.g., [31–36]). At high Reynolds numbers, all of these parameters have an impact on the hydrodynamic force coefficients.

To study the effects of marine growth on structures, as done for the cases of smooth cylinders, a common practice is to carry out small-scale laboratory experiment using artificial or natural roughness. In this thesis, we will refer just on experience with artificial biofouling tested against waves, currents or a combination of both in wave flume or tanks, where cylindrical-type structures were placed. In particular, a detail of the test facilities and the results obtained by the past experience authors in terms of the effects of marine fouling on the hydrodynamic forces on circular cylinders will be presented. All the gaps will be finally highlighted.

2.4 Laboratory tests of marine biofouling on cylindrical structures

To test the effects of marine fouling on the hydrodynamic loads on structures, a scaled experiment is the most common practice. The scaled tests are usually carried out in laboratory facilities placing rough cylinder in tanks, flume or directly into the sea. Regular waves or irregular waves are imposed to evaluate the time series of the hydrodynamic forces. The roughness of a cylinder can be artificially modeled with sandpaper, gravel, dimples, pyramids, artificial mussels, or tapes to reproduce soft fouling (e.g., [4, 22, 31–37]). Tests with natural biofouling can also be found in literature (e.g., [38]).

With particular reference to the hard roughness, several literature studies on cylindrical structures were performed. Sarpkaya [22] used a horizontal cylinder subject to a fluid oscillating in an U-tube. A comparison between a smooth and a sand-roughened cylinder was made in terms of horizontal and transverse forces through an extensive laboratory campaign. The results obtained for rough cylinder by the author in terms of drag and inertia force coefficients have shown that they both tend to values higher than the smooth cylinder, while small differences were noticed for the lift force coefficient. Theophanatos and Wolfram [4] undertook laboratory experiments with artificial macro-roughness (pyramid-type) on a horizontal cylinder under the action of steady flows or regular waves. They observed that the marine growth significantly increases the hydrodynamic loads, and this effects depends on the overall thickness, surface cover and distribution of the fouling. In the study carried out by Wolfram and Naghipour [37], roughness fiberglass elements were used as hard growth on two cylinders. The effects of irregular waves, currents and a combination of both were tested. They highlighted that the force coefficients varied significantly adding an external roughness, showing that

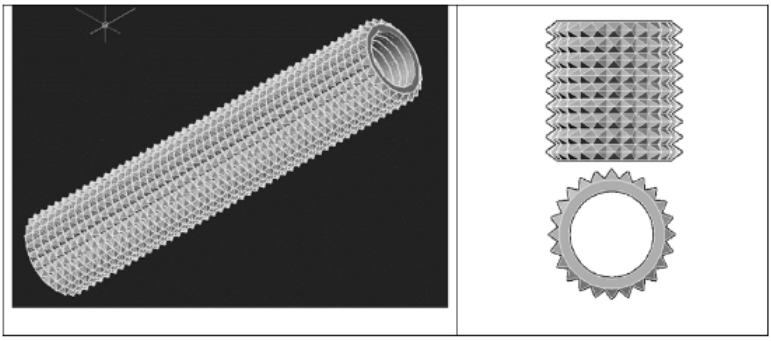

Figure 2.8: Rough cylinder used in the experiments of Zeinoddini et al. [31].

the addition of a current decreased the drag coefficient and, to a lesser extent, the inertia coefficient. Baarholm and Skaugset [39] studied the effects of marine fouling on a oscillating horizontal circular cylinder fitted with helical strakes. The hard growth was reproduced by gluing coarse sand and gravel over the cylinder. The mean height of the growth and its effect on the wave forces was analyzed. Zeinoddini et al. [31] studied the vortex induced vibrations (VIV) of a vertical cylinder covered by uniform pyramidal roughness printed using 3D techniques (Fig. 2.8). During the tests, the cylinder started in still water conditions and accelerated up to the desired velocity along the remaining length of the tank. Zeinoddini et al. [32], and Jadidi et al. [33] studied the vortex induced vibrations (VIV) of random pyramidal roughness with different coverage ratio, regular hemispherical roughness and random and regular truncated cone roughness (Figs. 2.9a and 2.9b). They observed that the force coefficients appeared to be sensitive, in descending order, to coverage ratio, aggregation, flow incidence and the fouling shape. Marty et al. [34] and Marty et al. [35] used a 3D ellipse-based mussel prototype (Fig. 2.10). The shells were arranged as a function of the angle between the major

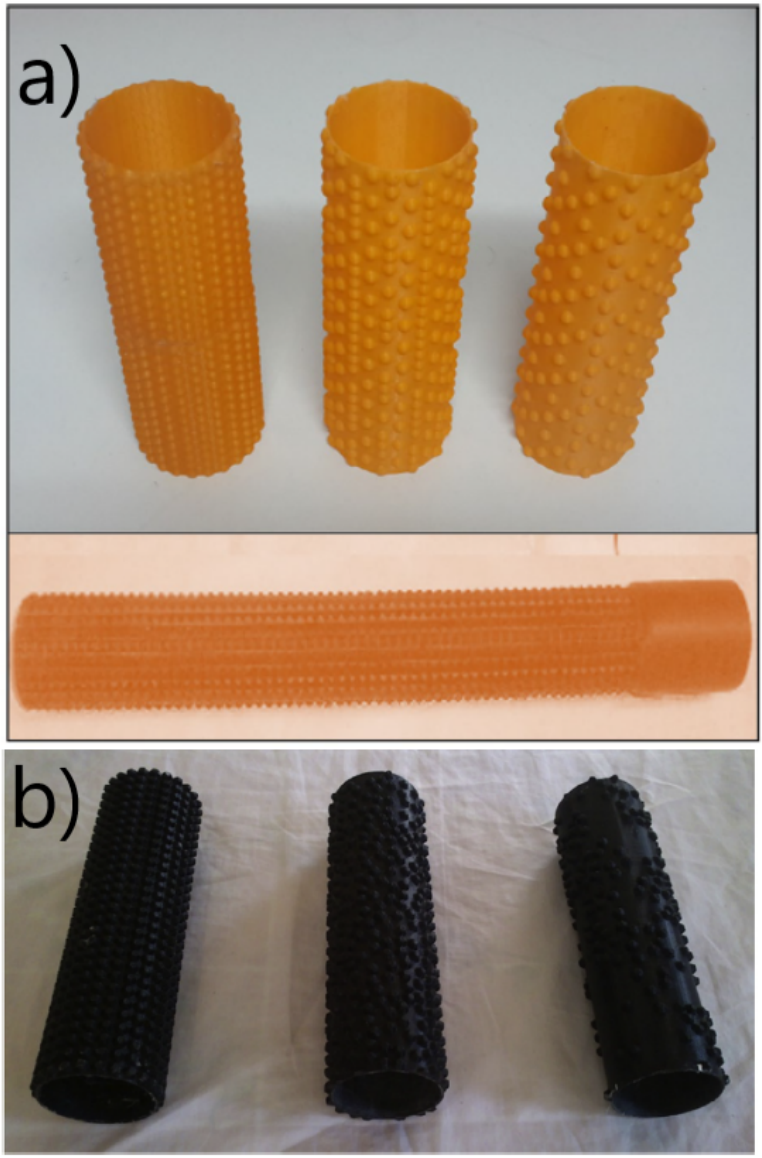

Figure 2.9: Rough cylinders used in the experiments of a) Zeinoddini et al. [32]; b) Jadidi et al. [33].

axis of the ellipse and the longitudinal axis of the cylinder to create a stochastic distribution mesh. Three conditions were analyzed: currents, regular waves and currents superimposed to regular waves. The results show that the more the cylinder surface is covered by biofouling, the more the drag coefficient increases (i.e. up to four times higher than in the case of the smooth cylinder). A small increase in the inertia coefficient was also observed (Fig. 2.11).

Marty et al. [36] investigated two different types of roughness by printing shells and corals on the cylinder surface (Fig 2.12). The coral prototype was produced on the basis of predictive models for marine growth. The same flow conditions of those analyzed by Marty et al. [34] and Marty et al. ([35] were considered. The authors found that the roughness created by the combination of shells and corals significantly increases the drag coefficient (about 50%) compared to the roughness created by shells alone and up to 4 times compared to the smooth case. Instead, the inertia coefficient generally increases from the smooth to the rough case, but a relevant difference appears between shells and corals up to 2 times.

2.5 Neural networks

Neural networks are a fundamental aspect of the artificial intelligence (AI), significantly impacting various areas such as computer vision, natural language processing, autonomous systems, and biomedical applications (e.g., [40–46]) Nowadays, also in the field of coastal and offshore engineering, many researchers tried to exploit the use of neural networks to better understand the features of various phenomena (e.g., [47–52]). Neural networks are essentially computational models designed to mimic the architecture and functioning of the human brain, with the goal of simulating how biological neurons process information.

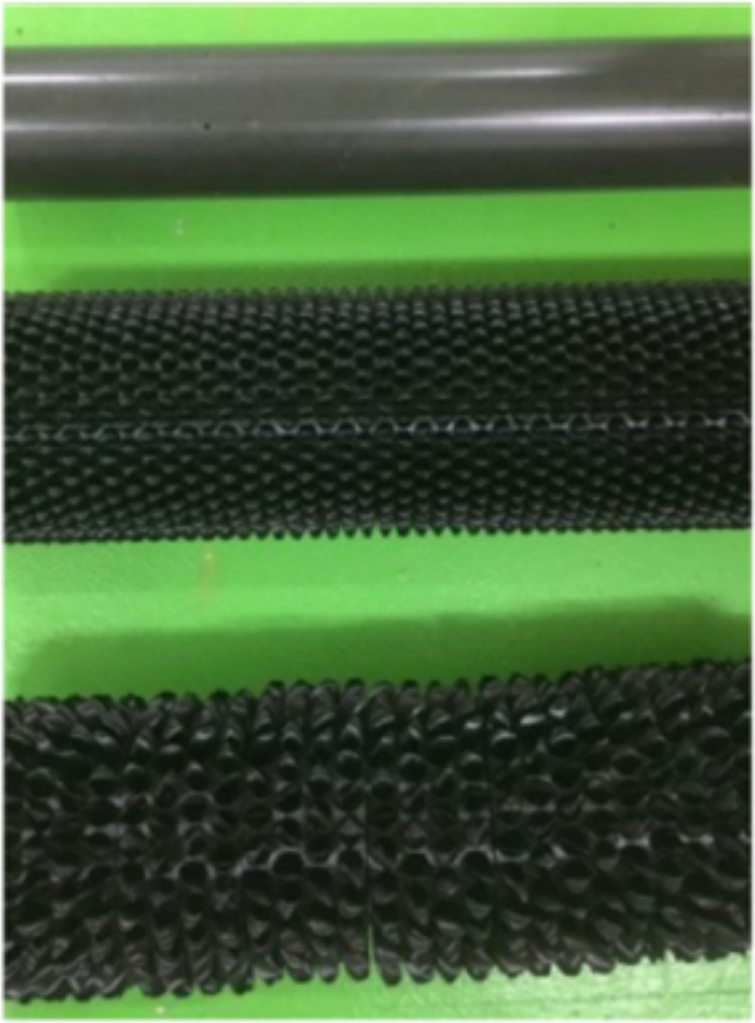

Figure 2.10: Rough cylinder used in the experiments of a) Marty et al. [34]; b) Marty et al. [35].

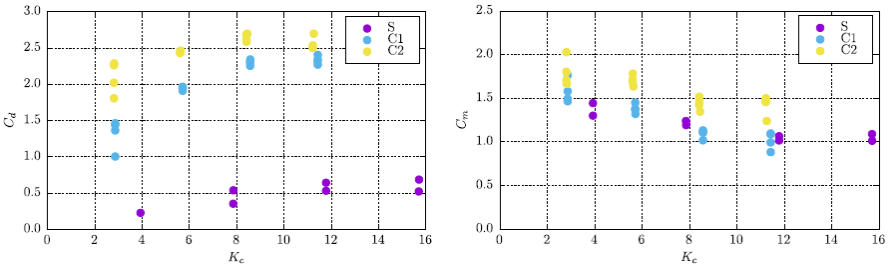

Figure 2.11: Drag and inertia coefficients vs. KC in the case of regular waves (Marty et al. [35]).

A neural network is structured with layers of interconnected nodes, known as neurons. These neurons are organized into an input layer, one or more hidden layers, and an output layer (Fig. 2.13). Each neuron within a layer is connected to other neuron in the subsequent layer through weighted connections. During the learning process, these weights are adjusted to minimize the difference between the predicted output and the actual output. The backpropagation algorithm, firstly introduced by Rumelhart et al. [53], plays a crucial role in this process. It allows for the efficient training of deep networks by iteratively adjusting the weights in order to reduce the overall error committed. Neural networks can be categorized on the basis of their architecture and intended use. The most commonly encountered types include:

- Feedforward Neural Networks (FNNs): these are the simplest form of neural networks, where the connections between neurons are unidirectional, moving from the input layer to the output layer (Fig. 2.14).
- Convolutional Neural Networks (CNNs): widely used in image recognition and processing, CNNs are specialized for learning spatial hierarchies of features from input images (Fig. 2.15).

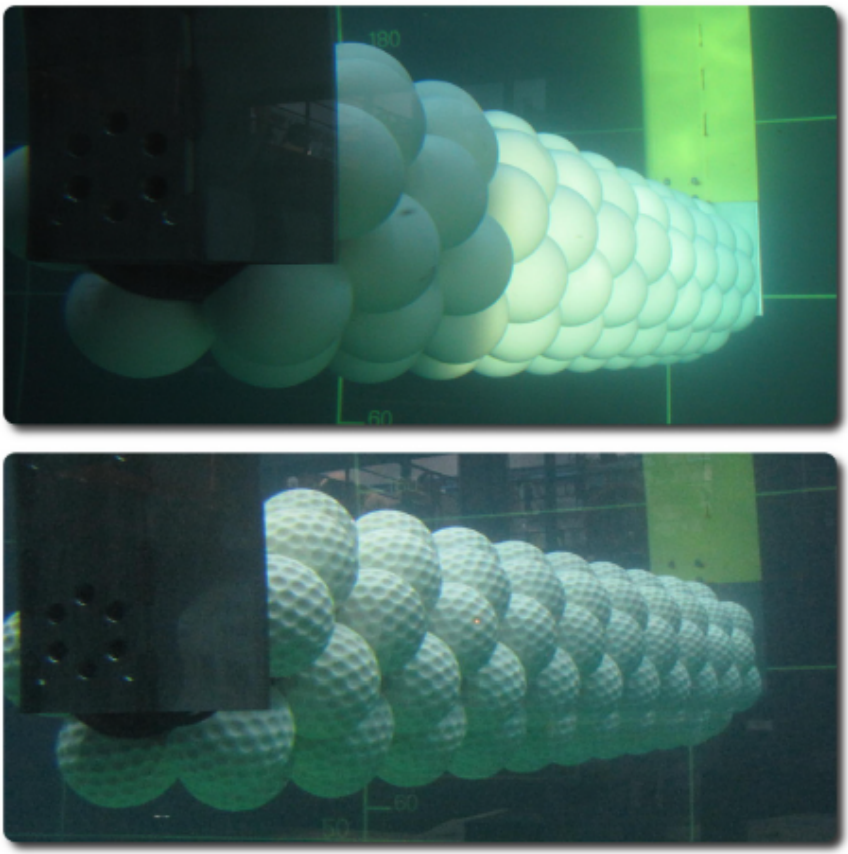

Figure 2.12: Rough cylinder used in the experiments by Marty et al. [36].

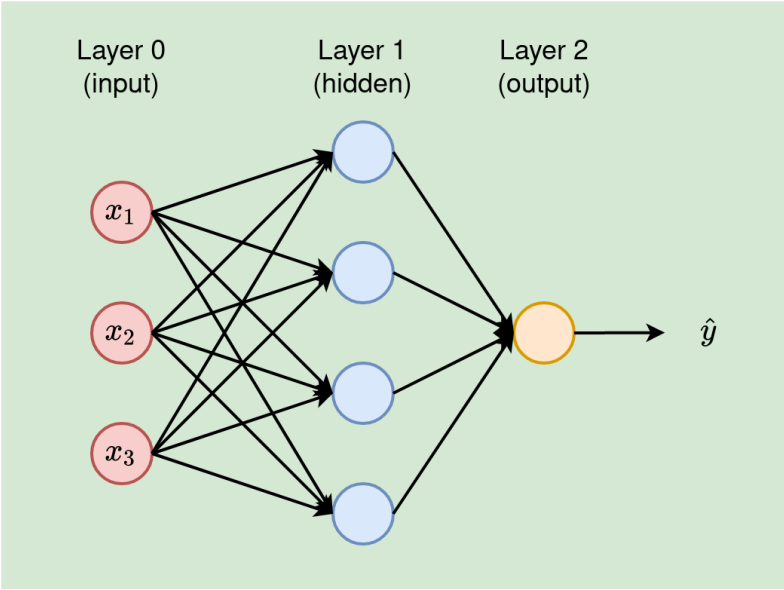

Figure 2.13: Basic scheme of a neural network.

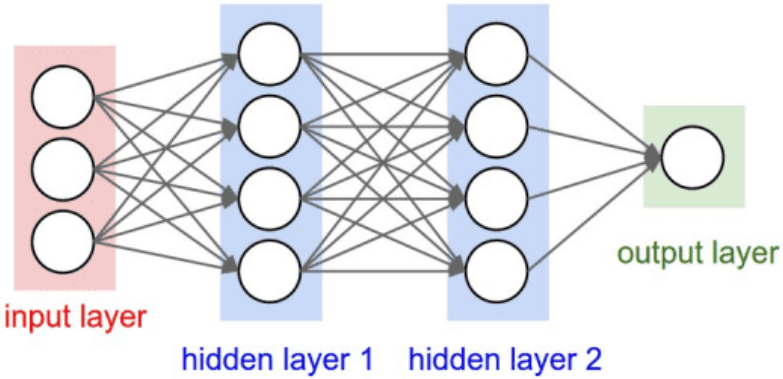

Figure 2.14: Basic scheme of a FNNs neural network.

- Recurrent Neural Networks (RNNs): unlike feedforward networks, RNNs have cyclical connections which allow them to retain information from previous inputs, making them well-suited for sequential data, such as time series analysis and language modeling (Fig. 2.16).

In recent years, the combination of increased computational power, availability of large datasets, and advancements in techniques such as deep learning has significantly enhanced the capabilities of neural networks. specifically, Deep learning refers to a neural network with multiple layers (deep neural networks) and capable of learning complex patterns from large volumes of data. Neural networks are a cornerstone of modern artificial intelligence, enabling machines to perform tasks that were previously thought to require human-like intelligence. As research progresses, neural networks will undoubtedly become even more central to the development of AI technologies, further narrowing the gap between human and machine capabilities.

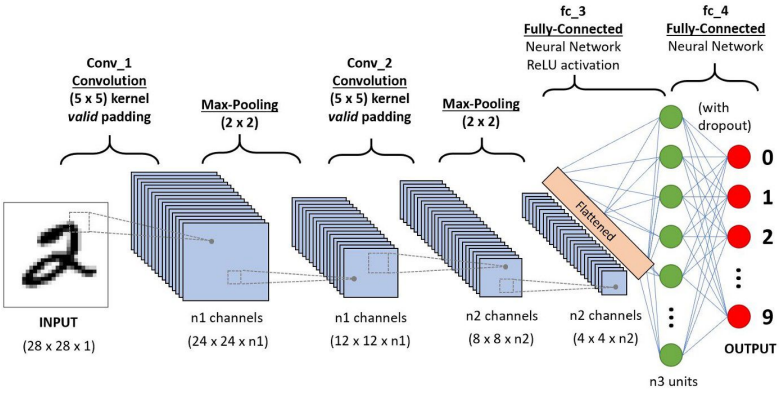

Figure 2.15: Basic scheme of a CNNs neural network.

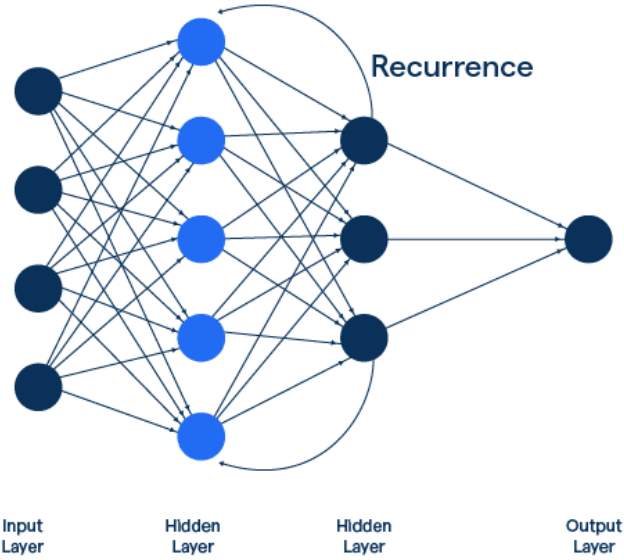

Figure 2.16: Basic scheme of a RNNs neural network.

2.6 Applications of neural networks to coastal and offshore engineering

Neural networks were used in various fields of coastal and offshore engineering. For wave forecasting, Deo et al. [54] used a simple 3-layered feed forward type of network to obtain the output of significant wave heights and average wave periods from the input of wind speeds. The network was trained with different algorithms and using three sets of data. They found that the network was useful to perform wind–wave mapping in deep waters and also when the sampling and prediction intervals are large, such as one week. Guarize et al. [55] applied a hybrid Artificial Neural Network (ANN)–Finite Element Method (FEM) procedure to perform a random dynamic analysis of mooring lines and risers. Firstly, a quite short FEM-based time-domain response simulation was generated. Then, a feedforward ANN was used to predict the time history of the structural response. A sketch of the used neural network is reported in Fig. 2.17. A multi-layered feedforward neural network was used by Balas et al. [56] to perform stability analysis of rubble-mound breakwaters. ANN were applied taking as case study a breakwater in Turkey. They found that a better agreement between the predicted stability numbers of hybrid artificial neural networks and measurements was obtained if compared to the classical stability equations. The prediction of wave and current forces on slender structures was instead investigated by Shafieefar et al. [57] applying neural networks to laboratory data. The dataset used is that related to some experiments on an oscillating vertical cylinder in current, waves and waves plus current. As can be seen in Fig. 2.18, the network adopted was composed by 5 neurons in the input layer, 12 neurons in the first hidden layer, 12 neurons in the second hidden layer and 2 neurons in the output layer. The input was the database of the current velocity, the horizontal

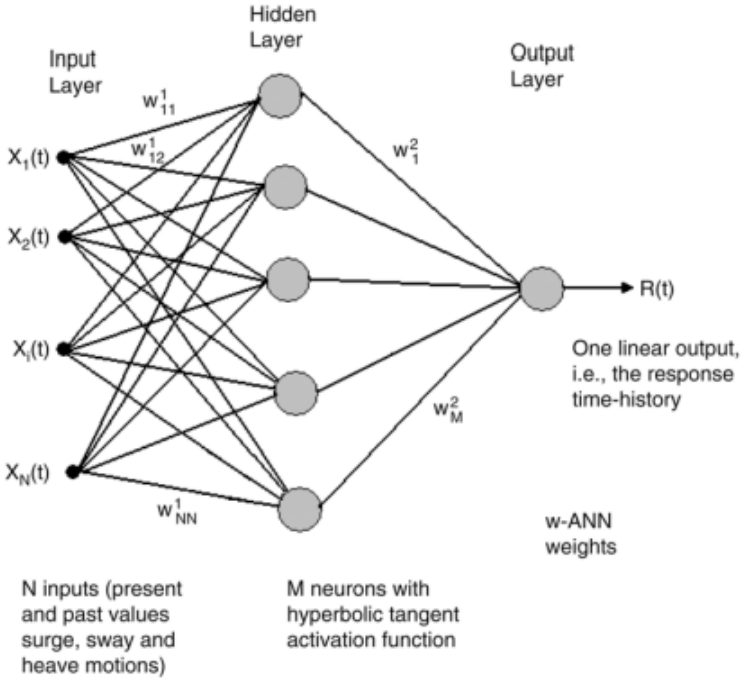

Figure 2.17: Feedforward neural network used by Guarize et al. [55].

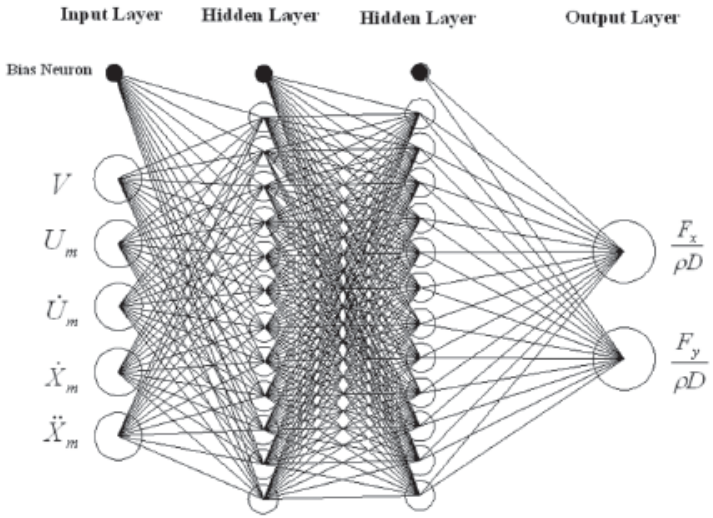

Figure 2.18: Feedforward neural network used by Shafieefar et al. [57].

velocity and acceleration due to wave motion, and the velocity and acceleration of the cylinder motion. The output was the in-line and transverse force on the cylinder. The authors stated that the results from the trained neural network indicate a better approximation performance than the Morison equation for estimating the forces exerted on a cylinder under various flow conditions. Fatigue analysis of steel catenary was performed through a coupled approach between numerical simulations and ANN by Quéau et al. [58]. This coupled technique was also applied in the field of vortex induced vibrations on cylinders. Indeed, a recent study conducted by Behara et al. [59] investigates the dynamic response and the associated wake structures at three identical tandem square cylinders oscillating in the cross-flow direction for a Reynolds number Re = 150. Through a neural network of 5 hidden layers of 40

neurons, the lift coefficients and the amplitude response were predicted. The training data were obtained through numerical simulations. To help in detecting the type of roughness on marine biofouling, that can be very helpful in designing marine structures, a convolutional neural network was used and trained on a database of 1261 images by Signor et al. [60]. The performance of the model was tested using images of offshore components with and without biocolonization. The performance was discussed with particular care, given the small number of images available and the statistical uncertainties of the metrics evaluated from the validation process. The average performance of the model on the testing images was 69% of good detection for all combined classes. By an engineering point of view, the results were satisfactory since the two classes with maximum hydrodynamic impact (mussels and no macro-biocolonization) provide average detection of 81% and 79%, respectively. The authors proposed recommendations to enrich the training image database and photographic surveys on offshore structures in order to provide metrics enabling algorithm optimization in engineering purposes. The main innovation of this study is to adapt existing machine learning tools to a new and complex application area such as the biofouling. The rapid identification of biofouling is also of great significance to the intelligent operation and maintenance of large ships or other deep-sea and offshore projects. For this reason, Zhao et al. [61] proposed a filter-guided inverse dark channel inversion exposure compensation (FIDCE) algorithm for the ambiguous images by exploring an underwater optical imaging model partially overexposed and partially underexposed. Also, MFONet, a pixel-level segmentation model, was introduced. Its backbone feature extraction network includes MobileNetV2—a lightweight CNN model with the Sandglass block as the basic unit, and combines with ASPP enhanced feature extraction module, thereby enhancing the network per-

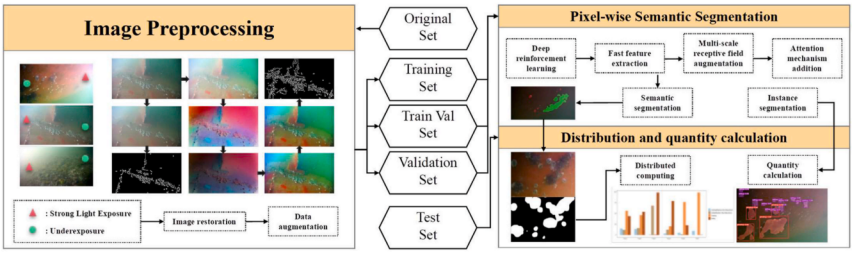

Figure 2.19: Flow chart of the model proposed by Zhao et al. [61].

ception field. According to the results, a more accurate and quicker effect can be observed in the fine-grained identification of biofouling using MFONet (see a flow chart of the model in Fig. 2.19). The flow around a circular cylinder has been investigated through neural networks in the work by Xie et al. [62]. They developed a new model that combines Graph Convolutional Networks (GCN) with Recurrent Neural Networks (RNN) (see details of the network in Fig. 2.20) to predict sequential transient flow around cylinders using unstructured flow field data. Their model has been initially verified with a flow around a single cylinder. Taking the numerical simulations as the reference, the relative errors of the predicted sequential velocity and the pressure fields are less than 3% and 2%, respectively. Subsequently, the complexity of the investigation is increased by varying the Reynolds number and introducing additional cylinders in the flow region. Good results have been obtained by the authors comparing the predicted physical fields with CFD simulations. A recent work discusses on the prediction of wave-induced forces on a wave energy converter based on a vertical cylindrical heavy point absorber (HPAWEC) using an artificial neural network [63]. The authors used a type of recurrent neural network called long short-term memory (LSTM). This network has been use-

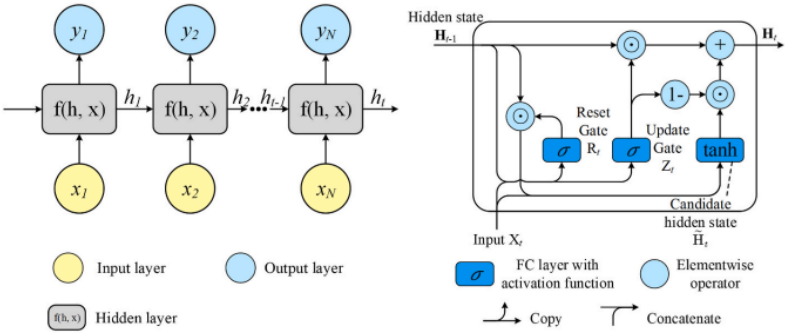

Figure 2.20: RNN used by Xie et al. [63].

ful to predict the time series of the wave forces on the WEC. The input of the ANN was the wave heights recorded by the probes, while the output was the wave excitation of the load cell (see Fig. 2.21). The results of 180 regular wave tests and 12 irregular wave tests were used to train the LSTM network. The authors stated that, for the regular wave cases, an advantage of the ANN is that it can filter random noise from the measured signal. For the irregular wave cases, the method has potential to be improved, generally quite good results are noticed but it is essential to note that the authors trained the network on a small dataset of unidirectional waves. For this reasons more tests need to be conducted in a multi-directional wave tank. For the reasons listed in Chapters 2.5 and 2.6, in the following thesis we want to use a neural network approach as support for the experimental results. We strongly believe that these techniques can help coastal and offshore engineers in extracting relationships between wave data and the forces exerted by waves on structures. This to achieve a design of maritime structures in a simpler and more efficient way. Looking at the listed literature, it can be highlighted that a deep investigation on the use of the neural networks in order to pre-

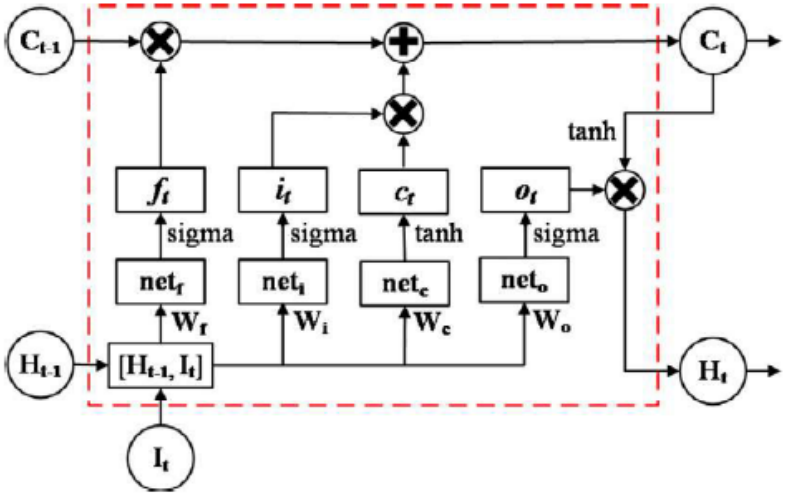

Figure 2.21: Memory block of the LSTM neural network used by Zhang et al. [63].

dict forces induced by irregular waves on horizontal circular cylinder is still lacking, as well as the influence of roughness in this physical process.

CHAPTER 3

Experimental set-up

3.1 Site of the experiments

The experimental tests were conducted using the facilities of the Marine Energy Laboratory (MEL) of the University of Reggio Calabria at the east coast of the Strait of Messina (Fig. 3.1). As highlighted by Boccotti [13], this site is quite unique for field experiments for the following reasons:

- the high stability of the wind blowing from Messina to Reggio Calabria;
- the orientation of the coast so that it is protected from the swell travelling from South to North;
- the short fetches of about 10 km;
- the relative small tide amplitude of about 10 cm.

Because of all these factors, it is possible to conduct small-scale field tests with laboratory techniques as we can do in controlled conditions in the classical laboratories. The significant wave height H_s ranged between 0.2 m and 0.8 m, the peak periods T_p ranged between 2 s and 3.8 s for wind-generated

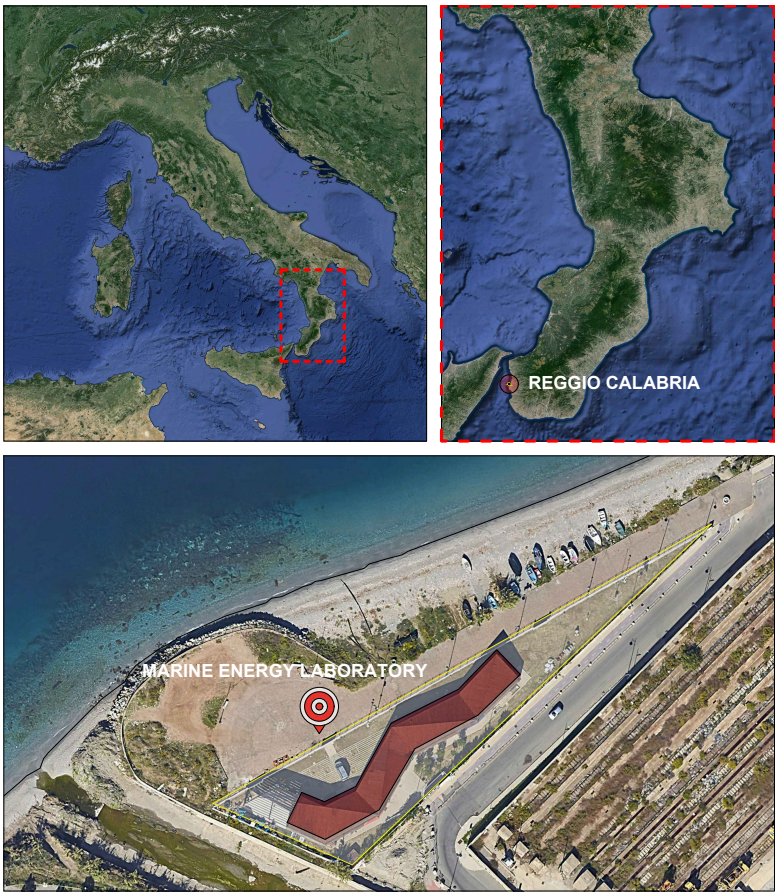

Figure 3.1: a) Geographic position of the laboratory; b) Direction of exposure; c) Features of the laboratory.

waves and between 6 s and 9 s for swell components. In this context, sea states characterized by the presence of pure wind-generated waves were here considered. The involvement of only wind waves is linked to the correct preservation of the Froude similarity between prototype and model. Indeed, the appearing of swell wave components implies unrealistic wave periods at full scale (e.g, [13]).

3.2 Design of the experimental installation

The structure of the experiments was designed to be easily assembled and disassembled directly into the water. It was composed by three iron frames (IPE160 shape), each of 1.00 m, supporting two iron cylinders of diameter $D = 0.127$ m having a length of 1.5 m Fig. 3.2a shows a 2D sketch of the experimental set-up, while 3.2b highlights a more realistic 3D sketch. The structure was placed at a water depth $d = 1.9$ m, parallel to the shoreline, through three tilting basements of 0.65 m x 0.65 m. A total of about 600 kg of iron ballasts was used to keep stable the structure. The cylinders were placed at half water depth 0.95 m (i.e., $e/D > 1$), so we can assume that they are isolated from the sea bed. To avoid a quick corrosion of the supporting structure, it was painted using two layers of epoxy primer and two layers of polyurethane finish. One of the two cylinders was treated using an anti-vegetative print to maintain it smooth over the time. At the middle support, a cross-shaped tube (3.2 m high from the sea bottom) was placed as support for two ultrasonic probes. The upper part of the installation at the sea and the installation phase with the placement of the ballasts are highlighted in Figs. 3.3a and 3.3b.

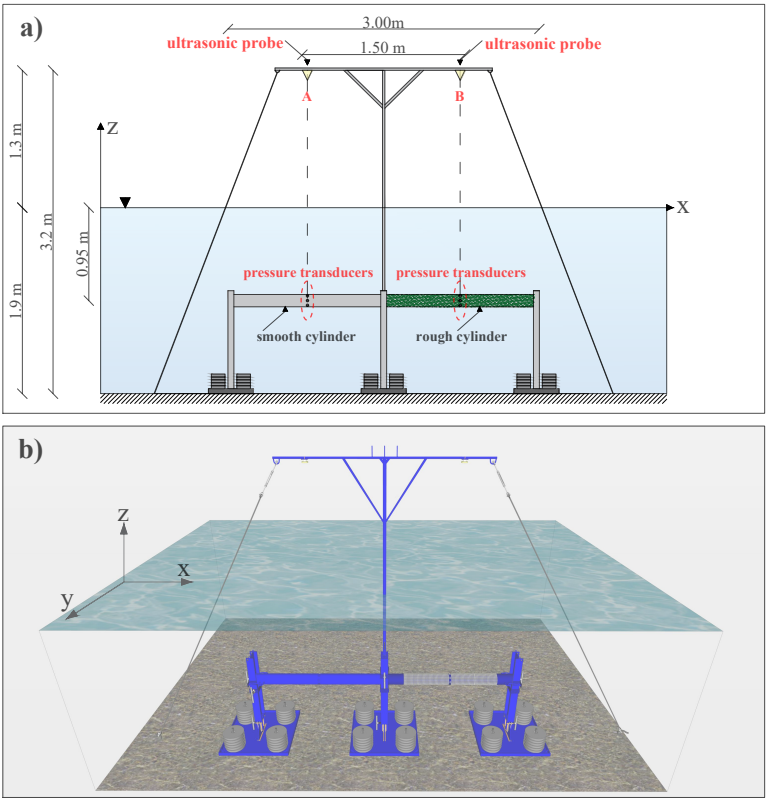

Figure 3.2: a) 2D sketch of the structure; b) 3D sketch of the structure.

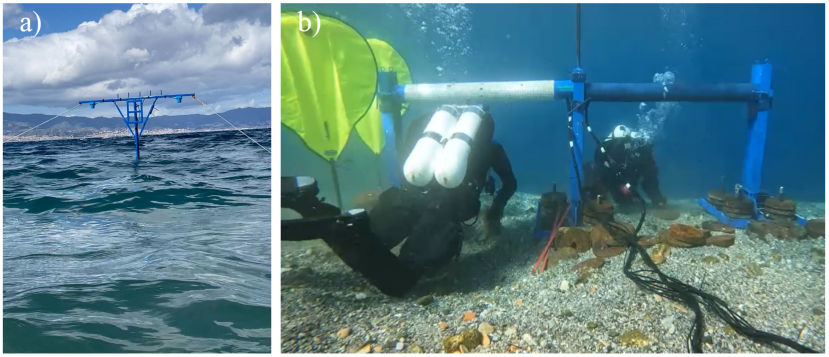

Figure 3.3: (a) Upper part of the installation at sea with the two ultrasonic probes; (b) Installation phase at sea (placement of the ballasts).

3.3 Instruments

3.3.1 Pressure transducers

A battery of 8 pressure transducers (STS ATM.1ST/n model) was placed in the middle of each cylinder (Figs. 3.4a and 3.4b), through stainless steel L-joints, to deduce the time series of the horizontal and vertical forces. Each transducer was placed at $\delta = 45°$, where δ is the reference angle positive clockwise (Fig. 3.4a). The sampling frequency of each pressure transducer was set equal to 10 Hz. Each of it had a pressure measurement range between 0 and 4 m. The range of input current was 9-33 V, while the output signal was 4-20 mA. The calibration of the transducers was made by using a portable calibrator inducing a pressure through a valve and reading the output signal. Thanks to this procedure, a linear calibration law for each sensor was possible, as shown in the example of Fig. 3.5.

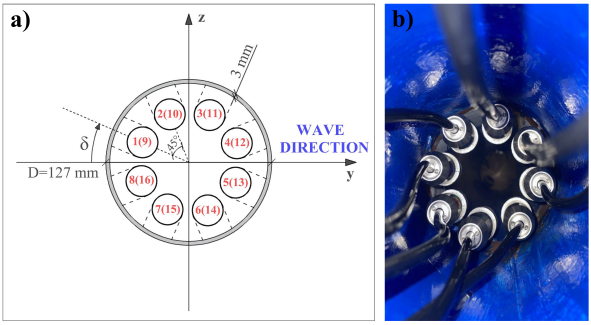

Figure 3.4: (a) Sketch of the position of the pressure transducers around the cylinders; (b) Detail of the pressure transducers inside a cylinder.

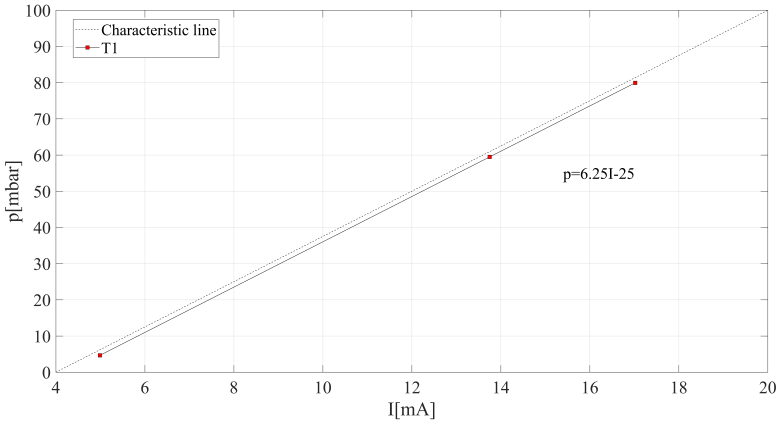

Figure 3.5: Example of calibration curve for a pressure transducer.

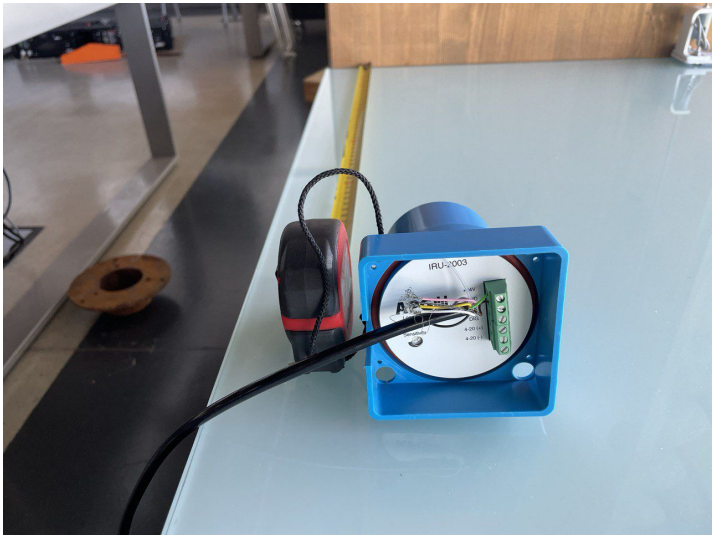

Figure 3.6: Ultrasonic probe model APG IRU-2003

3.3.2 Ultrasonic probes

Thanks to a cross-shaped tube, two ultrasonic probes model APG IRU-2003 were mounted on top of the experimental structure. They were placed at a mutual distance of 1.5 m. This instrument works sending an high-frequency pulse, catching the returning echo. It allows to evaluate the time series of the free surface elevation. The sampling frequency of the ultrasonic probes was set to 10 Hz. The calibration of the sensors was possible thanks to a calibrator connected to the probes, with an input current of 24 V and a calibration software. Thanks to the calibration software, the setting of the parameters of the probe such as the sensitivity of the instrument, the pulses and the maximum measurement distance was possible. Moreover, the testing of the results of the calibration comparing distances taken at fixed point with the values read through the calibration software was feasible (3.6).

3.3.3 The measurement system

The hardware section

The measurement system implemented to continuously read sea states, as previously described, uses 16 ATM.1ST/n pressure sensors with 4-20 mA output arranged along the circumference of the two horizontal cylinders. On the emerged part of the structure, two ATG-IRU-2003 ultrasonic level sensors were mounted perpendicularly to the sea surface to detect wave elevation.

The pressure gauges are relative sensors based on piezoresistive technology, suitable to detect rapidly changing signals. The principal measurement characteristics are

- accuracy ($\pm$ % FS) = 0.2;
- total error ($\pm$ % FS) = 0.4;
- response time (typical) $<$ 1 ms / 10 ... 90 % FS;
- long term stability (per year) $<$ 1 mbar.

The total error includes the accuracy and the temperature influence at the maximum signal variability range (16 mA). It has a sufficiently fast response time for the present application and high stability over time.

The IRU 2003 ultrasonic level sensors base their operation principle on calculating the flight time of a sound pulse reflected from the sea surface. For correct operation, it is essential that they are installed nearly perpendicularly to the surface to be measured. They incorporate internal temperature compensation for greater accuracy under varying environmental conditions, because sound speed depends on temperature, and have a 4-20 mA current loop output. The measurement range was adjusted to its minimum (3.048 m) in our application. They are housed in an ABS enclosure, resistant to UV,

moisture and enough robust for the marine environment. Their main metrological characteristics are

- frequency = 69 kHz;
- accuracy = ±0.25% of detected range;
- resolution = 2.5 mm;
- response time = programmable (55 ms minimum @ 7.62 m).

The ultrasonic level sensors require a warm-up time of about 20 min to meet the declared accuracy specifications. For this purpose, the acquisition system has been designed to ensure they are always operative.

For acquiring the 4-20 mA signals from the described sensors, a National Instruments Ethernet CompactDAQ chassis cDAQ-9185 was used. The chassis controls the timing, synchronization, and data transfer between the C Series input/output modules and an external host. This system allows the combination of multiple C Series I/O modules and provides synchronized and precise timing over the network thanks to TSN networking, ideal for highly distributed measurements over long distances. Using the TCP-IP protocol allows physical separation between the acquisition site and the board that manages the measurements, making it easier to access the data. Being a modular system, two C series 8-channel 200 kS/s ±20 mA NI-9203 current input module, for reading the pressure and surface elevation, were used. This module is ideal for advanced performance control and monitoring applications. It includes programmable input ranges and various connectivity options. For protection from transients, it includes a double insulation barrier (channel-to-ground isolation) with 250 Vrms isolation for safety and noise isolation. It employs a 16-bit ADC with an Input Noise of 1 LSB (0.3 µA). Regarding accuracy, in unipolar measurement conditions (0-20 mA) are

- Measurement conditions (typical) = 25 °C, ±5 °C;
- Percent of reading (gain error) = ±0.04%;
- Percent of range (offset error) = ±0.02%.

To evaluate the measurement chain uncertainty, we consider only the error contribution introduced by the sensors, being significantly higher than that introduced by the acquisition board.

The software section

The numerical code for data acquisition and storage was implemented in the LabVIEW language. Considering the technical characteristics previously described, the platform was designed to ensure maximum autonomy in performing measurements, guaranteeing high reliability conditions, and freeing itself from the need for expert operator intervention to assess sea conditions or select the sea states of interest among thousands of acquired packets.

To reduce the error due to digital-to-analogue conversion, we oversampled the data at 500 Hz, and then average to reduce the frequency to 10 Hz. Each sea state is identified by a packet of 3000 points corresponding to a duration of 5 min. The flow chart of the acquisition process is sketched in Fig. 3.7.

To optimize memory usage, considering long-term acquisitions and the peculiar characteristics of the sensors used, the acquisition procedure was splitted into two alternative tasks. The first task acquires only the ultrasonic sensors, every 5 min calculates the parameters of interest related to the acquired sea state (H_s, T_p, ψ^* and T^*), and the relative spectrum. The implementation of algorithms for calculating these quantities allows a preliminary classification of the sea state during data saving based on the ψ^* value, for example, identifying sea states related to pure wind waves. When a condition of

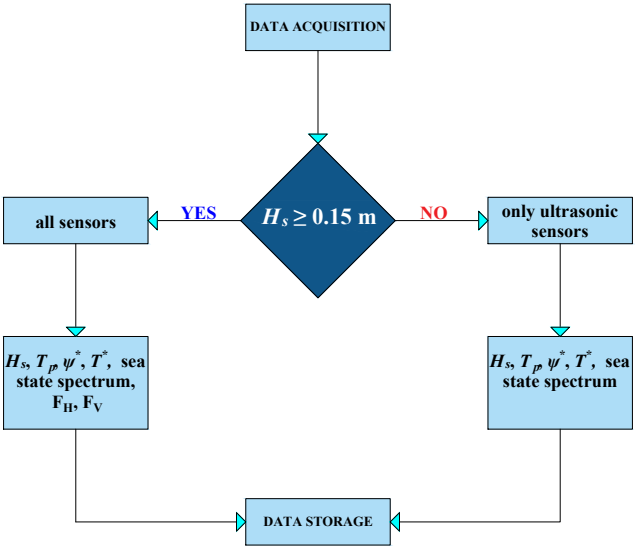

Figure 3.7: Flow chart of the acquisition process.

$H_s > 0.15$ m is detected, the system stops the first task and run automatically the second task, which involves acquiring all sensors: in addition to the ultrasonic sensors, the pressure ones are also acquired. This structure has a dual advantage: on the one hand, it reduces memory usage (smaller files) and, on the other hand, preserves the duration and reliability of the pressure sensors. Indeed, in conditions of low-interest sea states for calculating the forces acting on the cylinders, they are powered off, ensuring lower energy consumption and improving the robustness and reliability of the measurement system by preserving them from drift phenomena related to prolonged use. Note that the ultrasonic sensors are always running, to constantly evaluate sea conditions and for the previously mentioned considerations, because each restart requires a non-negligible warm-up time to avoid worsening of the sensor's accuracy specifications.

In addition to the 5 min acquired sea states files, the system saves also daily summary files where the previously described parameters (H_s, T_p, ψ^* and T^*) are saved for each acquired data packet, with a timestamp. These files provide an overview of sea conditions on daily windows to quickly select specific conditions of interest, thus facilitating the post-processing phase.

3.4 Artificial roughness design

As detailed in Chapter 2, many authors focused their attention in evaluating the effects of marine fouling on the hydrodynamic forces under different types of waves on cylindrical structures. In coastal waters, the marine biofouling is generally composed by barnacles and algae (Fig. 1.4). As well stressed by Thomason et al. [64], the presence of barnacles has effects in the flow field over the structures and, consequently, in the horizontal and vertical forces. Owing to the lack of studies on the effects

on barnacles on wave forces, this type of hard marine fouling has been chosen in the present research. The common type of barnacles that can be found is the "Balanus ampherite" (Fig. 3.8). This is a cone-shaped sessile barnacle, which is spread across most of the seas in Europe. To reproduce the barnacles over the cylinder (Fig. 3.9a), a 3D CAD model was made. In particular, the roughness was realized by a grid of barnacles designed as truncated shape cave cones with a circular base of 7.0 mm of diameter and an height of 3.5 mm (Fig. 3.8b). The coverage ratio of the barnacles, calculated as the ratio between the area occupied by barnacle bases and its influence area (highlighted by a dotted red line in Fig. 3.8b) is 39%. This coverage ratio proves to be in the range of other similar experiments (e.g., [32]). The scaled height of the current roughness was determined in accordance of what found on an offshore structure in the North Sea by [1]. The artificial marine growth was built using a 3D printer ($WASP$ Industrial) with Polylactic Acid Filament (PLA) and gluing it over the surface of the cylinder with a special sealant for the marine environment.

3.5 The experimental dataset

A total number of approximately 8000 tests, characterized by a broad range of wave conditions (pure wind-waves and wind-waves superimposed by swells), was carried out during the experimental campaign. More than 4880 representative pure wind-wave tests, each lasting 5 min, were extracted from that dataset for training the neural network model in evaluating the probability density function of the wave forces. Another dataset of 107 representative tests, having a similar wave direction and characterized by pure wind-waves, was extracted. The above specific tests were chosen avoiding repetitions and forming a balanced set to test the effectiveness of Morison and

Figure 3.8: Real barnacles ("Balanus ampherite") on an iron structure in France.

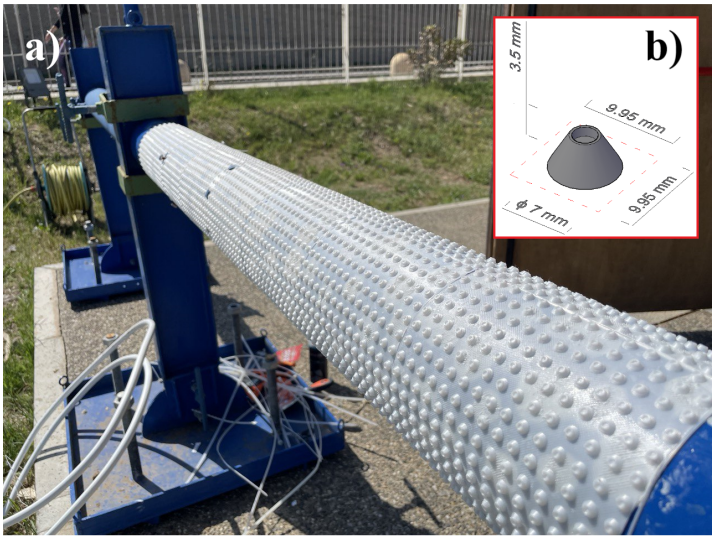

Figure 3.9: (a) The reproduced barnacles on the cylinder; (b) Dimensions of the adopted barnacles.

transverse equations in the evaluation of the wave loads induced by random waves on a horizontal cylinder covered by barnacles. As previously mentioned, only tests characterized by pure wind-waves were chosen through the methodology illustrated in Chapter 4.

The considered sea states were characterized by significant wave heights H_s ranging from 0.18 m to 0.70 m, peak periods T_p ranging from 2 s to 3.8 s, mean wave directions θ ranging from 330° to 29°, Keulegan-Carpenter numbers KC ranging from 2.68 to 14.46 and Reynolds numbers Re ranging from $2.09\text{x}10^4$ to $5.50\text{x}10^4$. The Froude scale of the installation and of the adopted roughness was 1:10.

CHAPTER 4

Methodology

4.1 Wind-generated waves

Mostly of the waves that it is possible to frequently see at sea are wind-generated waves. Looking at the sea, the free surface elevation $\eta(t)$ represents the instantaneous displacement above or below the sea water level. Between two zero-up or down crossing points it is possible to define a single wave. The period is the interval between the two extreme zero up-crossing or down-crossing points. The crest is the local maximum and the wave through is the local minimum, while the height is the distance between the crest and the trough if the zero up-crossing method is considered. A long time series of stationary wind waves can be called sea state. Let us imagine to have N consecutive set of waves and we estimate the mean values of height and period for each set as follows: $\bar{H}_1$, $\bar{T}_1$, $\bar{H}_2$, $\bar{T}_2$,...,$\bar{H}_N$ and $\bar{T_N}$. For a small value of N, the mean value of height and period can be really different from one another. For $N \to \infty$, the differences tend to vanish and the pairs will become equal.

A real sea state can be thought as a succession of 200-300 wind waves. So, the real sea state is nearly stationary and it is long enough to be thought as a sequence from an ideal state. Boccotti [13] proposed that, for the Reggio Calabria site, the

best duration of a real sea state is about one hundred waves. This can also be demonstrated, for the present work, by taking into account the time series of surface elevation recorded for one of the conducted tests. From the wave record we can obtain a number of sequences of $N/2$ consecutive waves. So that the first sequence goes from the first recorded wave to the number of waves equal to $N/2$. The second sequences goes from $N/2+1$ to N and so on. For each sequence, we need to calculate the root mean square value σ_i of the surface elevation. After that let us introduce a random variable as

$$V_i = \frac{\sigma_i + 1}{\sigma_i} - 1 \tag{4.1}$$

and we obtain the variance of this variable

$$\bar{V_i^2} = \frac{1}{n-1} \sum_{i=1}^{n-1} V_i^2 \tag{4.2}$$

with n equal to the number of sequences of $N/2$ waves. Changing N several times, with N an even number, it is possible to obtain the following function

$$\sqrt{\bar{V_i^2}} = f\,(N) \tag{4.3}$$

Looking at the Fig. 4.1 we can see that the minimum of the function, showing the differences between the first half and the second half of sequence of N waves. For the tests conducted is about 140 waves. Due to that and considering the typical wave characteristics for the considered site in terms of wave periods, in the present work each test has a duration of 5 minutes.

For a fixed point, the surface elevation η can be calculated as sum of many N small periodic waves, considering the Stokes expansion at the first order of approximation ([13]).

$$\eta(t) = \sum_{i=1}^{N} a_i \cos(\omega_i t + \tilde{\epsilon_i}), \tag{4.4}$$

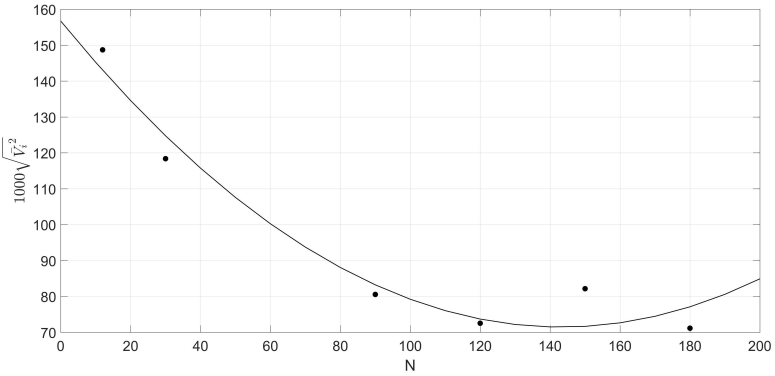

Figure 4.1: Best duration of a real sea state through a sequence of N waves (Reggio Calabria site)

and the velocity potential as

$$\phi(t) = g \sum_{i=1}^{N} a_i \omega_i^{-1} \frac{\cosh[k_i(d+z)]}{\cosh(k_i d)} \sin(\omega_i t + \tilde{\epsilon_i}), \tag{4.5}$$

where

$$\tilde{\epsilon_i} \equiv -(\epsilon_i + k_i x \sin\theta_i + k_i y \cos\theta_i), \tag{4.6}$$

where t is the time, x, y and z are the coordinate axes (defined in Fig. 3.2), k_i is the wave number, a_i is the wave amplitude, ω_i is the angular frequency, ϵ_i is the phase angle and θ_i is the wave direction. The linear dispersion relationship between k_i and ω_i is

$$k_i \tanh(k_i d) = \frac{\omega_i^2}{g}. \tag{4.7}$$

In general, we recorded three different types of sea states during the experimental campaign. The first family is characterized by wind-generated waves, the second is characterized

by wind waves superimposed to swells, and the last is characterized just by swell waves (characterized by small amplitudes and long periods). These waves can spoil the dynamic similarity of the small scale tests. As stressed by Boccotti [14] and Boccotti [65], the site of Reggio Calabria is a quite unique, because often sea states characterized by pure wind-waves with characteristics comparable to those obtainable in large laboratory tanks occur. In this work, sea states formed by pure wind-generated waves were selected. To check if a sea state is characterized just by pure wind-waves, we refereed to the narrow bandedness parameter ψ^* [14], calculated as

$$\psi^* = |\psi(T^*)/\psi(0)|, \tag{4.8}$$

where ψ is the autocovariance of the instantaneous surface elevation and T^* is the abscissa of the absolute minimum of the autocovariance function. This index is complementary to the one introduced by Cartwright and Longuet-Higgins [66], that can be used to inspect the nature of the waves and how much they tend to differ from the ideal condition of narrow spectrum. The value of ψ^* approaches to 1 as the bandwidth of the spectrum decreases and the autocovariance function tends to a cosine shape. Otherwise, it decreases and tends to 0. For pure wind-waves, the typical range of ψ^* is between 0.65 and 0.75. To better understand the nature of a sea state, a good practice is to compare ψ^* of the surface waves with the value of ψ^* of the pressure head waves beneath the surface. For the case of pure wind-waves, the spectrum becomes narrow from the water surface to the sea bed since the water depth acts as a low-pass filter. This lead to a larger value of ψ^*. The opposite occurs when we have wind-waves superimposed to swells, because the latter are less attenuated along the depth, due to the wave periods larger than the wind-waves ones.

In Fig. 4.2, the autocovariance and the spectrum of a cross sea state (i.e. characterized by wind-waves superimposed to

swells) is shown. The autocovariance (Fig. 4.2a) and the frequency spectrum of the surface waves (Fig. 4.2b) are obtained using the records of an ultrasonic sensor, while the autocovariance (Fig. 4.2c) and the spectrum of the pressure head waves (Fig. 4.2d) are given by the records of the pressure transducer no. 1 (see Fig. 3.4a) located on the wave-beaten side of the smooth cylinder. Looking at Figs. 4.2a and 4.2b, we would be tempted to conclude that this is a well-scaled sea state characterized by pure wind-waves, since the energy contents of the part of spectrum relevant to the surface waves are quite larger than those related to the swells. However, it is possible to notice that the energy contents of the swells, noticed for a small bump in the spectrum of the surface waves, increase going down from the free surface (Figs. 4.2c and 4.2d). The scaled peak period of the pressure head wave is, in this example, about 15 s that spoils the Froude similarity of the tests and it is not realistic for a prototype. An example of one of 107 records of pure wind waves, used in this work, is instead shown in Fig. 4.3. Here too, ψ^* falls in the typical range of wind-waves, both for the autocovariance obtained for the surface waves (Fig. 4.3a) and for the one of the pressure head waves (Fig. 4.3c). It is also clear that all the energy contents belonging to the surface waves, with no peaks in low frequencies, also going from the surface to beneath it (Figs. 4.3b and 4.3d). It is worth noting that ψ^* increases going down from the free surface. This example test and the others chosen in this work, as said before, are perfectly scalable maintaining the Froude similarity, as the tests that could be obtained in laboratory tanks.

4.2 Directional wave spectrum

To obtain the directional wave spectrum, a common practice is to find a directional distribution, through a best-fit analy-

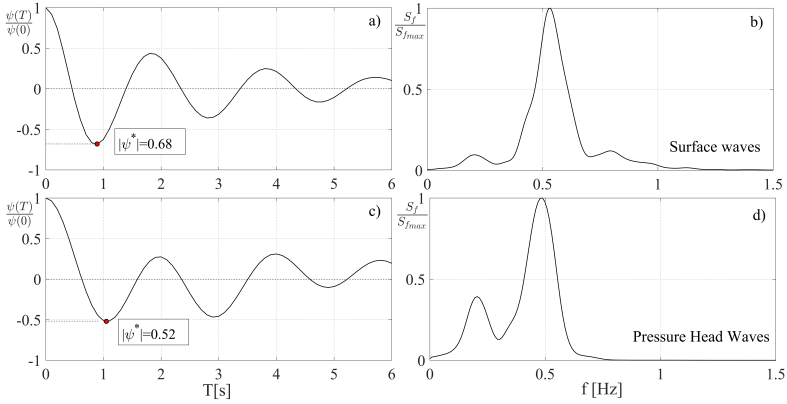

Figure 4.2: Autocovariance and spectrum for a test of wind-waves superimposed to swell waves ($H_s = 0.25$ m, $T_p = 1.9$ s) (both functions have been normalized).

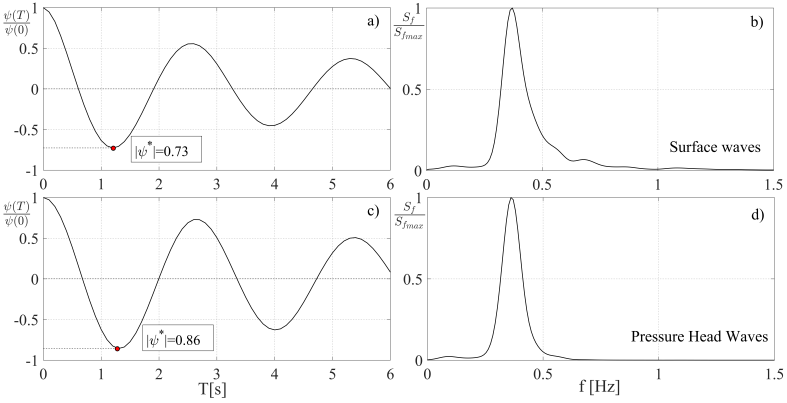

Figure 4.3: Autocovariance and spectrum for a test of pure wind-waves ($H_s = 0.55$ m, $T_p = 2.7$ s) (both functions have been normalized).

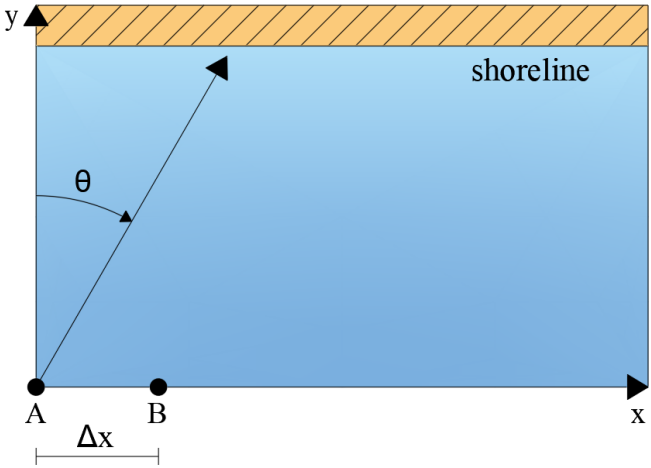

Figure 4.4: Advance wave angles (positive clockwise)

sis, for each frequency ω_i. This approach was introduced by Longuet-Higgins et al. [67].

To determine the directional wave spectrum for this thesis, starting from the time series of surface elevation at two fixed points, we used the method by [14]. The aim of this analysis is to determine the direction θ of a wave belonging to a sea state.

We assume an x-axis parallel to the coast, and to the longitudinal axis of the cylinders. In two fixed points along it, named respectively A and B, two ultrasonic probes at a mutual distance $\Delta x = 1.5$ m were placed (Fig. 4.4). By means of the linear wave theory for irregular waves, we can obtain

$$\eta_A(t) = \sum_{i=1}^{N} a_i \cos(-\omega_i t + \epsilon_i), \tag{4.9}$$

$$\eta_B(t) = \sum_{i=1}^{N} a_i \cos(k_i \Delta x \sin\theta_i - \omega_i t + \epsilon_i). \tag{4.10}$$

From the two time series of the surface elevation, recorded by the two ultrasonic probes on the structure, it is possible to obtain the corresponding Fourier series [14]. As a result, the reconstruction of the directional wave spectrum (see example in Fig. 4.5) is obtained as follows

$$\eta_A(t) = \sum_{i=1}^{N} A_i^{'} \cos(\omega_i t) + A_i^{''} \sin(\omega_i t), \tag{4.11}$$

$$\eta_B(t) = \sum_{i=1}^{N} B_i^{'} \cos(\omega_i t) + B_i^{''} \sin(\omega_i t), \tag{4.12}$$

where

$$A_i^{'} = a_i \cos \epsilon_i, \tag{4.13}$$

$$A_i^{''} = a_i \sin \epsilon_i, \tag{4.14}$$

$$B_i^{'} = a_i \cos(k_i \Delta x \sin \theta_i + \epsilon_i), \tag{4.15}$$

$$B_i^{''} = a_i \sin(k_i \Delta x \sin \theta_i + \epsilon_i). \tag{4.16}$$

Due to fact that we know, for N simple waves, the N quadruplets $A_i^{'}$, $A_i^{''}$, $B_i^{'}$, $B_i^{''}$ and the N angular frequencies ω_i we can obtain the values of the amplitudes a_i, phase angle ϵ_i and θ_i from

$$a_i = \sqrt{A_i^{'2} + A_i^{''2}}, \tag{4.17}$$

$$\sin \epsilon_i = \frac{A_i^{''}}{a_i}, \tag{4.18}$$

$$\cos \epsilon_i = \frac{A_i^{'}}{a_i}, \tag{4.19}$$

$$\tan(k_i \Delta x \sin\theta_i) = \frac{A_i^{'} B_i^{''} - A_i^{''} B_i^{''}}{A_i^{'} B_i^{'} + A_i^{''} B_i^{''}}. \tag{4.20}$$

Finally, it is possible to reconstruct the directional wave spectrum (Fig. 4.5) as

$$S(\omega, \theta)\Delta\omega\Delta\theta = \sum_{i=1}^{N} \frac{1}{2} a_i^2, \tag{4.21}$$

with

$$\begin{cases} \omega - \Delta\omega/2 < \omega_i < \omega + \Delta\omega/2, \\ \theta - \Delta\theta/2 < \theta_i < \theta + \Delta\theta/2. \end{cases} \tag{4.22}$$

where $\Delta\omega$ and $\Delta\theta$ represent selected windows associated with ω and θ to model the directional wave spectrum.

It is worth to observe that, looking at the directional spectrum shown in Fig. 4.5, the range of the directions of the waves are between the typical range for the site ($330°N - 60°N$) and the frequency f is used. In this example, the peak direction is nearly centered on the North. It is also possible to observe an asymmetry in the directional spreading of the spectrum because of the prevailing influence of the waves coming from North-North-East direction and, specifically, from the entrance to the Strait of Messina. This because the structure is oriented parallel to the coast and the wave direction of the pure wind-waves are generally from Messina to Reggio Calabria, acting quite orthogonally to the longitudinal axis of the cylinders.

4.3 Determination of experimental wave forces

The horizontal F_H and vertical F_V wave loads acting on the smooth and rough cylinder were deduced from the eight pressure transducers mounted in the middle of each cylinder at 45°

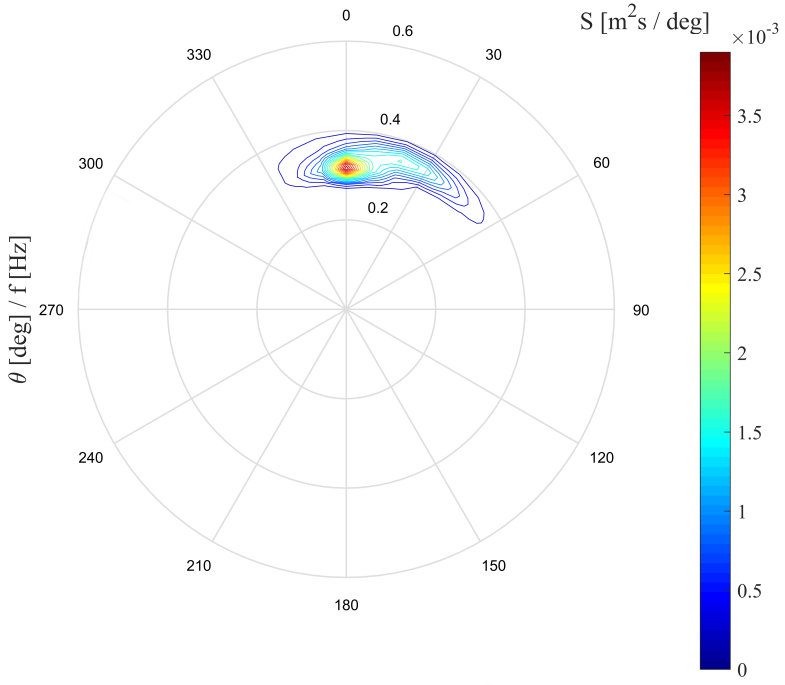

Figure 4.5: Directional wave spectrum for pure wind-waves ($H_s = 0.43$ m, $T_p = 2.8$ s).

intervals (Fig. 3.4a). To determine the hydrodynamic forces, we assume that the dynamic pressure Δp is constant over 1/8 of the circumference. This quantity was calculated by subtracting the static pressure p_s=-$\gamma_w z$ from the record of the total pressure p, where γ_w (specific weight) $\approx$ 10104 N/m^3, and z (negative below the free surface) is the generic distance from the SWL to the center of the transducer head. For F_H and F_V, we then obtain the following relationships

$$\begin{aligned} F_H(t) =& A_x \left[\Delta p_1(t) + \Delta p_8(t) - \Delta p_4(t) - \Delta p_5(t)\right] \\ &+ B_x \left[\Delta p_2(t) + \Delta p_7(t) - \Delta p_3(t) - \Delta p_6(t)\right], \end{aligned} \tag{4.23}$$

$$\begin{aligned} F_V(t) =& A_z \left[\Delta p_6(t) + \Delta p_7(t) - \Delta p_2(t) - \Delta p_3(t)\right] \\ &+ B_z \left[\Delta p_5(t) + \Delta p_8(t) - \Delta p_1(t) - \Delta p_4(t)\right], \end{aligned} \tag{4.24}$$

where the influence areas A_x, B_x, A_z and B_z are respectively calculated as a function of the position of the transducers (see Fig. 3.4a) as follows

$$A_x = A_z = \left(\frac{1}{2} - \frac{\sqrt{2}}{4}\right) D, \tag{4.25}$$

$$B_x = B_z = \frac{\sqrt{2}}{4} D. \tag{4.26}$$

4.4 Kinematic field

From the time series of surface elevation recorded by the ultrasonic probes, it is possible to obtain, for each elementary component, the values of amplitude a_i, angular frequency ω_i and phase angle ϵ_i of each i-th elemental wave. The directions θ_i can be obtained, as explained before, from the time series evaluated by the two ultrasonic probes. Then, we can obtain

the time series of particle velocities and accelerations, at the center of the circular section of the cylinders, according to [65] as

$$v_y(t) = g\sum_{i=1}^{N} a_i A_i(z_c)\frac{k_i}{\omega_i}\cos(\theta_i)\cos(-\omega_i t + \epsilon_i), \tag{4.27}$$

$$v_z(t) = g\sum_{i=1}^{N} a_i B_i(z_c)\frac{k_i}{\omega_i}\sin(-\omega_i t + \epsilon_i), \tag{4.28}$$

$$a_y(t) = g\sum_{i=1}^{N} a_i A_i(z_c) k_i \cos(\theta_i)\sin(-\omega_i t + \epsilon_i), \tag{4.29}$$

$$a_z(t) = g\sum_{i=1}^{N} a_i B_i(z_c) k_i \cos(-\omega_i t + \epsilon_i), \tag{4.30}$$

where

$$A_i(z) = \frac{cosh\left[k_i(d+z)\right]}{cosh(k_i d)}, \tag{4.31}$$

$$B_i(z) = \frac{sinh\left[k_i(d+z)\right]}{cosh(k_i d)}, \tag{4.32}$$

$$k_i tanh(k_i d) = \frac{\omega_i^2}{g}, \tag{4.33}$$

in which z_c is the distance from the SWL to the cylinder centre. In this case, z_c = -0.95 m.

4.5 Morison and transverse semi-empirical equations for short-crested waves

For short-crested waves, the Morison equation was rearranged by Boccotti [65] to consider the contribution of the velocity components, v_y and v_z, in assessing the drag component. As a result, the horizontal force is expressed as

$$F_{Hm}(t) = F_D(t) + F_{HI}(t) = \frac{1}{2}\rho C_D D\sqrt{v_y(t)^2 + v_z(t)^2}v_y(t) + \frac{\pi}{4}D^2\rho C_{MH}a_y(t), \tag{4.34}$$

where C_D is the drag coefficient and C_{MH} is the horizontal inertia coefficient. The undisturbed values of v_y, v_z, a_y and a_z are calculated at the cylinder centre, as highlighted in Section 4.4.

To evaluate the vertical force induced by wind generated waves, the transverse scheme was used (e.g., [12]). The vertical force is evaluated as a sum of a lift component F_L, due to the increase of the velocity across the cylinder caused by the flow blockage, and a vertical inertia component, depending in this case on the vertical acceleration. Along the lines of the horizontal force, Boccotti [65] rearranged the transverse equation to consider the effect of both components of velocity in assessing the lift force component. The vertical force is calculated as

$$F_{Vm}(t) = F_L(t) + F_{VI}(t) = \frac{1}{2}\rho DC_L\sqrt{v_y(t)^2 + v_z(t)^2}v_z(t) + \frac{\pi}{4}D^2\rho C_{MV}a_z(t) \tag{4.35}$$

where C_L is the lift coefficient and C_{MV} is the vertical inertia coefficient.

4.6 Keulegan-Carpenter and Reynolds numbers

Since we are dealing with random waves, we resort to the definition of KC made by Boccotti [65] for a sea state. The authors proposed to relate KC to the quotient between drag and horizontal inertia forces as follow

$$KC = \pi^2 \sqrt{4/3} \sqrt{\frac{\langle f_D(t)^2 \rangle}{\langle f_{HI}(t)^2 \rangle}}, \tag{4.36}$$

where $\langle f_D(t)^2 \rangle$ and $\langle f_{HI}(t)^2 \rangle$ are the temporal mean of the square of the drag and horizontal inertia forces

$$f_D(t) = \frac{1}{2} \rho D \sqrt{v_y(t)^2 + v_z(t)^2} v_y(t), \tag{4.37}$$

$$f_{HI}(t) = \frac{\pi}{4} D^2 \rho a_y(t). \tag{4.38}$$

As for Eq. 4.36, we resort to the definition of the Reynolds number introduced by Boccotti [65] as follows

$$Re = \frac{KCD^2}{\nu T_p}, \tag{4.39}$$

where ν is the kinematic viscosity.

4.7 Propagation of uncertainty in the force calculation

The standard uncertainty, σ_P, associated with the instantaneous measurement of the pressure is the same for all the transducers, because they are all the same model. The evaluation of σ_P can be derived from the manufacturer specification, generally expressed in terms of absolute error E_P. In absence of information about polarization within the error interval, we

assume that measurements are distributed uniformly and, consequently, we have

$$\sigma_P = \frac{E_P}{\sqrt{3}}, \tag{4.40}$$

where EP is the half of error interval, expressed as a fraction of the full-scale range (FS). In this case, we have

$$E_P = 0.2\%FS = 0.002 * 400mbar = 0.8mbar, \tag{4.41}$$

and, consequently,

$$\sigma_P = \frac{E_P}{\sqrt{3}} = 0.46mbar. \tag{4.42}$$

Horizontal and vertical forces on the cylinder are linearly dependent by the wave pressures recorded by the eight transducers, as we can see in Eqs. 4.23 and 4.24, respectively. Indeed, the terms A_x, B_x, A_z and B_z depend only on geometry. Assuming that the measurements of the different pressure sensors are independent and uncorrelated, it follows that the combined uncertainty relative to the calculation of the horizontal forces, σ_{FH}, is

$$\sigma_{FH}^2 = 4A_x^2\sigma_P^2 + 4B_x^2\sigma_P^2, \tag{4.43}$$

$$\sigma_{FH} = 2\sqrt{A_x^2 + B_x^2}\sigma_P, \tag{4.44}$$

and, similarly, for the vertical forces, σ_{FV}, is

$$\sigma_{FV} = 2\sqrt{A_x^2 + B_x^2}\sigma_P. \tag{4.45}$$

Being $A_x = A_z = 0.019$ m and $B_x = B_z = 0.045$ m, it follows that the uncertainty in the force calculation, U_F, is

$$U_F = \pm\sigma_{FH} = \pm\sigma_{FV} = \pm 4.5N/m. \tag{4.46}$$

CHAPTER 5

Deep learning application to the force analysis

Two different approaches were used during this thesis. In the first one, neural networks are used to predict the values of the 95^{th} percentile of the horizontal and vertical forces induced by wind-generated waves on the smooth and rough cylinder using the current field tests. In the second one, neural networks were involved in the prediction of the values of the means and the standard deviations of the time series of the hydrodynamic forces. This in order to reconstruct, with this model, the probability density function of the horizontal and vertical forces, both for the smooth and for the rough cylinder, at a given value of H_s and T_p. The reconstruction of PDF can be used to compare the values of the percentiles calculated with the first method with the ones extracted with this second method. All the results can be also compared with the experimental results.

In both cases, the used database refers to the results obtained experimentally from 4865 field tests. Before applying the models, the data were cleaned by outliers. To define a sea state, the input data chosen was the significant wave height H_s and the peak period T_p. Looking at the Fig. 5.1, it appears clear that some values exceed the characteristics of pure

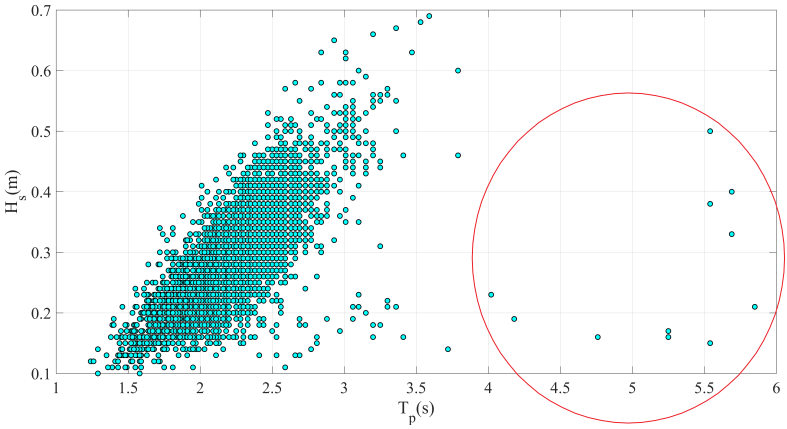

Figure 5.1: Database of H_s and T_p as input of the neural network models (the cleaned outliers are highlighted by a red circle).

wind-waves of the site (e.g., T_p is greater than 4 seconds), as explained in the previous Chapter. These values have been excluded from the dataset.

5.1 FNN to predict the 95^{th} percentile of the wave forces

The first approach concerned the use of a feedforward neural network (FNN) in predicting the features of the forces induced by wind-generated waves on a smooth and a rough cylinder covered by artificial barnacles. As stated, the ANN was trained giving as input the wave characteristics (e.g., H_s and T_p) and predicting the 95^{th} percentile of the horizontal and vertical forces both for the smooth and the rough cylinder. The 95^{th} percentile of a probability density function (PDF) is a value, denoted as x_{95}, below which 95% of the data in a given distribution fall. In other words, it is the value at which the

cumulative distribution function (CDF) reaches 0.95. Mathematically, if $F(x)$ is the CDF corresponding to the PDF $f(x)$, the 95th percentile x_{95} is defined as

$$F(x_{95}) = \int_{-\infty}^{x_{95}} f(x)\,dx = 0.95, \tag{5.1}$$

Specifically, $f(x)$ describes the likelihood of a random variable taking on a particular value, and $F(x)$ represents the probability that the random variable is less than or equal to x. In this case, we will refer to the Rayleigh distribution, which well represents the distribution of random wave heights in a sea state, as found by Boccotti [13] for the Reggio Calabria site. Let us introduce the PDF of the Rayleigh distribution

$$f(x_f;\sigma_f) = \frac{x_f}{\sigma_f^2} e^{-\frac{x_f^2}{2\sigma_f^2}}, \quad x_f \geq 0 \tag{5.2}$$

where x_f is the set of possible values that can be assumed by the current force process modeled by the Rayleigh distribution. The value of σ_f is the standard deviation of the force process for each test. To find the 95^{th} percentile starting from the PDF of the Rayleigh distribution, firstly we need to calculate the cumulative density function (CDF) of the distribution as

$$F(x_f;\sigma_f) = 1 - e^{-\frac{x_f^2}{2\sigma_f^2}}, \tag{5.3}$$

so that

$$0.95 = 1 - e^{-\frac{x_{95}^2}{2\sigma_f^2}}, \tag{5.4}$$

The 95^{th} percentile can be then obtained from

$$x_{95} = \sigma_f \sqrt{-2\ln(0.05)}. \tag{5.5}$$

In Fig.5.2 an example of the PDF of the Rayleigh distribution with $\sigma_f = 1$ is shown. The red dashed line marks the 95^{th}

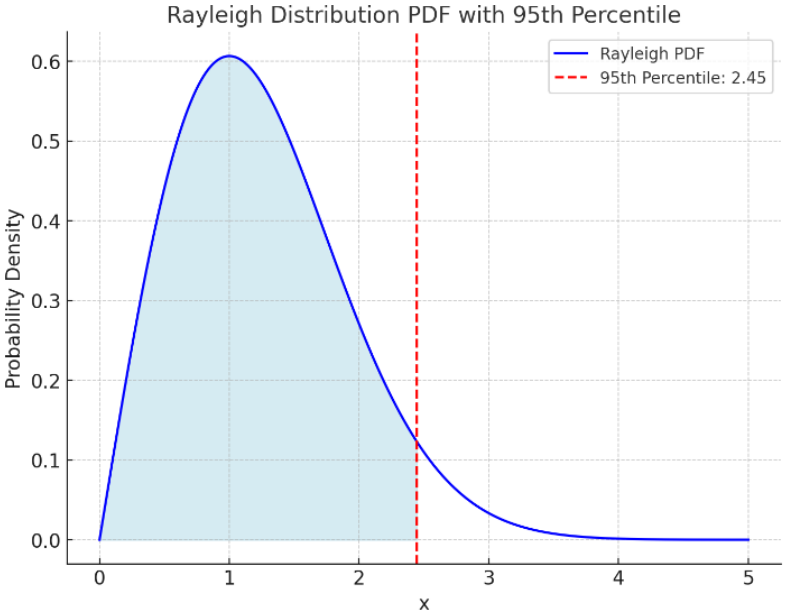

Figure 5.2: PDF of the Rayleigh distribution.

percentile. The shaded region represents 95% of the distribution's probability mass, showing that most of the values lie below this threshold.

The choice of the 95^{th} percentile of the hydrodynamic forces is motivated by the fact that other values, such as the maximum force, can be affected by errors resulting from spikes in the signals due to instrument reading problems. Once the input x values (H_s and T_p) and output y values ($95^{th}F_{Hs}$, $95^{th}F_{Hr}$, $95^{th}F_{Vs}$ and $95^{th}F_{Vr}$) of the network are known, the next step is to split the dataset. The database was splitted as:

- 60% of the data was adopted for training, that represents the largest portion of the data used to train the neural network [68]. It is the dataset that the model learns from by adjusting its weights and biases to minimize the error between its predictions and the actual outputs. During training, the model iteratively updates its parameters to improve its accuracy on this dataset.

- 20% of the data was used for the validation. It is a separate subset of data used to evaluate the model during the training process. It helps in fine-tuning the model's hyperparameters (e.g., learning rate, number of layers, batch size) and provides an unbiased evaluation of the model's performance during training. The validation dataset is not used for updating the model weights but rather for monitoring the model's ability to generalize to unseen data, allowing for early stopping to prevent overfitting. Generally overfitting in neural networks occurs when the model learns the training data too well, capturing noise and outliers instead of the underlying pattern. This leads to poor performance on new, unseen data because the model is too complex and specific to the training set [69].

- The last 20% of the data was used for the test. It is used

to evaluate the final performance of the neural network after the training process is complete. It is never used during the training or validation phases. The test dataset provides a final and unbiased assessment of the model's ability to generalize to new and unseen data, and its performance on this dataset reflects how well the model is expected to perform.

Once the database has been split, the next step is to standardize the inputs. This process is mandatory because it ensures that all datasets have the same scale, that is crucial for many machine learning algorithms that assume features are centered around 0 and have the same variance. By fitting the scaler only on the training data and applying it to the validation and test sets, the code avoids data leakage and ensures that the model is evaluated on data standardized in the same way it was trained. A Standard Scaler from the scikit-learn library was used [70]. This scaler transforms the data so that the resulting distribution has a mean of 0 and a standard deviation of 1. The transformed value is calculated by subtracting the mean from the original value and then dividing by the standard deviation. The transformation is performed using the following formula

$$j = \frac{\delta - \mu}{\sigma}, \tag{5.6}$$

where j is the transformed value of the feature, δ is the original value, μ is the mean and σ is the standard deviation.

5.1.1 Architecture of the neural network

A feedforward artificial neural network was used (see Chapter 2.5). As already defined, the input data were the wave characteristics for a given sea state (H_s and T_p). The output was, at a fixed input, the 95^{th} percentile of the horizontal and vertical forces induced by the waves on the smooth cylinder

($95^{th}F_H^s and 95^{th}F_V^s$) and the ones on the cylinder covered by barnacles ($95^{th}F_H^r and 95^{th}F_V^r$). As sketched in Fig. 5.3, the data flows only in one direction from input to output. It can be summarized as follows

- the input layer does not perform any computation; it merely defines the shape of the input data that the model will receive. It is composed by two neurons, i.e. one for the significant wave height and one for the peak period.

- the first hidden layer is a fully connected layer with 32 neurons. Each neuron in this layer will connect to all the neurons in the preceding (input) layer. The Rectified Linear Unit (ReLU) activation function is applied to the output of each neuron in this layer. ReLU is a popular choice for hidden layers because it helps to mitigate the vanishing gradient problem [71], allowing the model to learn complex patterns. The ReLU function is mathematically defined as:

$$ReLU(c) = max(0, c), \tag{5.7}$$

  where c is the input to the activation function. If c is greater than 0, the function returns c. Otherwise, the function returns 0. The function is linear for all positive input values and flat for all negative values. This simple yet effective property allows neural networks to learn quickly with less complexity compared to other activation functions. A Kernel Regularizer L2 is applied to the layer's weights from Keras library [72]. The regularization helps in preventing overfitting by penalizing large weights. The regularization term is set, in this case, to 0.01. This is a hyperparameter that controls the extent of the penalty applied to large weights. A dropout was also included [72]. The dropout works in the first hidden layer by randomly dropping out or ignoring (set to zero)

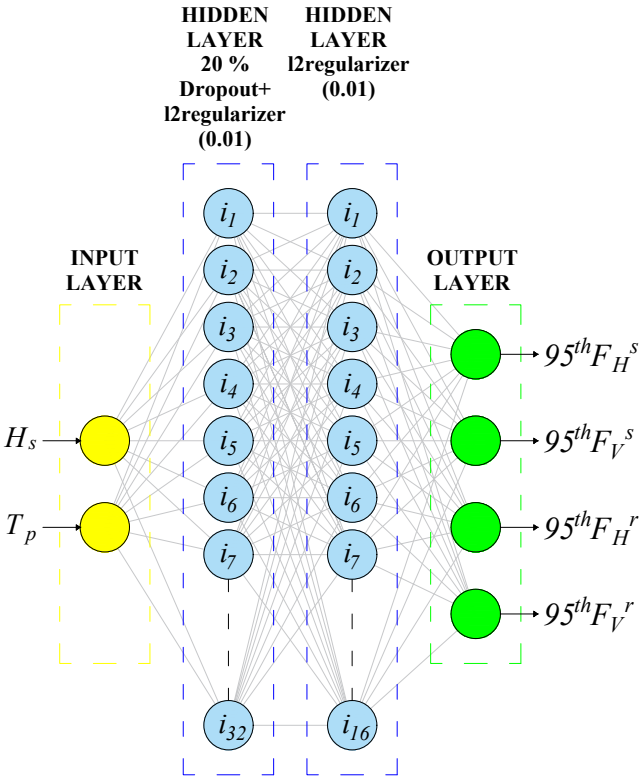

Figure 5.3: FNNs neural network to predict the 95^{th} percentile of the wave forces on the cylinders.

20% of the neurons at each update step. This helps in preventing overfitting by forcing the model to learn more robust features, as it cannot rely on any specific set of neurons to make predictions.

- The second hidden layer is formed by 16 fully-connected artificial neurons. Also in this layer, the same activaction function is used, as well as the same regularizer (L2(0.01)).

- The output is a fully-connected layer with 4 neurons to predict the four outputs ($95^{th}F_H^s$, $95^{th}F_V^s$, $95^{th}F_H^r$ and $95^{th}F_V^r$).

5.1.2 Performance evaluation of FNN

When compiling the FNN, the Adaptive Moment Estimation optimizer (ADAM) was chosen [72]. The ADAM optimizer combines two methods: Adaptive Gradients (AdaGrad) and Root Mean Square Propagation (RMSProp). Instead of computing the gradient using the entire dataset, ADAM utilizes a randomly selected subset of data (a mini-batch) to produce a stochastic approximation of the gradient. This allows for efficient and scalable updates of the model parameters. ADAM adapts the learning rate for each parameter and requires not so much memory being computationally efficient.

To measure the difference between the model's predicted outputs and the actual target values, the mean squared error (MSE) was chosen as loss function. MSE is commonly used for regression problems and calculates the average of the squared differences between the predicted values and the actual target values as

$$\text{MSE} = \frac{1}{n}\sum_{i=1}^{n}(y_i - \hat{y}_i)^2 \tag{5.8}$$

where y_i is the true value, $\hat{y}_i$ is the value predicted by the ANN, and n is the number of values.

Two metrics were also implemented to check the performance of the model during the training and validation phases. One is the mean absolute error (MAE) computed as

$$\text{MAE} = \frac{1}{n} \sum_{i=1}^{n} |y_i - \hat{y}_i| \tag{5.9}$$

The second metric is the mean squared error (MSE). This means that during training, both the MAE and MSE have been calculated and reported as metrics, even though MSE has been also used as the loss function. These metrics have been added for two reasons

- MAE gives an idea of the average size of the errors in a simple and interpretable way;
- MSE provides additional insight, particularly emphasizing larger errors, which can help to assess how the model performs under different circumstances.

In Fig. 5.4, the training and validation losses are plotted against the epochs of training. Looking at it, some consideration can be done. The initial loss values are high because the model has just started learning. The gap between training and validation loss suggests that the model has not yet generalized well, but this is expected in the early stages. The losses and errors decrease rapidly in the initial epochs, indicating that the model is learning quickly. The fast decline shows that the model is adjusting its weights effectively to reduce errors. From epochs between 10 and 20, the rate of decrease in loss is slowing, that is expected as the model converges. The training and validation losses are close to each other, indicating good generalization and no signs of overfitting ("learning by heart"). The model's loss (both training and validation) decreases quickly, suggesting good convergence. By epoch equal

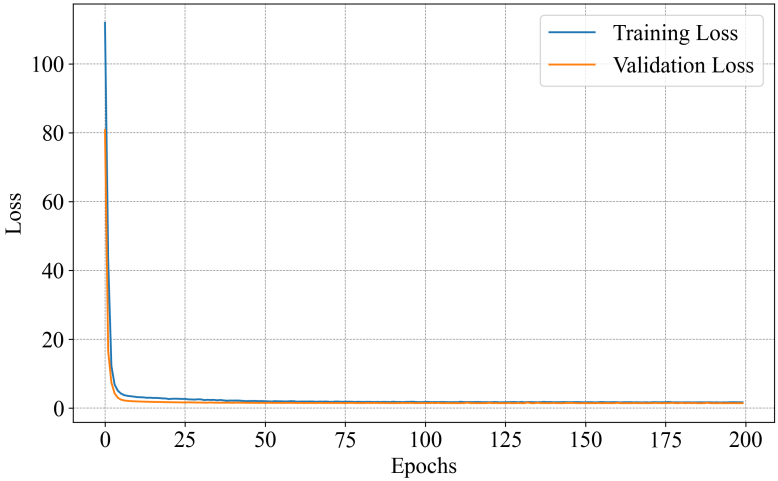

Figure 5.4: Training and validation loss against the epochs of training (first neural network).

to 30, the losses are much lower than at the start, indicating significant learning. It is possible to see the convergence of the model by the epoch larger than 30. The same conclusions can also be made by referring to the metrics graphs during the training and validation phase (Figs. 5.5a and 5.5b). The metrics also as the losses tends to decrease during the epochs as a symptom of network convergence.

5.2 FNN to predict the standard deviation

In order to reconstruct the probability density function of the time series of the wave forces, artificial neural networks were used to predict the values of the standard deviations and the means for each time series of wave forces belonging to a specific sea state. Since these time series have always a mean around

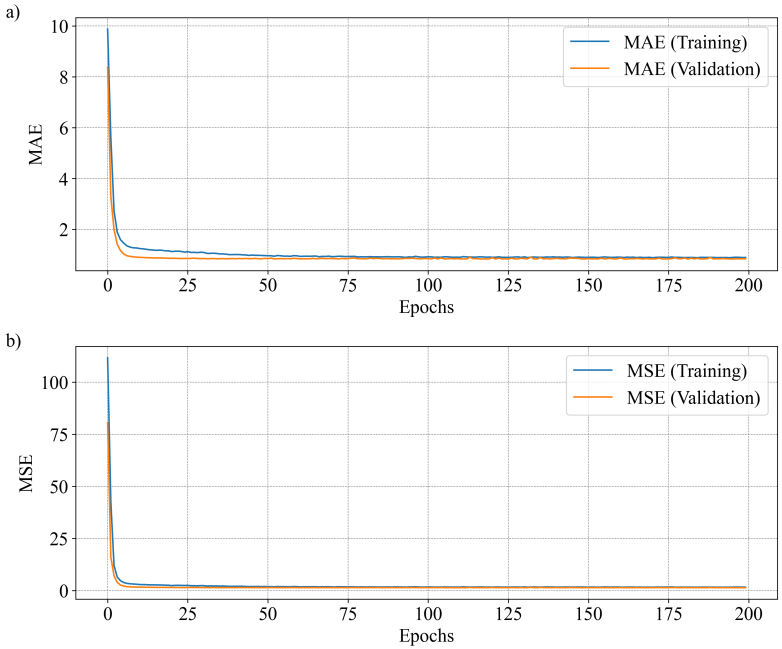

Figure 5.5: a) Training and validation MAE vs epochs; b) Training and validation MSE vs epochs.

zero, it is reported just the feedforward neural network used to predict the values of the standard deviations for the horizontal and vertical forces, both for the smooth and the rough horizontal cylinder. Fig. 5.6 shows the scheme of the neural network used in this case. As for the percentile prediction, a feedforward neural network was chosen. The configuration that performed better is composed by

- an input layer composed by two neurons, i.e. one for the significant wave height and one for the peak period.
- a first hidden fully connected layer with 32 neurons. The Rectified Linear Unit (ReLU) activation function is also applied to the output of each neuron in this layer. A Kernel Regularizer L2 is also applied as well as a 20% dropout.
- The second hidden layer is formed by 16 fully connected artificial neurons with the same activation function and regularizer as the previous one.
- The output is a formed by a fully connected layer with 4 neurons to predict the four outputs ($\sigma_{FH}{}^{s}$, $\sigma_{FV}{}^{s}$, $\sigma_{FH}{}^{r}$ and $\sigma_{FV}{}^{s}$).

5.2.1 Performance evaluation of FNN in predicting the standard deviation

As for the previous neural network, the same optimizer (ADAM), the same loss function (MSE) and the same metrics (MAE and MSE) were chosen to evaluate the performance of this model. Looking at Fig. 5.7, the training and validation losses are plotted against the epochs of training for this second network. Some conclusions can be given. In this case, the initial loss values are high (but lower than the first network) due to the start of the learning process. The gap between training and

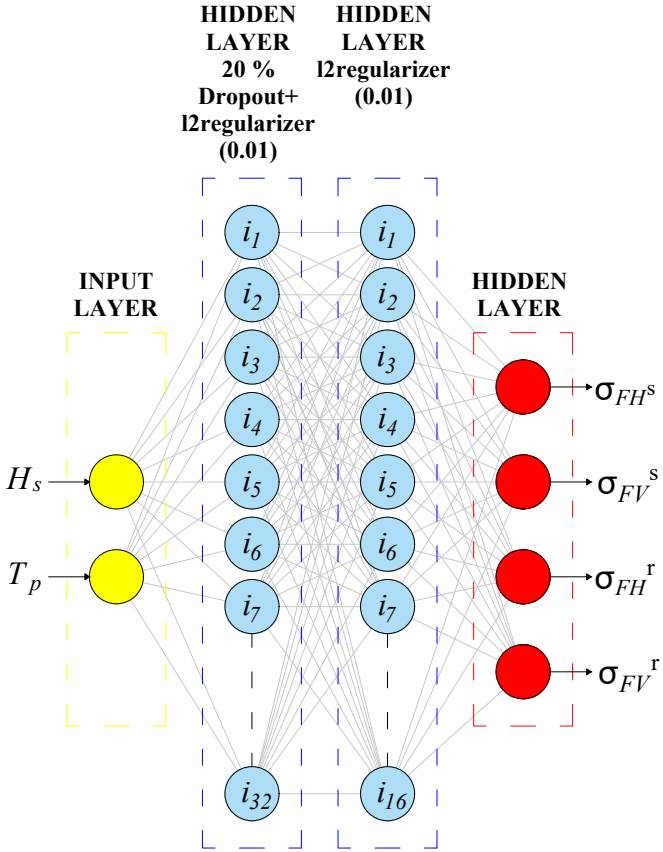

Figure 5.6: FNNs neural network to predict the standard deviations of the wave forces on the cylinders.

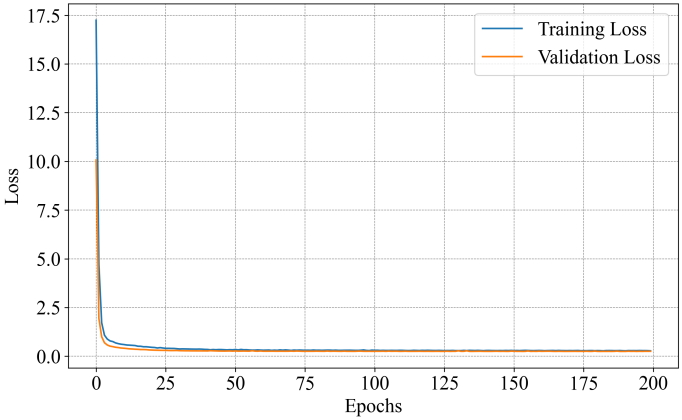

Figure 5.7: Training and validation loss against the epochs of training (second neural network).

validation loss suggests that the model has not yet generalized well. As already noticed, this behaviour is expected in the early stages. The losses and errors decrease rapidly and became slower for epochs ranging between 10 and 25, that is expected as the model converges. The training and validation losses are close to each other. A good generalization of the network can be observed as the model's loss (both training and validation) decreases quickly, suggesting good convergence. It is possible to see the convergence of the model by the epoch greater than 30. The values of losses for this case are a bit lower compared to the first one. This is a sign of a well-trained neural network.

The same conclusions can also be made by referring to the metrics graphs during the training and validation phase (Figs. 5.8a and 5.8b), the metrics as well as the losses tend to decrease during the epochs as a symptom of the network convergence.

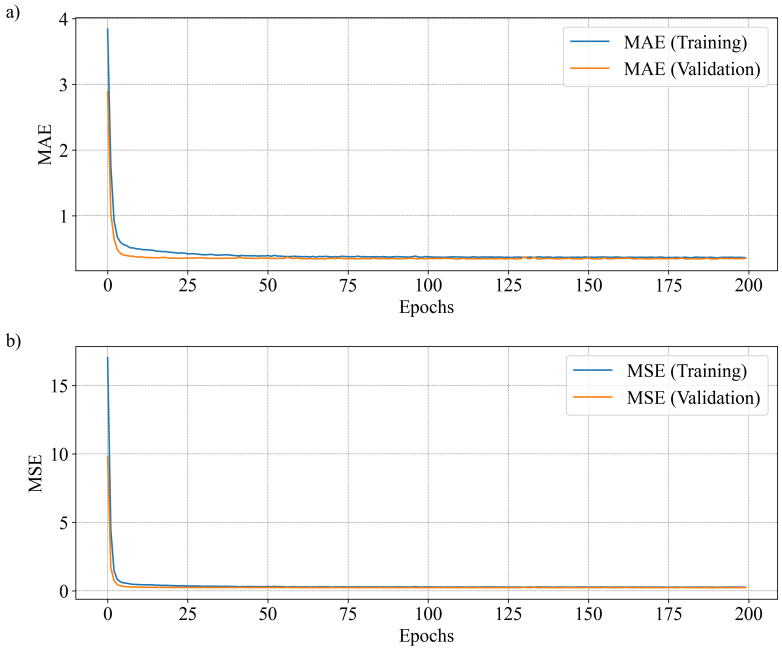

Figure 5.8: a) Training and validation MAE vs epochs; b) Training and validation MSE vs epochs (second case).

CHAPTER 6
Results

6.1 Wave forces

To assess the influence of the roughness on the circular cylinder covered by barnacles, it was firstly checked the measured forces on the smooth and rough cylinder. In Figs. 6.1a and 6.1b, a time window of 100 s of the measured horizontal and vertical forces is respectively plotted both for the smooth and the rough cylinder, normalized by the absolute maximum of the series. The chosen test has $H_s = 0.43$ m and $T_p = 2.8$ s. It is noticeable the effect of the roughness on the magnitude of the horizontal and vertical loads. Indeed, the wave loads at the rough cylinder are generally larger than those observed for the smooth one. If compared to the smooth cylinder, the current roughness causes, for this test, a mean increasing in the peaks of horizontal and vertical forces of 15% and 18%, respectively. This difference is mainly caused by the growth of the cylinder section for the rough case. Moreover, it can be observed, for this case, that the wave forces at the rough cylinder are slightly back shifted if compared to the smooth case, particularly when low peaks occur. This effect could be related to the small different wave directions of the single waves crossing the two cylinders.

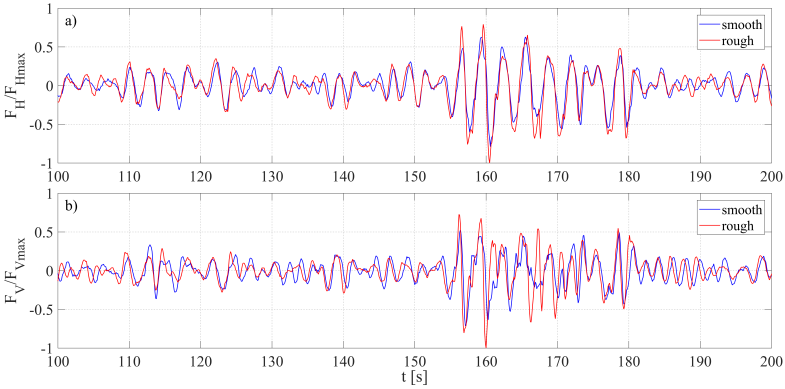

Figure 6.1: Time series of measured hydrodynamic forces for the smooth and rough cylinder ($H_s = 0.43$ m, $T_p = 2.8$ s). (a) Horizontal force; (b) Vertical force.

Because of the relevant scattering of the force peaks due to random behaviour of the wind-generated waves, we averaged the peaks within intervals of KC wide 0.5. The mentioned behaviour, also noticed for the hydrodynamic force coefficients, was particularly observed in the case of field experiments (e.g., [26]). The positive and negative peaks of the horizontal and vertical forces both for the smooth and rough cylinder are shown in Fig. 6.2. Each symbol represents the average value of F_{Hmax} (or F_{Vmax}) recorded during a sea state whose KC falls in the considered interval. The force peaks are normalized by the absolute maximum found in all considered sea states (i.e., $F_{Hmax}{}^*$ and $F_{Vmax}{}^*$). Moreover, vertical error bars at each data point were also added to highlight the scattering of the maximum value of the forces due to the uncertainties given by the accuracy of the pressure sensor measurements (see Section 4.7). Specifically, this uncertainty is equal to ±7%. Owing to the roughness effect, a general increase by 15% and 6% can be shown for the positive peaks of horizontal and vertical forces, respectively. Moreover, the presence of the roughness leads

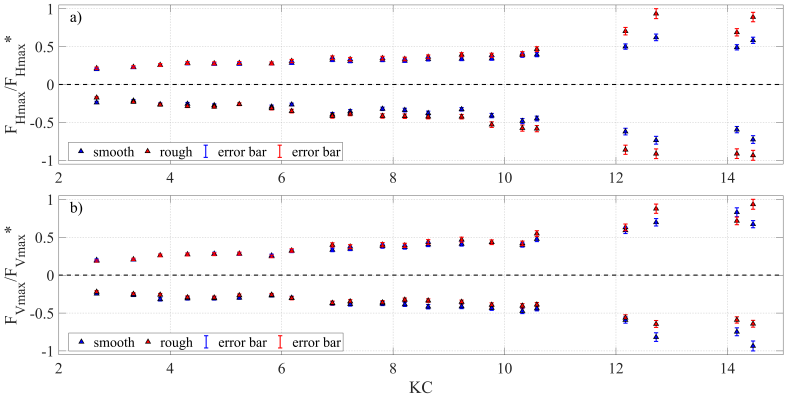

Figure 6.2: Positive and negative force peaks vs. KC for the smooth and rough cylinder. (a) Horizontal force; (b) Vertical force.

that the negative peaks increase by 17% for the horizontal force and reduce by 11% for the vertical one. In general, all types of peaks highlight an overall linear trend proportionally to KC both for the smooth and rough cases. The presence of the roughness is amplified the larger KC is. As better underlined in Section 6.3 on the analysis of the force components, this behaviour can be explained by the rise of the drag (or lift) force component in comparison with the inertia one when KC increases (e.g., [73]).

6.2 Hydrodynamic coefficients

Using the Morison and transverse semi-empirical formulas, the estimation in the time domain of the horizontal and vertical forces on a cylinder can be obtained. These methods start from the knowledge of the hydrodynamic coefficients, which in turn depend on the experimental kinematic field at the cylinder in undisturbed conditions, the measured wave forces and

the dimensions of the cylinder. The methods illustrated in literature evaluate the hydrodynamic coefficients starting from tests carried out in wave flumes or laboratory tanks (e.g., [74], [75], [37]). Here, we are dealing with field experiments characterized by short-crested waves. Therefore, the hydrodynamic coefficients are obtained following the approach introduced by Boccotti [65]. As stated by the author, this method is suitable for field tests and based on the linear theory of wind-generated waves. It allows the coefficients to be obtained by imposing that: (i) the estimated force and the measured one have the same variance and (ii) the ratio between the weight of the drag force and the weight of the inertia one is the same both between measured forces or between the calculated ones. The values of the hydrodynamic coefficients are then obtained as

$$\begin{cases} C_D = \left(\dfrac{\langle f_{HI}^2(t) \rangle \langle F_H(t) f_D(t) \rangle}{\langle f_D^2(t) \rangle \langle F_H(t) f_{HI}(t) \rangle} \right) C_{MH}, \\ C_{MH} = \sqrt{\dfrac{\langle F_H(t)^2 \rangle}{\langle f_{HI}^2(t) \rangle + \left(\dfrac{\langle f_{HI}^2(t) \rangle \langle F_H(t) f_D(t) \rangle}{\langle f_D^2(t) \rangle \langle F_H(t) f_{HI}(t) \rangle} \right)^2 \langle f_D^2(t) \rangle}}, \end{cases} \tag{6.1}$$

with $f_D(t)$ and $f_{HI}(t)$ calculated by Eqs. 4.37 and 4.38.

The above methodology is also applied for obtaining the hydrodynamic coefficients for the vertical force

$$\begin{cases} C_L = \left(\dfrac{\langle f_{VI}^2(t) \rangle \langle F_V(t) f_L(t) \rangle}{\langle f_L^2(t) \rangle \langle F_V(t) f_{VI}(t) \rangle} \right) C_{MV}, \\ C_{MV} = \sqrt{\dfrac{\langle F_V(t)^2 \rangle}{\langle f_{VI}^2(t) \rangle + \left(\dfrac{\langle f_{VI}^2(t) \rangle \langle F_V(t) f_L(t) \rangle}{\langle f_L^2(t) \rangle \langle F_V(t) f_{VI}(t) \rangle} \right)^2 \langle f_L^2(t) \rangle}}, \end{cases} \tag{6.2}$$

where $f_L(t)$ and $f_{VI}(t)$ are determined as

$$f_L(t) = \frac{1}{2} \rho D \sqrt{v_y(t)^2 + v_z(t)^2} v_z(t), \tag{6.3}$$

$$f_{VI}(t) = \frac{\pi}{4} D^2 \rho a_z(t). \tag{6.4}$$

The values of C_D, C_{MH}, C_L and C_{MV} are plotted vs. KC in Fig. 6.3. As carried out for the force peaks, vertical error bars were added to this plot to quantify the uncertainties derived from the accuracy of the simultaneous measurements of pressure transducers and ultrasonic sensors through the Monte Carlo method (e.g., [76]). This methodology is here preferred over traditional uncertainty propagation because it does not rely on linear approximations and can handle complex, nonlinear relationships between input parameters and outputs. To implement the Monte Carlo method for assessing uncertainty in the hydrodynamic coefficients, a systematic approach is followed. Firstly, the probability distributions of the forces influencing the structure were defined for the selected 107 sea states. Next, random samples were generated for each measured force using appropriate random number generation techniques, that conform to the defined probability distribution with the standard uncertainty calculated in Section 4.7. Each set of simulated force values represents a potential scenario of forces acting on the involved cylinders. For each scenario, the developed computational model was employed to calculate the corresponding hydrodynamic coefficients from Eqs. 6.1 and 6.2. The simulation and computation process was repeated several times, for each test, to generate a substantial dataset of hydrodynamic coefficients. This dataset captures the range of possible outcomes considering the variability in the forces and their impact on the coefficients, and it is used to determine the probability distribution of the hydrodynamic coefficients. Measurements such as the mean, standard deviation, and confidence intervals are calculated to quantify the central tendency and spread of the coefficients across the sampled scenarios. To determine the uncertainty associated with the hydrodynamic

coefficients (U_{CD}, U_{CMH}, U_{CL} and U_{CMV}), we then obtain

$$U_{CD} = \pm\sigma_{CD} = \pm 25\%, \tag{6.5}$$

$$U_{CMH} = \pm\sigma_{CMH} = \pm 17\%, \tag{6.6}$$

$$U_{CL} = \pm\sigma_{CL} = \pm 35\%, \tag{6.7}$$

$$U_{CMV} = \pm\sigma_{CMV} = \pm 3\%. \tag{6.8}$$

Concerning the horizontal force coefficients (Figs. 6.3a and 6.3b), it can be observed that C_D increases proportionally to KC for both cylinders until about $KC = 6$, followed by an overall constant tendency, while C_{MH} shows a small decrease for low KC and a successive small increase for high KC. Paying attention to the vertical force coefficients (Figs. 6.3c and 6.3d), C_L and C_{MV} highlight an overall increasing trend in the considered range of KC. This behaviour is more pronounced for C_{MV}. Apart from the case of C_D associated to low KC, it is worth noting that all coefficients for the rough cylinder show higher values if compared to the smooth case. Indeed, C_D exhibits a mean increase of about 10%, C_{MH} of about 9%, C_L of about 2% and C_{MV} of about 5%. For the considered range of KC, the coefficients obtained are quite in agreement with those obtained by Boccotti [65] and Marty et al. [34] for the case of horizontal smooth cylinder. The roughness effect on the drag and lift coefficients are in between of what obtained by Zeinoddini et al. [32] for coverage ratios of 33% and 66% using a vertical cylinder.

6.3 Application of semi-empirical equations

The features of the different components of the estimated hydrodynamic forces (i.e., drag, horizontal inertia, lift and vertical inertia) are displayed along a time interval of 50 s. To

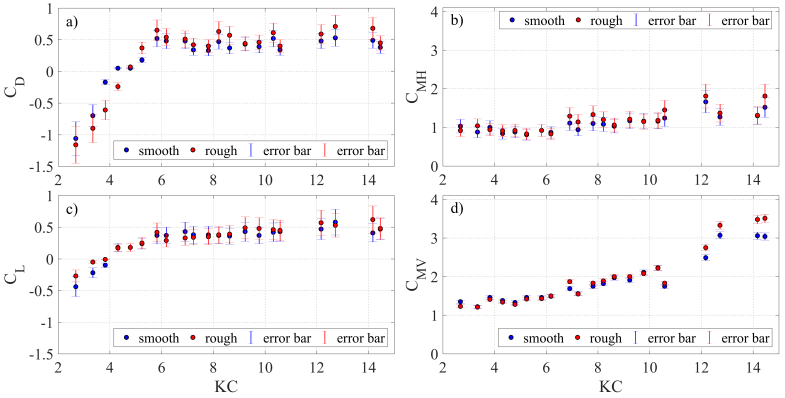

Figure 6.3: Hydrodynamic force coefficients vs. KC. (a) C_D; (b) C_{MH}; (c) C_L; (d) C_{MV}.

analyze the weight of the involved force components, two different tests are chosen, one considering a low KC (Fig. 6.4), and one a high KC (Fig. 6.5). Specifically, the first case is characterized by $H_s = 0.27$ m, $T_p = 2.4$ s and $KC = 4.10$, while the second, by $H_s = 0.68$ m, $T_p = 3.5$ s and $KC = 14.17$. The tests are normalized by the maximum force which, in these cases, is the inertia component. It can be highlighted that, for low KC tests, the so-called inertia-dominated regime occurs. This regime is due to the symmetry into the vortex generation induced by the interaction between the wave motion and the cylinder [17]. When KC increases, the contribution of the drag (Figs. 6.5a and 6.5b) and lift (Figs. 6.5c and 6.5d) force components increases since the symmetry condition of the vortices disappears (e.g., [19], [13]). It can be also observed that inertia force components are generally backward shifted with respect to the drag and lift force components. This is evident both for the smooth cylinder and for the rough one. This feature is due to the fact that the inertia force components are proportional to the acceleration field, while the drag and lift

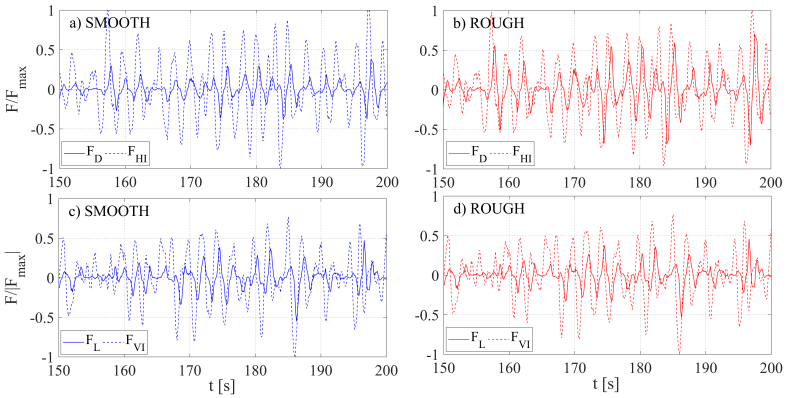

Figure 6.4: Time variation of horizontal and vertical force components calculated by semi-empirical equations ($H_s = 0.27$ m, $T_p = 2.4$ s, $KC = 4.10$). (a) Drag and horizontal inertia - smooth cylinder; (b) drag and horizontal inertia - rough cylinder; (c) lift and vertical inertia - smooth cylinder; (d) lift and vertical inertia - rough cylinder.

force components to the velocity field. Indeed, these kinematic quantities are 90° out of phase between them.

Considering all the 107 tests, the peak values of the force components are plotted in Fig. 6.6, averaging on intervals of KC equal to 0.5. The force components are normalized by the maximum value of the peak force among all tests. It can be generally noticed that the inertia components are prevalent on the drag and lift components, being the range of considered KC typical of the inertia-dominated regime (e.g., [13], [73]). A larger difference between the force peaks can be particularly observed by comparing the lift and vertical inertia components between them. This difference is emphasized for low KC.

To test the performance of the Morison and transverse schemes, we computed the Percentage Error (PE) between the peaks of the measured forces (F_{max}) and those calculated

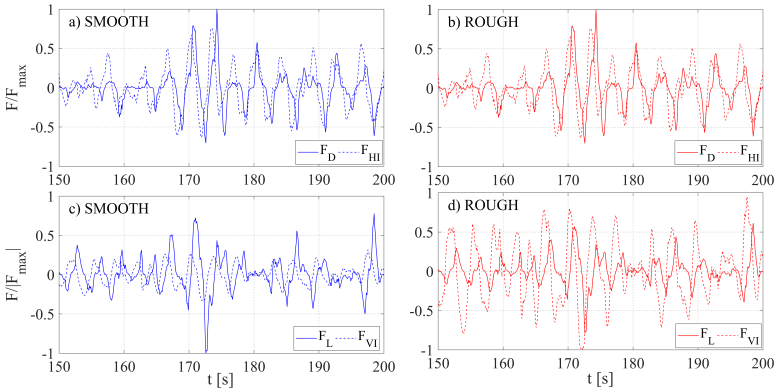

Figure 6.5: Time variation of horizontal and vertical force components calculated by semi-empirical equations ($H_s = 0.68$ m, $T_p = 3.5$ s, $KC = 14.17$). (a) Drag and horizontal inertia - smooth cylinder; (b) Drag and horizontal inertia - rough cylinder; (c) Lift and vertical inertia - smooth cylinder; (d) Lift and vertical inertia - rough cylinder.

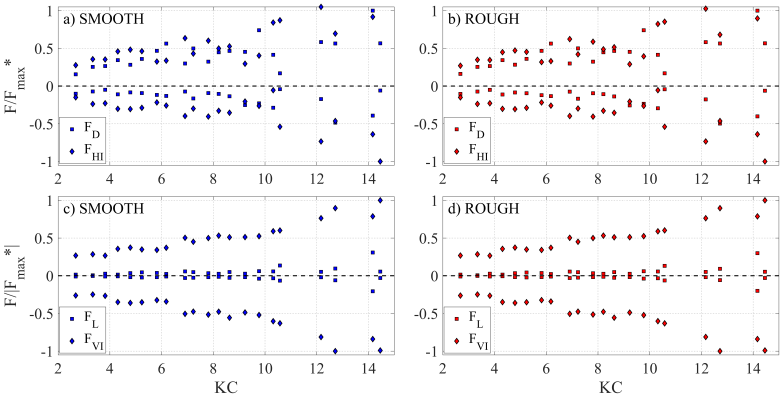

Figure 6.6: Positive and negative peaks of force components vs. KC. (a) Drag and horizontal inertia - smooth cylinder; (b) Drag and horizontal inertia - rough cylinder; (c) Lift and vertical inertia - smooth cylinder; (d) Lift and vertical inertia - rough cylinder.

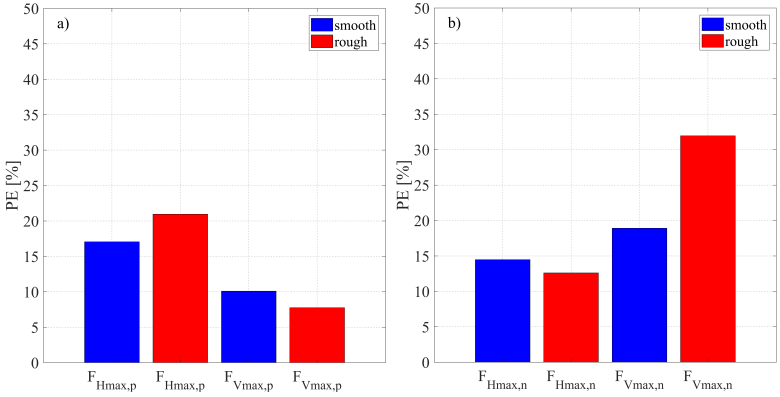

Figure 6.7: Percentage Errors (PE) between the measured and calculated horizontal and vertical force peaks. (a) Positive peaks; (b) Negative peaks.

by the models ($F_{max,m}$) as

$$PE = \left| \frac{F_{max} - F_{max,m}}{F_{max}} \right| 100. \tag{6.9}$$

Looking at Figure 6.7, some considerations can be done. The errors calculated for the positive peaks (Fig. 6.7a) are of about 17% and 20% for the horizontal force acting on the smooth and rough cylinder, respectively, and about 10% and 7% for the vertical one, respectively. Instead, the errors in the negative peaks (Fig. 6.7b) are equal to 14% and 13% for the horizontal force at the smooth and rough cylinder, respectively, and 18% and 32% in the vertical case, respectively. Generally, it can be noticed that the semi-analytical models work better in smooth condition than in the rough one, especially for the negative peak of the vertical force. Indeed, the Morison and transverse schemes do not consider as input the presence of roughness which undoubtedly modifies the flow field near the cylinder.

The effectiveness of the Morison and transverse semi-empirical models for short-crested waves was also tested in the frequency domain. This analysis was carried out by comparing the measured spectra of the horizontal and vertical forces with the calculated ones. The normalized spectra are shown in Fig. 6.8. The frequencies in abscissas are dimensionless by dividing them for the peak frequency f_p. The chosen test was characterized by $H_s = 0.43$ m and $T_p = 2.8$ s. As highlighted in Figs. 6.8a and 6.8b, it can be noticed that the spectrum of the horizontal force obtained experimentally and that obtained by the Morison scheme are quite similar both for the smooth and rough case. Small discrepancies can be observed for the magnitude of the peak of the spectrum and for some energy contents close to the peak. Regarding the comparison of the spectrum of the vertical forces for the smooth and rough case (Figs. 6.8c and 6.8d), a small underestimation of the calculated spectrum on the peak and some energy contents in comparison with the measured one can be observed in the case of smooth cylinder. For the rough cylinder, it is instead evident an overall overestimation of the calculated spectrum, particularly for the energy contents before and after the peak. To better quantify the differences between the measured and calculated force spectra, the narrow bandedness parameter ψ^*, introduced by [13] and described in Section 4.1, was determined for all cases of this example test. Fig. 6.9 shows the values of ψ^* deduced from the spectra of the horizontal and vertical forces for the case of smooth and rough cylinder. The parameter ψ^* oscillates between 0.49 and 0.77. Regarding the measured and calculated spectra of horizontal forces of the smooth and rough cylinder, the differences on ψ^* are quite low and equal to 3.9% and 6.9%, respectively. Paying attention to the measured and calculated spectra of vertical forces of the smooth and rough cylinder, the differences on ψ^* are larger than the case of the horizontal forces and equal to 26.5% and 44.9%, respectively,

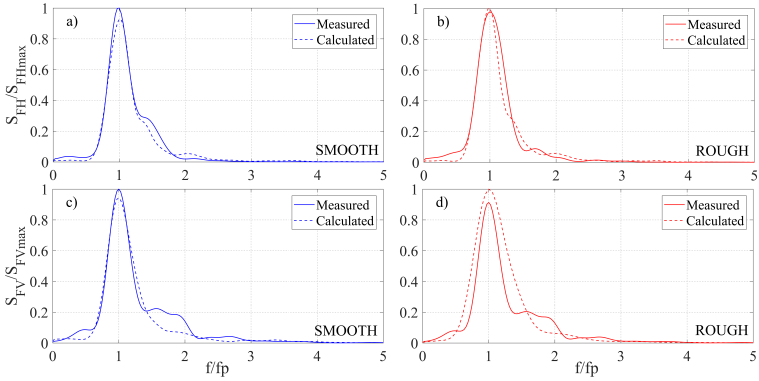

Figure 6.8: Comparison between measured and calculated force spectra ($H_s = 0.43$ m, $T_p = 2.8$ s). (a) horizontal force - smooth cylinder; (b) horizontal force - rough cylinder; (c) vertical force - smooth cylinder; (d) vertical force - rough cylinder.

highlighting some limitations of the transverse scheme to well model the shape of the measured spectrum, particularly for the rough case.

6.4 Probability of exceedance of the force peaks

The last analysis concerns the study of the probability of exceedance of the measured force peaks in comparison with those calculated by the semi-empirical models. As stressed by Boccotti [65], this type of analysis is useful for design purposes, and it can be also adopted to check the effectiveness of Morison and transverse equations for wind-generated waves. Starting from 107 considered tests, both for the smooth and the rough cylinder, it is possible to define the normalized random process of the calculated and measured forces as

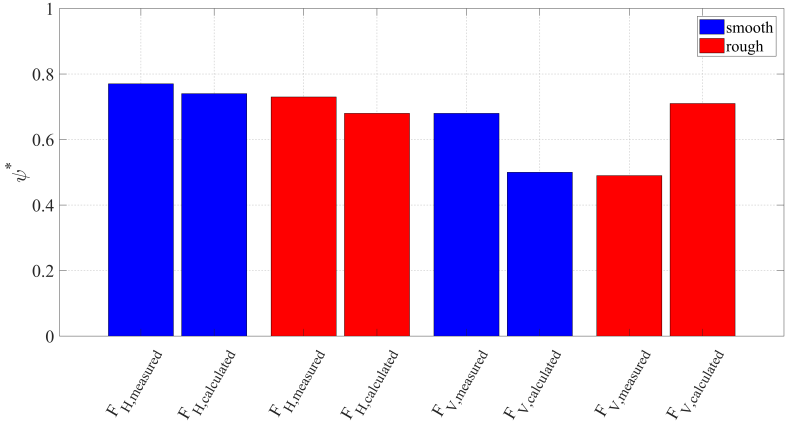

Figure 6.9: Narrow bandedness parameter ψ^* of the measured and calculated force spectra ($H_s = 0.43$ m, $T_p = 2.8$ s).

$$F_H^*(t) = \frac{F_H(t)}{\sqrt{\langle F_H^2(t)\rangle}}, \tag{6.10}$$

$$F_V^*(t) = \frac{F_V(t)}{\sqrt{\langle F_V^2(t)\rangle}}, \tag{6.11}$$

$$F_{Hm}^*(t) = \frac{F_{Hm}(t)}{\sqrt{\langle F_{Hm}^2(t)\rangle}}, \tag{6.12}$$

$$F_{Vm}^*(t) = \frac{F_{Vm}(t)}{\sqrt{\langle F_{Vm}^2(t)\rangle}}, \tag{6.13}$$

where F_H^*, F_V^*, F_{Hm}^* and F_{Vm}^* are referred to the horizontal measured force, vertical measured force, horizontal calculated force and vertical calculated force, respectively. For each test, the largest peak, both positive and negative, was selected. For a given threshold β, as done by Boccotti [65], the comparison can be performed by introducing the probability of exceedance

of the peaks of a normalized Gaussian random force with a narrow band spectrum as

$$P(peak > \beta) = exp\left(-\frac{\beta^2}{2}\right). \tag{6.14}$$

In Figs. 6.10, 6.11, 6.12 and 6.13, the probability of exceedance of the positive peaks and negative peaks for the horizontal and vertical forces are shown, both for the smooth cylinder and for the rough one. Specifically, the theoretical probability of exceedance was determined by fixing values of β so that P ranges between about 10^{-4} and 10^{-1}, considering that 107 tests were adopted. Then, the normalized random process of the measured and calculated forces (see Eqs. 6.10, 6.11, 6.12 and 6.13) are inserted into Eq. 6.14 in the place of β to determine P. The distribution of the peaks of the calculated force process is quite close to the distribution of the measured force process, particularly for high values of P. Considering a threshold β with a probability of 10^{-3} (i.e., a serious case by an engineering viewpoint), the difference on β between experimental and calculated positive peaks of the horizontal force process is close to 0.3% for the case of smooth cylinder (Fig. 6.10a) and about 1% for the case of rough cylinder (Fig. 6.10b). For the same considered probability, the difference on β between experimental and calculated positive peaks of the vertical force process is approximately 0.2% for the case of smooth cylinder (Fig. 6.11a) and about 2% for the case of rough cylinder (Fig. 6.11b). Regarding the negative peaks, the difference on β between measured and calculated horizontal force process is less than 0.5% for the case of smooth cylinder (Fig. 6.12a) and almost the same for the case of rough cylinder (Fig. 6.12b), while the difference on β between measured and calculated vertical force process is less than 1% for the case of smooth cylinder (Fig. 6.13a) and about 1.5% for the case of rough cylinder (Fig. 6.13b). For this kind of analysis, it is

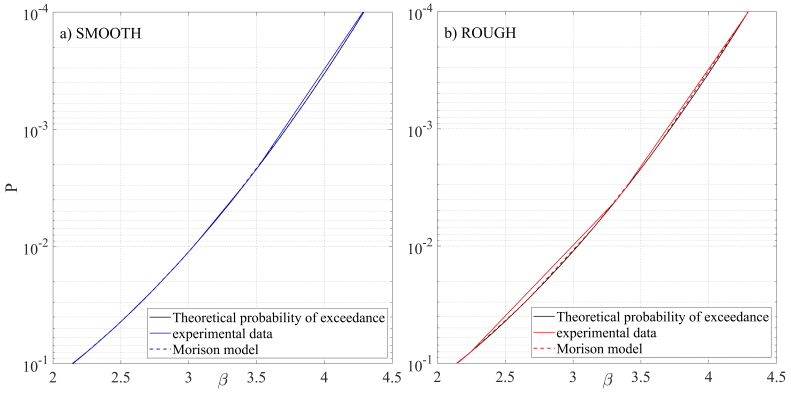

Figure 6.10: Probability of exceedance of the positive peaks of the horizontal force. (a) smooth cylinder, (b) rough cylinder.

worth noting that the Morison and transverse schemes lead to a slight underestimation if compared to the measured data in all the cases.

6.5 Results of the application of neural networks

The results obtained by the application of the considered neural networks are here illustrated. The first application is related to the prediction of the 95^{th} percentile of the horizontal and vertical forces induced by the waves on the horizontal circular smooth and rough cylinder. As said in Chapter 5.1.1, a feedforward neural network with 2 hidden layer each of 32 and 16 fully connected neurons is used. A first result can be shown in Fig. 6.14, in which the performance of the network in predicting the 95^{th} percentile values is plotted calculating the Mean Absolute Error (MAE) and the Mean Squared Error (MSE) for the test database. MAE is about 0.84, indicating that, on average, the absolute difference between the predicted

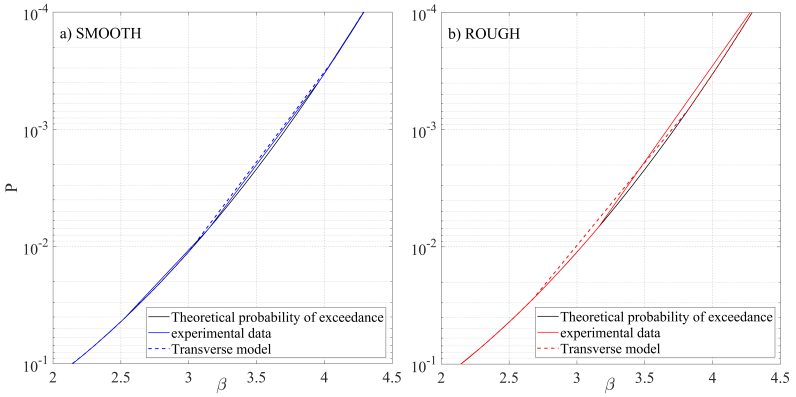

Figure 6.11: Probability of exceedance of the positive peaks of the vertical force. (a) smooth cylinder, (b) rough cylinder.

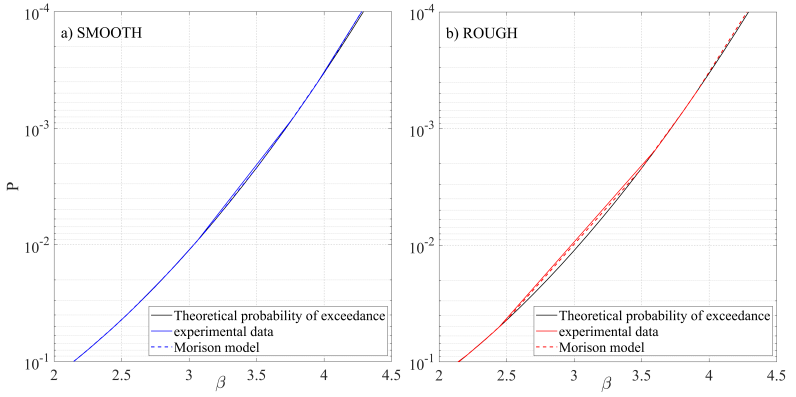

Figure 6.12: Probability of exceedance of the negative peaks of the horizontal force. (a) smooth cylinder, (b) rough cylinder.

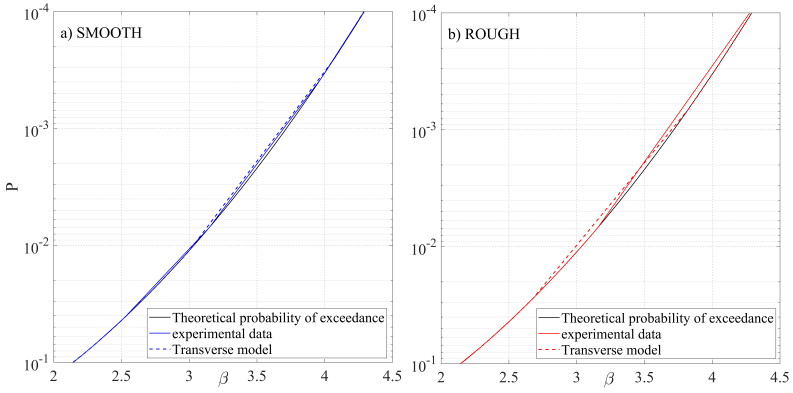

Figure 6.13: Probability of exceedance of the negative peaks of the vertical force. (a) smooth cylinder, (b) rough cylinder.

values and the actual ones is about 0.84 units. Since the predicted values have a wide range, the result obtained from the MAE calculation can be considered a good estimator of the goodness of the constructed model. MAE is straightforward to interpret, since it represents the average magnitude of the errors in the same unit as the target variable, without considering their direction (positive or negative). The Mean Squared Error (MSE) of about 1.29 provides the average of the squared differences between predicted and actual values. Since errors are squared before averaging, MSE gives more weight to larger errors, which means that it is more sensitive to outliers compared to MAE. Since they are relatively close, the errors are reasonably consistent without extreme outliers significantly affecting the MSE. As shown in Fig. 6.15, the MAE and MSE values on the validation dataset are essential for assessing how well the model performs on new and unseen data. This reflects the model's ability to generalize rather than simply memorize the training data. Looking at the metrics of the validation database, we can observe that the values of MAE and MSE are

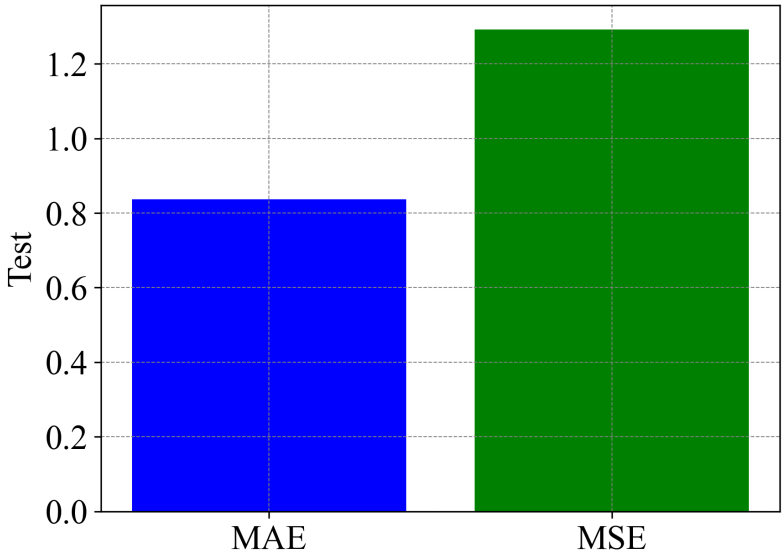

Figure 6.14: MAE and MSE of the test database (first approach).

relatively very close to the one of the test. Similar MAE and MSE values between the validation and test datasets suggest that the model generalizes well to unseen data. This means that the model has learned the underlying patterns in the data without overfitting to the training set.

A good estimation in how well the neural network model performs in predicting the experimental features of the 95^{th} percentile of the horizontal and vertical forces on the horizontal smooth and rough cylinder can be also made by calculating the coefficient of determination R^2. It is generally evaluated as

$$R^2 = 1 - \frac{\sum_{i=1}^{n}(y_i - \hat{y}_i)^2}{\sum_{i=1}^{n}(y_i - \bar{y})^2}, \tag{6.15}$$

where y_i are the experimental values, $\hat{y}_i$ are the values predicted by the neural network, and $\bar{y}$ is the mean of the exper-

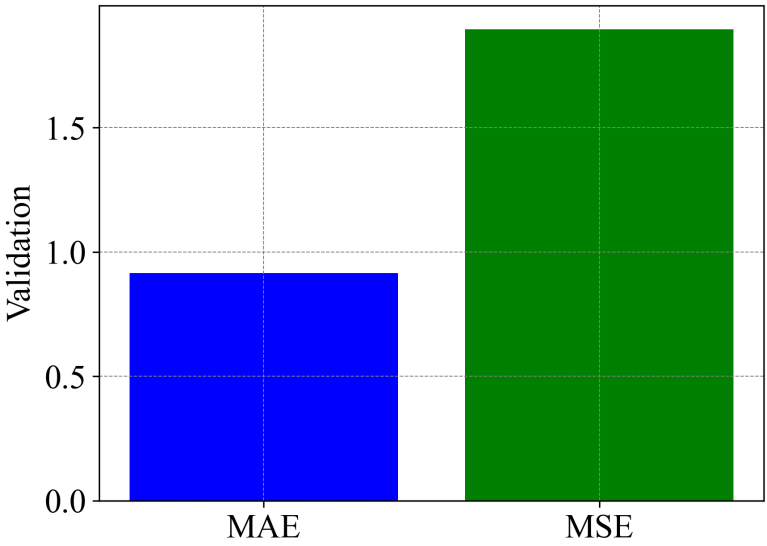

Figure 6.15: MAE and MSE of the validation database (first approach).

imental values.

The obtained coefficients of determination are shown in Fig. 6.16, in which it can be noted that the network works better in predicting the 95^{th} percentiles of the horizontal forces for smooth $95^{th}{F_H}^s$ and rough cylinders $95^{th}{F_H}^r$ in comparison to the ones for the vertical forces on the smooth $95^{th}{F_V}^s$ and rough $95^{th}{F_V}^r$ cylinders. In fact, the coefficients of determination for these cases are equal to 0.90 and 0.89, respectively. For the vertical forces, the values are 0.84 and 0.80 for the smooth and the rough cylinder, respectively. Looking at the scatter plot in Fig. 6.17, it is observable a good result in terms of prediction of the neural network model. Indeed, all the points are in between the 15% deviation bar and just some values gave errors greater than 30%. It is worth noting a good agreement between the experimental values and the predicted ones for the case of smooth and rough horizontal forces (Figs. 6.17a and b) and for the vertical smooth one (Fig. 6.17c). A bit of underestimation and a more scattering trend is notable in Fig. 6.17d with reference to the vertical forces on the rough cylinder.

Concerning the results of the second neural network, this modeling is able to predict the standard deviation of the experimental horizontal and vertical forces acting on the smooth and rough horizontal cylinder. As for this case, the neural network was a feedforward-type with 2 hidden layers with 32 and 16 layers, respectively. In Fig. 6.18 the mean absolute error (MAE) and the mean squared error (MSE) computed for the training dataset are reported. Also in this case, the two errors are relatively close. MAE is equal to 0.36 and MSE is equal to 0.22. Comparing to the results of the first artificial neural network, the above lower values indicate a better performance of this second one in predicting the standard deviation of the forces. The conclusion is the same also by looking at the results of the MAE and MSE between the test (Fig. 6.18) and

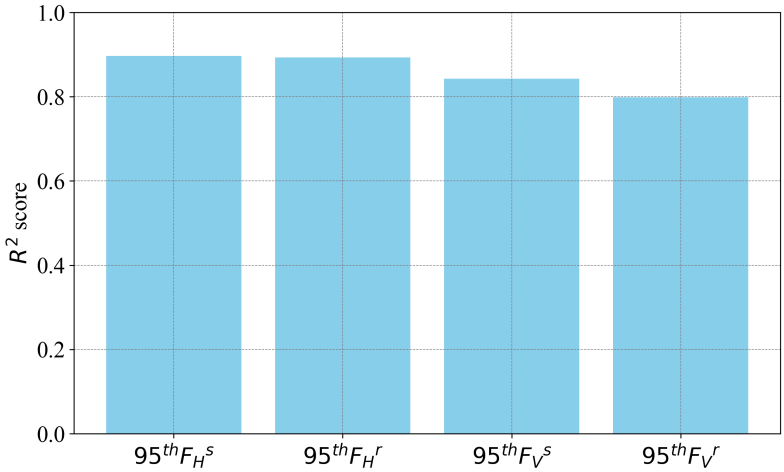

Figure 6.16: Coefficients of determination obtained applying the first FNN.

the validation (Fig. 6.19) datasets.

The coefficients of determination, obtained by comparing the measured values with the predicted ones by the second neural network in terms of standard deviation of the forces, are shown in Fig. 6.20. Also in this case, it is shown that the second FNN works well in predicting the standard deviation of the horizontal forces, with values of R^2 of 0.89 for both the smooth (σ_{FH_s}) and rough cylinder (σ_{FH_r}). These values are lower for the vertical forces on the smooth (σ_{FV_s}) and on the rough (σ_{FV_r}) cylinders. In fact, the value of R^2 is 0.84 and 0.80 for the smooth and the rough horizontal cylinder, respectively. Similar findings can be done by looking at the scatter plots in Fig. 6.20. All the points are in between the 15% deviation band and just some values exceeds the 30% band. The better results in terms of agreement between the measured values and the predicted ones are for the standard deviation of the horizontal forces both for the smooth and the rough cases (Fig.

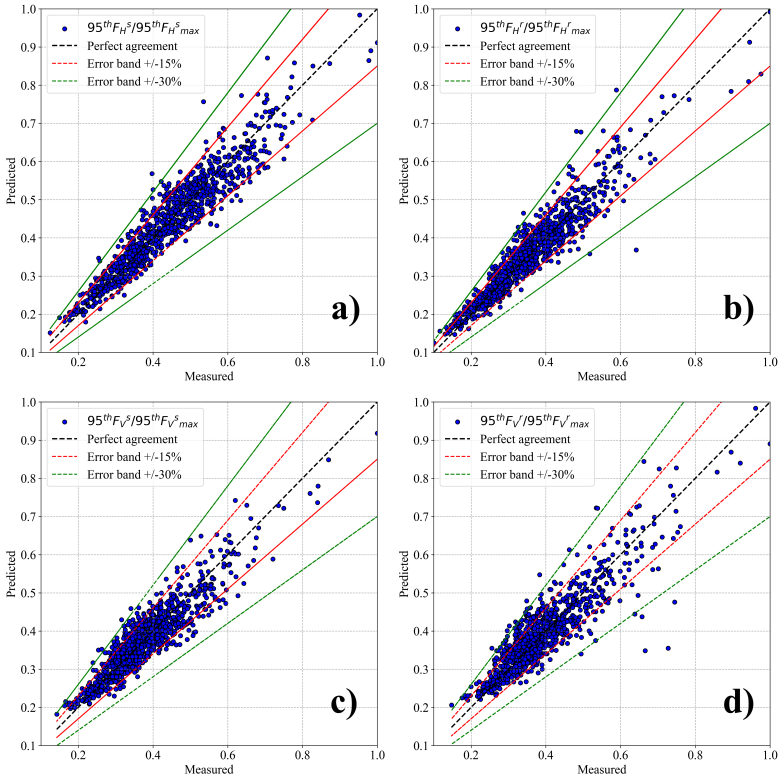

Figure 6.17: Scatter plots of the measured values vs. the predicted ones by the first neural network. a) horizontal force (smooth cylinder), b) horizontal force (rough cylinder), c) vertical force (smooth cylinder), b) vertical force (rough cylinder)

.

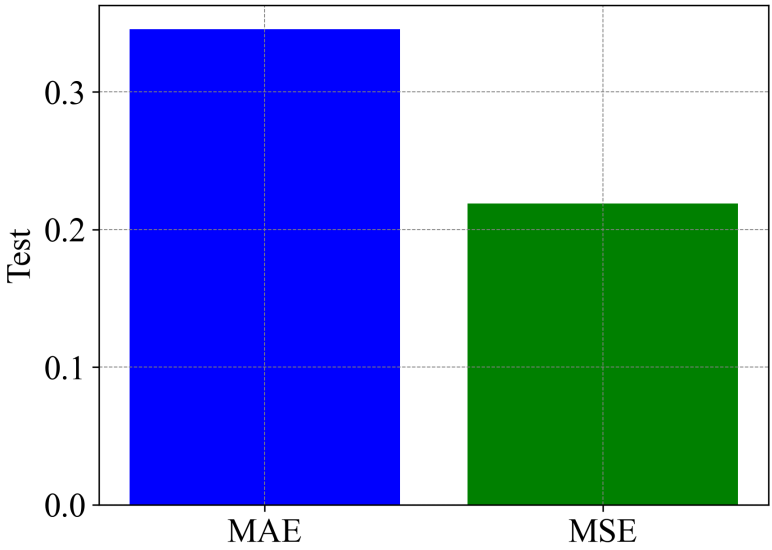

Figure 6.18: MAE and MSE of the test database (second approach).

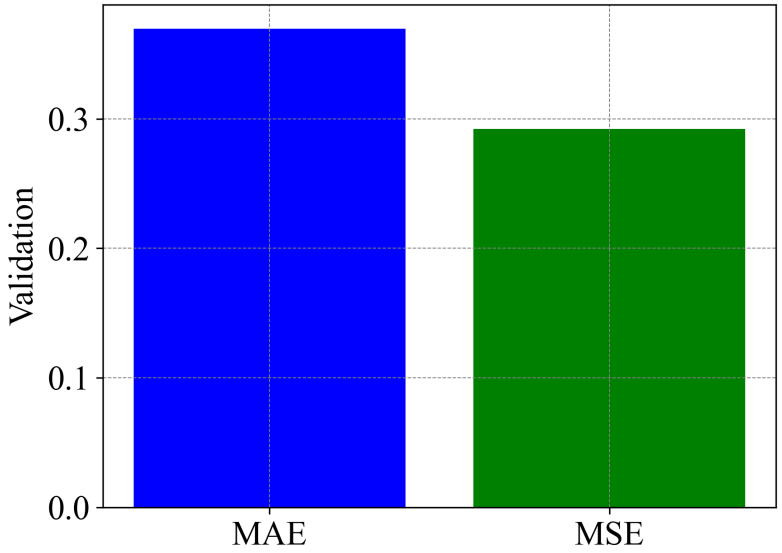

Figure 6.19: MAE and MSE of the validation database (second approach).

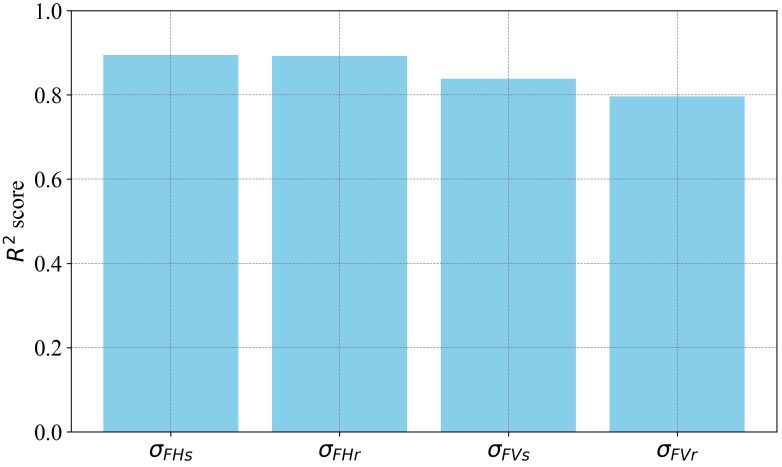

Figure 6.20: Coefficients of determination obtained applying the second FNN.

6.21a and b). Slightly lower, but generally acceptable, are the performance for the case of vertical forces at the smooth cylinder (Fig. 6.21c) and a little bit more scattering for the rough one (Fig. 6.21d).

The last analysis concerned the reconstruction of the probability density function of the force process, from the values of standard deviation obtained from the previous neural network. Since we have predicted the standard deviations, the PDF function can be reconstructed by means of Eq. 5.2. For two representative sea states with $H_s = 0.18$ m and $T_p = 1.8$ and $H_s = 0.69$ m and $T_p = 3.59$, Figs. 6.22 and 6.23 show the results of the reconstruction of the PDF function with the FNN compared to the measured one for the horizontal and vertical forces acting on the smooth and rough cylinder. It can be seen that the predictions made by the neural network are quite good, since the PDF curves for the horizontal and vertical forces (both for the smooth and the rough cylinder) are quite close to those deduced from the measurements. The good agreement between the models and the experimental result is also shown in Fig. 6.24 by comparing, for the two test cases, the values of the 95^{th} percentile of the forces directly predicted by the first neural network against the ones measured as well as the same percentiles extracted by the PDF evaluated from the second neural network also against the measured results. This analysis was done by computing a Percentage Error (PE) between measured and simulated percentiles, taking the mean value obtained by the two cases. It can be highlighted that, for both cases, the errors are quite low. More in detail, the errors computed by predicting the 95^{th} percentile for the test cases are 3.71% and 3.19% (Fig. 6.24a) using the first neural network ($95^{th}F_{H,1NN}$) and the second one ($95^{th}F_{H,2NN}$) for the horizontal force on the smooth cylinder, respectively, 2.23% and 3.67% for the horizontal force on the rough cylinder (Fig. 6.24b), 2.81% and 3.34% (Fig. 6.24c) for the vertical

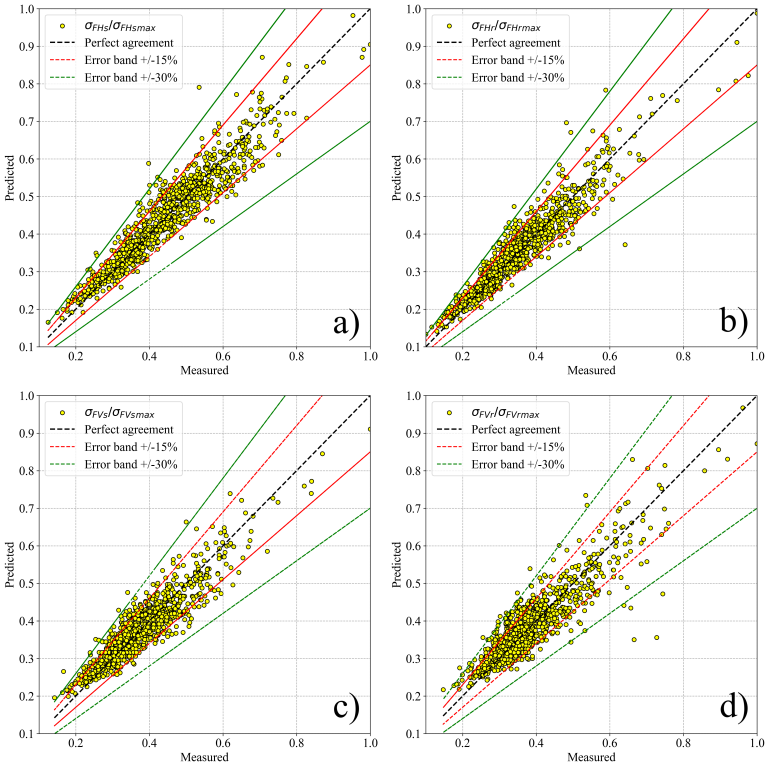

Figure 6.21: Scatter plots of the measured values vs the predicted ones for the second neural network approach. a) horizontal force (smooth cylinder), b) horizontal force (rough cylinder), c) vertical force (smooth cylinder), b) vertical force (rough cylinder)

.

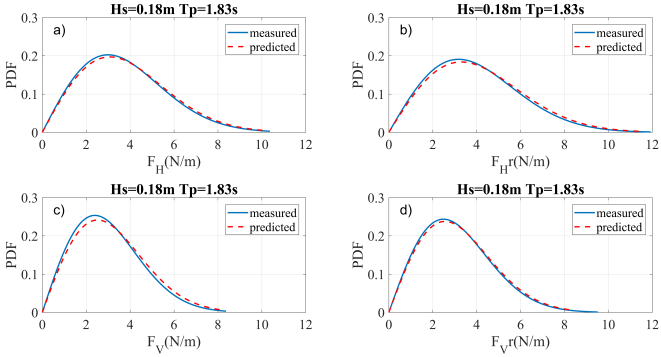

Figure 6.22: Predicted PDF functions by ANN vs. measured ones for a test with $H_s = 0.18$ m and $T_p = 1.8$ s. a) horizontal force (smooth cylinder), b) horizontal force (rough cylinder), c) vertical force (smooth cylinder), b) vertical force (rough cylinder).

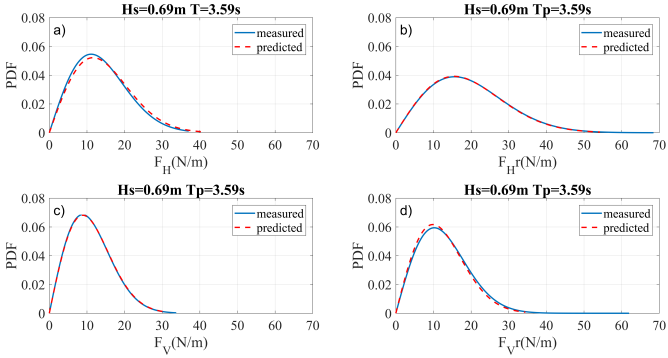

Figure 6.23: Predicted PDF functions by ANN vs. measured ones for a test with $H_s = 0.69$ m and $T_p = 3.59$ s. a) horizontal force (smooth cylinder), b) horizontal force (rough cylinder), c) vertical force (smooth cylinder), b) vertical force (rough cylinder).

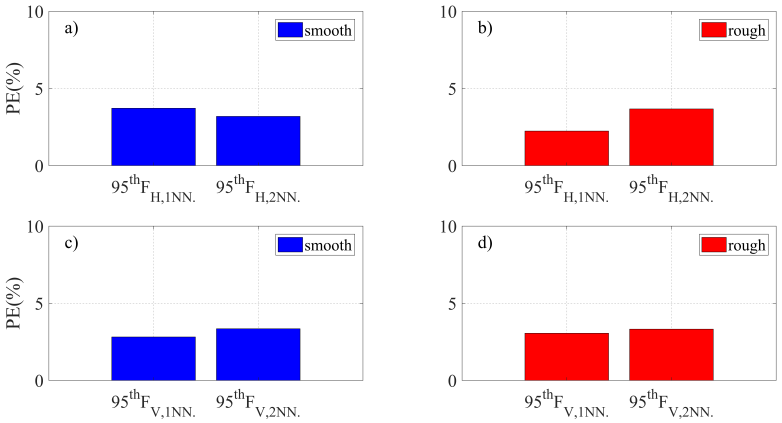

Figure 6.24: Mean values of the Percentage Errors PE calculated by comparing the 95^{th} percentile extracted by the first neural network and the second one (for the two test cases). a) horizontal force (smooth cylinder), b) horizontal force (rough cylinder), c) vertical force (smooth cylinder), b) vertical force (rough cylinder).

force on the smooth cylinder, and 3.06 % and 3.33% (Fig. 6.24d) for the vertical force on the rough cylinder ($95^{th}F_{V,1NN}$ and $95^{th}F_{V,2NN}$). Both methods show a good performance to quantify this percentile of the forces. Slightly better results can be pointed out when extracting these values by reconstructing the PDF with the second neural network.

CHAPTER 7

Conclusions and ongoing activities

In this thesis, field tests to investigate the features of the hydrodynamics forces on a horizontal circular cylinder covered by printed barnacles have been performed. The tests have been carried out in the reserved portion of sea of the Marine Energy Laboratory of the University of Reggio Calabria adopting laboratory techniques. The set-up was composed by two submerged horizontal cylinders, one smooth and one covered with a barnacles-type roughness, both placed at 0.95 m below the SWL and aligned along the same longitudinal axis. Adopting two ultrasonic probes, arranged above the SWL, the time series of surface elevations, wave directions and wave kinematics have been evaluated. Thanks to a battery of 8 pressure transducers, placed in the middle section of each cylinder, the time series of horizontal and vertical forces have been deduced. Field tests, each lasting 5 min and characterized by only wind-generated waves, has been considered. The experimental results revealed a general increase of the loads on the rough cylinder if compared to the smooth one. The effect of the roughness leads to a mean rise of 15% and 6% for the positive peaks of the horizontal and vertical forces, respectively, while an increase

of 17% and a reduction of 11% has been found for the negative peaks of the horizontal and vertical force, respectively. The hydrodynamic force coefficients have been calibrated in the Morison and transverse semi-empirical models for short-crested waves. Owing to the roughness around the cylinder, a general mean increase of the drag coefficient by 10%, of the inertia coefficient by 9%, of the lift coefficient by 2% and of the vertical inertia coefficient by 5% in comparison with the smooth one has been found. The spectral analysis of the wave loads as well as the analysis of the probability of exceedance of the force peaks led us to conclude that the Morison and transverse schemes for short-crested waves can be used, in the case of field tests with the involved range of KC, for the evaluation of the hydrodynamic forces on horizontal cylinders. The application of the above simplified force schemes gives good results for the smooth cylinder, while some acceptable discrepancies have been observed for the rough one.

Two feedforward neural networks were implemented in order to evaluate some features of the wave-induced forces on the involved two cylinders. The networks were composed by two fully connected hidden layers a first one with 32 neurons and a second one with 16 neurons. In particular, a first neural network was used to calculate the 95^{th} percentile of the wave forces. The second one was used to reconstruct, knowing the standard deviation of the forces, the probability density function. The comparisons with the experimental results have shown a good performances of both feedforward neural networks, the errors obtained by comparing the percentile results extraced by the first neural network and the percentile calculated by the PDF reconostructed by the second neural networks with the experimental values are quite good in both cases with low errors.

Further field experiments will be carried out to investigate the hydrodynamic loads induced by wind-generated waves on

cylinders covered by a higher coverage ratio of the barnacles around the cylinder with respect to the current one and using soft fouling such as kelps. Also, neural networks will be trained with larger and more generalized datasets with respect to the current one. Different neural network models (e.g., LSTM) will be finally applied to try to predict the time series of the forces acting on the cylinders.

APPENDIX A

Symbology

	SYMBOLOGY
1	$95^{th} F_H^r$ = 95th percentile of the horizontal force on the rough cylinder
2	$95^{th} F_H^s$ = 95th percentile of the horizontal force on the smooth cylinder
3	$95^{th} F_V^r$ = 95th percentile of the vertical force on the rough cylinder
4	$95^{th} F_V^r$ = 95th percentile of the vertical force on the smooth cylinder
5	AI = artificial intelligence
6	A_i = horizontal attenuation factor
7	a_i = wave amplitude
8	$A_{x,z}$ = influence area
9	a_y = horizontal component of the acceleration
10	a_z = vertical component of the acceleration

Table A.1: Symbology used in the thesis (continue on the next page).

SYMBOLOGY	
11	β = threshold
12	B_i = vertical attenuation factor
13	$B_{x,z}$ = influence area
14	C_D = drag coefficient
15	CDF = cumulative distribution function
16	C_L = lift coefficient
17	C_{MH} = horizontal inertia coefficient
18	C_{MV} = vertical inertia coefficient
19	CNN = convolutional neural network
20	D = diameter of the cylinder
21	δ = reference angle of the pressure transducer
22	d = water depth
23	D_e = external diameter of the cylinder
24	Δp = dynamic pressure
25	Δx = distance between the ultrasonic probes
26	e = distance between the lower part of the cylinder and the bed
27	ϵ_i = phase angle
28	E_p = absolute error
29	ϕ = velocity potential
30	F_D = drag force on the cylinder
31	F_H = horizontal force on the cylinder
32	F_{HI} = horizontal inertia force on the cylinder
33	F_L = lift force on the cylinder
34	FNN = feedforward neural network
35	FS = full scale range
36	F_V = vertical force on the cylinder
37	F_{VI} = vertical inertia force on the cylinder
38	γ_w = specific water weight
39	η = surface elevation
40	H_s = significant wave heigth

Table A.2: Symbology used in the thesis (continue on the next page).

	SYMBOLOGY
41	k = heigth of the roughness
42	KC = Keulegan-Carpenter number
43	k_i = wave number
44	MAE = mean absolute error
45	MSE = mean squared error
46	ν = viscosity of the fluid
47	P = probability of exceedance of the peak of the forces
48	p = total pressure
49	PDF = probability density function
50	PE = percentage error
51	PLA = polylactic acid
52	ps = static pressure
53	θ_i = wave direction
54	Re = Reynolds number
55	$ReLU$ = rectified linear unit
56	RNN = recurrent neural network
57	$S(\omega, \theta)$ = directional wave spectrum
58	S_f = frequency spectrum
59	σ_{FHr} = standard deviation of the horizontal force on the rough cylinder
60	σ_{FHs} = standard deviation of the horizontal force on the smooth cylinder
61	σ_{FVr} = standard deviation of the vertical force on the rough cylinder
62	σ_{FVs} = standard deviation of the vertical force on the smooth cylinder
63	σ_p = standard uncertainity
64	σ_{vy} = root mean square of the velocity
65	SWL = surface water level
66	T = period of the wave
67	t_i = standard thickness of the roughness
68	t = time
69	$T*$ = abscissa of the absolute minimum of the autocovariance
70	Tp = peak period
71	σ_i = root mean square of the surface elevation
72	j=transformed value of the standard deviation
73	v_{ym} = maximum value of the horizontal velocity
74	v_{ym0} = significant velocity at the sea bottom

Table A.3: Symbology used in the thesis (continue on the next page).

	SYMBOLOGY
75	v_y = horizontal component of the velocity
76	v_z = vertical component of the velocity
77	ω = angular frequency
78	y = hoorizontal cordinate axis
79	$\psi*$ = narrow bandedness parameter
80	z = vertical coordinate axis with origin at the still water level
81	z_c = coordinate axis of the cylinder center with origin at the still water level
82	y = coordinate axis orthogonal to the coast and orthogonal to the cylinder

Table A.4: Symbology used in the thesis.

Bibliography

[1] Iberahin Jusoh and Julian Wolfram. "Effects of marine growth and hydrodynamic loading on offshore structures". In: *Jurnal Mekanikal* (1996).

[2] Momchilo M Zdravkovich. *Flow around circular cylinders: Volume 2: Applications*. Vol. 2. Oxford university press, 1997.

[3] T Sarpkaya. "On the effect of roughness on cylinders". In: (1990).

[4] A Theophanatos and J Wolfram. "Hydrodynamic loading on macro-roughened cylinders of various aspect ratios". In: (1989).

[5] Pedro Almeida Vinagre et al. "Marine biofouling: a European database for the marine renewable energy sector". In: *Journal of marine science and engineering* 8.7 (2020), p. 495.

[6] Alexandra Chava et al. "AT THE INTERFACE OF MARINE DISCIPLINES". In: *Oceanography* 34.3 (2021), pp. 61–70.

[7] Koh Lip Low, Hong Woo Khoo, and Lip Lin Koh. "Ecology of marine fouling organisms at Eastern Johore Strait". In: *Environmental Monitoring and Assessment* 19 (1991), pp. 319–333.

[8] Franck Schoefs, Arash Bakhtiari, and Hamed Ameryoun. "Evaluation of hydrodynamic force coefficients in presence of biofouling on marine/offshore structures, a review and new approach". In: *Journal of Marine Science and Engineering* 10.5 (2022), p. 558.

[9] Paolo Boccotti et al. "Field experiment on random wave forces acting on vertical cylinders". In: *Probabilistic engineering mechanics* 28 (2012), pp. 39–51.

[10] Paolo Boccotti et al. "Two small-scale field experiments on the effectiveness of Morison's equation". In: *Ocean Engineering* 57 (2013), pp. 141–149.

[11] JR Morison, Joseph W Johnson, and Samuel A Schaaf. "The force exerted by surface waves on piles". In: *Journal of Petroleum Technology* 2.05 (1950), pp. 149–154.

[12] Hin-Fatt Cheong, N Jothi Shankar, and K Subbiah. "Inertia dominated forces on submarine pipelines near seabed". In: *Journal of Hydraulic Research* 27.1 (1989), pp. 5–22.

[13] Paolo Boccotti. *Wave mechanics for ocean engineering*. Elsevier, 2000.

[14] Paolo Boccotti. "A method to obtain the directional wave spectrum". In: *Ocean engineering* 31.5-6 (2004), pp. 539–545.

[15] Francesco Aristodemo, Giuseppe Roberto Tomasicchio, and Paolo Veltri. "New model to determine forces at on-bottom slender pipelines". In: *Coastal Engineering* 58.3 (2011), pp. 267–280.

[16] Maduka Maduka et al. "Hydrodynamic effects of biofouling-induced surface roughness–Review and research gaps for shallow water offshore wind energy structures". In: *Ocean Engineering* 272 (2023), p. 113798.

[17] Jorgen Fredsoe and B Mutlu Sumer. *Hydrodynamics around cylindrical structures (revised edition)*. Vol. 26. World Scientific, 2006.

[18] H Honji. "Streaked flow around an oscillating circular cylinder". In: *Journal of Fluid Mechanics* 107 (1981), pp. 509–520.

[19] Turgut Sarpkaya, Michael Isaacson, and JV Wehausen. "Mechanics of wave forces on offshore structures". In: (1982).

[20] Mads B Bryndum, Vagner B Jacobsen, and LP Brand. "Hydrodynamic forces from wave and current loads on marine pipelines". In: *Offshore Technology Conference*. OTC. 1983, OTC–4454.

[21] MB Bryndum, V Jacobsen, and DT Tsahalis. "Hydrodynamic forces on pipelines: Model tests". In: (1992).

[22] Turgut Sarpkaya. *In-line and Transverse Forces on Smooth and Sand-roughened...* Naval Postgraduate School, 1976.

[23] Turgut Sarpkaya. "In-line and transverse forces on cylinders in oscillatory flow at high Reynolds numbers". In: *Journal of ship Research* 21.04 (1977), pp. 200–216.

[24] BM Sumer, BL Jensen, and J Fredsøe. "Effect of a plane boundary on oscillatory flow around a circular cylinder". In: *Journal of Fluid Mechanics* 225 (1991), pp. 271–300.

[25] PW Bearman and JR Chaplin. "The loading on a cylinder in post-critical flow beneath periodic and random waves". In: (1985).

[26] Wataru Koterayama, Masahiko Nakamura, and Changhong Hu. "Drag and Inertia coefficients of a Cylinder in Random Waves". In: (1995).

[27] E Achenbach and E Heinecke. “On vortex shedding from smooth and rough cylinders in the range of Reynolds numbers 6× 103 to 5× 106”. In: *Journal of fluid mechanics* 109 (1981), pp. 239–251.

[28] Kris A Digre and Farrel Zwerneman. “Insights into using the 22nd edition of API RP 2A recommended practice for planning, designing and constructing fixed offshore platforms-working stress design”. In: *Offshore Technology Conference*. OTC. 2012, OTC–23558.

[29] Andreas Theophanatos. “MARINE GROWTH AND THE HYDRODYNAMIC LOADING OF OFFSHORE STRUCTURES.” In: (1989).

[30] CoCo Teng and JH Nath. “Hydrodynamic forces on roughened horizontal cylinders”. In: *Offshore Technology Conference*. OTC. 1989, OTC–6008.

[31] M Zeinoddini et al. “Towards an understanding of the marine fouling effects on VIV of circular cylinders: Response of cylinders with regular pyramidal roughness”. In: *Applied Ocean Research* 59 (2016), pp. 378–394.

[32] M Zeinoddini et al. “Towards an understanding of marine fouling effects on the vortex-induced vibrations of circular cylinders: partial coverage issue”. In: *Biofouling* 33.3 (2017), pp. 268–280.

[33] P Jadidi et al. “Towards an understanding of marine fouling effects on VIV of circular cylinders: Aggregation effects”. In: *Ocean Engineering* 147 (2018), pp. 227–242.

[34] Antoine Marty et al. “Experimental study of hard marine growth effect on the hydrodynamical behaviour of a submarine cable”. In: *Applied Ocean Research* 114 (2021), p. 102810.

[35] Antoine Marty et al. "Effect of roughness of mussels on cylinder forces from a realistic shape modelling". In: *Journal of Marine Science and Engineering* 9.6 (2021), p. 598.

[36] A Marty et al. "Experimental study of two kinds of hard marine growth effects on the hydrodynamic behavior of a cylinder submitted to wave and current loading". In: *Ocean Engineering* 263 (2022), p. 112194.

[37] J Wolfram and M Naghipour. "On the estimation of Morison force coefficients and their predictive accuracy for very rough circular cylinders". In: *Applied Ocean Research* 21.6 (1999), pp. 311–328.

[38] J Wolfram and A Theophanatos. "The effects of marine fouling on the fluid loading of cylinders: some experimental results". In: *Offshore technology conference*. OTC. 1985, OTC–4954.

[39] Rolf Baarholm and Kjetil Skaugset. "Modelling and characterization of artificial marine growth". In: *International Conference on Offshore Mechanics and Arctic Engineering*. Vol. 48227. 2008, pp. 863–870.

[40] Joe Lemley, Shabab Bazrafkan, and Peter Corcoran. "Deep learning for consumer devices and services: pushing the limits for machine learning, artificial intelligence, and computer vision". In: *IEEE Consumer Electronics Magazine* 6.2 (2017), pp. 48–56.

[41] Vijay Kakani et al. "A critical review on computer vision and artificial intelligence in food industry". In: *Journal of Agriculture and Food Research* 2 (2020), p. 100033.

[42] Palash Goyal, Sumit Pandey, and Karan Jain. "Deep learning for natural language processing". In: *New York: Apress* (2018).

[43] Daniel W Otter, Julian R Medina, and Jugal K Kalita. "A survey of the usages of deep learning for natural language processing". In: *IEEE transactions on neural networks and learning systems* 32.2 (2020), pp. 604–624.

[44] Yu Xianjia et al. "Federated learning in robotic and autonomous systems". In: *Procedia Computer Science* 191 (2021), pp. 135–142.

[45] Ryad Zemouri, Noureddine Zerhouni, and Daniel Racoceanu. "Deep learning in the biomedical applications: Recent and future status". In: *Applied Sciences* 9.8 (2019), p. 1526.

[46] Polina Mamoshina et al. "Applications of deep learning in biomedicine". In: *Molecular pharmaceutics* 13.5 (2016), pp. 1445–1454.

[47] Pooja Jain and MC Deo. "Neural networks in ocean engineering". In: *Ships and offshore structures* 1.1 (2006), pp. 25–35.

[48] Marcel RA van Gent et al. "Neural network modelling of wave overtopping at coastal structures". In: *Coastal engineering* 54.8 (2007), pp. 586–593.

[49] Barbara Zanuttigh, Sara Mizar Formentin, and Riccardo Briganti. "A neural network for the prediction of wave reflection from coastal and harbor structures". In: *Coastal Engineering* 80 (2013), pp. 49–67.

[50] T-L Lee. "Neural network prediction of a storm surge". In: *Ocean Engineering* 33.3-4 (2006), pp. 483–494.

[51] Md Alhaz Uddin, Mohammed Jameel, and Hashim Abdul Razak. "Application of artificial neural network in fixed offshore structures". In: (2015).

[52] Ali Nazari, Pathmanathan Rajeev, and Jay G Sanjayan. "Offshore pipeline performance evaluation by different artificial neural networks approaches". In: *Measurement* 76 (2015), pp. 117–128.

[53] David E Rumelhart, Geoffrey E Hinton, and Ronald J Williams. "Learning representations by back-propagating errors". In: *nature* 323.6088 (1986), pp. 533–536.

[54] Mc C Deo et al. "Neural networks for wave forecasting". In: *Ocean engineering* 28.7 (2001), pp. 889–898.

[55] R Guarize et al. "Neural networks in the dynamic response analysis of slender marine structures". In: *Applied Ocean Research* 29.4 (2007), pp. 191–198.

[56] Can Elmar Balas, M Levent Koç, and Rıfat Tür. "Artificial neural networks based on principal component analysis, fuzzy systems and fuzzy neural networks for preliminary design of rubble mound breakwaters". In: *Applied Ocean Research* 32.4 (2010), pp. 425–433.

[57] Mehdi Shafieefar, Ardeshir Bahreininejad, and Mohammad Navid Moghim. "Prediction of Wave and Current Forces on Slender Structures Using Artificial Neural Networks". In: *HKIE Transactions* 18.1 (2011), pp. 30–35.

[58] Lucile M Quéau, Mehrdad Kimiaei, and Mark F Randolph. "Artificial neural network development for stress analysis of steel catenary risers: sensitivity study and approximation of static stress range". In: *Applied Ocean Research* 48 (2014), pp. 148–161.

[59] Suresh Behara, B Ravikanth, and Venu Chandra. "Predicting flow-induced vibrations of tandem square cylinders using finite element simulations and data-driven neural network model". In: *Ocean Engineering* 308 (2024), p. 118237.

[60] Juliette Signor et al. “Automatic classification of biofouling images from offshore renewable energy structures using deep learning”. In: *Ocean Engineering* 288 (2023), p. 115928.

[61] Wangyuan Zhao et al. “Research on the identification and distribution of biofouling using underwater cleaning robot based on deep learning”. In: *Ocean Engineering* 273 (2023), p. 113909.

[62] Hao-Ran Xie et al. “Estimation of sequential transient flow around cylinders using recurrent neural network coupled graph convolutional network”. In: *Ocean Engineering* 293 (2024), p. 116684.

[63] Ming Zhang et al. “LSTM RNN-based excitation force prediction for the real-time control of wave energy converters”. In: *Ocean Engineering* 306 (2024), p. 118023.

[64] JC Thomason et al. “Hydrodynamic consequences of barnacle colonization”. In: *Hydrobiologia* 375.0 (1998), pp. 191–201.

[65] Paolo Boccotti. *Wave mechanics and wave loads on marine structures*. Butterworth-Heinemann, 2014.

[66] David Edgar Cartwright and Michael S Longuet-Higgins. “The statistical distribution of the maxima of a random function”. In: *Proceedings of the royal society of london. series a. mathematical and physical sciences* 237.1209 (1956), pp. 212–232.

[67] Michael S Longuet-Higgins. “Observation of the directional spectrum of sea waves using the motions of a floating buoy”. In: *Oc. Wave Spectra* (1963).

[68] GM Foody, MB McCulloch, and WB Yates. “The effect of training set size and composition on artificial neural network classification”. In: *International Journal of Remote Sensing* 16.9 (1995), pp. 1707–1723.

[69] Xue Ying. "An overview of overfitting and its solutions". In: *Journal of physics: Conference series*. Vol. 1168. IOP Publishing. 2019, p. 022022.

[70] *Scikit-learn*. URL: https://scikit-learn.org/stable/.

[71] Sepp Hochreiter. "The vanishing gradient problem during learning recurrent neural nets and problem solutions". In: *International Journal of Uncertainty, Fuzziness and Knowledge-Based Systems* 6.02 (1998), pp. 107–116.

[72] *Keras*. URL: https://keras.io/.

[73] Francesco Aristodemo et al. "Solitary wave-induced forces on horizontal circular cylinders: Laboratory experiments and SPH simulations". In: *Coastal Engineering* 129 (2017), pp. 17–35.

[74] Willard James Pierson Jr and Patrick Holmes. "Irregular wave forces on a pile". In: *Journal of the Waterways and Harbors Division* 91.4 (1965), pp. 1–10.

[75] G Najafian and R Burrows. "Critical assessment of the least square error method used in derivation of Morison's force coefficients". In: (1994).

[76] Xiaonong Hu et al. "Simplified models for uncertainty quantification of extreme events using Monte Carlo technique". In: *Reliability Engineering & System Safety* 230 (2023), p. 108935.